FEEDING PROPERTIES OF THE HIGHLY GRAIN REFINED A20X ALLOY

BY

PHILIP BALE

A thesis submitted to the School of Engineering

Of

The University of Birmingham

For the Degree of

MASTER of RESEARCH

Department of Metallurgy and Materials

School of Engineering

The University of Birmingham

September 2011

ABSRACT

A program of research was conducted to evaluate the feeding behaviour of a new highly grain refined Al-4%Cu alloy, A20X, and reflect its castability within the software package MAGMASOFT for process development. A20X alloy and two similar Al-4%Cu alloys (grain refined and ingot A201) with varying levels of grain refinement were assessed quantitatively in terms of centreline porosity development in a simple geometric shaped casting (keelblock). A MAGMASOFT solidification model was calibrated experimentally to verify boundary conditions and a material database developed to accurately reflect the A20X alloys solidification behaviour based on measurement of thermophysical properties. The model was calibrated using volume fraction porosity measurements and the porosity module function (feeding effectiveness). It was found that A20X alloy exhibited significantly reduced porosity along the casting centreline (0.48%) when compared with both the grain refined A201 alloy (0.97%) and ingot A201 alloy (1.48%). This effect was due primarily to the higher levels of Ti and B present producing a fully globular microstructure. The A20X model was calibrated at a feeding effectiveness value of 93% and predicts better global porosity levels than the MAGMASOFT Al-4%Cu model, but was unable to resolve local distribution patterns because MAGMASOFT is unable to account for the heterogeneous nucleation of porosity.

DEDICATION

To my family, whose unwavering encouragement and support has pushed me over the finishing line in what has been a fantastic yet challenging two years.

ACKNOWLEDGEMENTS

I have had a great deal of help and support throughout this project from many people and I would like to take the opportunity now to offer my thanks to:

- First and foremost Professor Nick Green, for his guidance and incredible support throughout the entirety of this project without which it would not have been possible.
- Adrian Caden and Peter Cranmer, whose technical expertise and help in the foundry have been invaluable to the collection of casting data for this project. Their advice and sense of humour has made many tough days a lot easier.
- Frank Biddlestone, for his unrivalled knowledge, his help and willingness to persist with a series of complicated DSC experiments.
- Aeromet International plc specifically Bill Stott whose knowledge, interest and encouragement was inspiring.

I would also like to acknowledge the support of the Midlands Aerospace Alliance, Aerospace Technology Exploitation Program grant (ATEP112-D6) on the A20X innovative aluminium alloy.

TABLE OF CONTENTS

CHAPTER 5 RESULTS 57

TABLE OF FIGURES

LIST OF TABLES

CHAPTER 1 INTRODUCTION

The aerospace industry has, for a long time, been interested in the development and use of lightweight high strength aluminium alloys, one example of which is the Al-4Cu alloy A201 (Din and Campbell 1996). Casting this alloy potentially has huge cost benefits over the alternative machining of components from solid. However, the casting properties of A201 are poor. A newly developed alloy, A20X, exhibits superior castability and additional strengthening achieved through massive grain refinement of the primary aluminium phase by TiB_2 (titanium diboride), resulting in globular grain structures. It is the intention of this project to characterise and quantify this difference with respect to the base A201 alloy such that casting process design software (MAGMASOFT) can be calibrated and applied to assess the castability of specific structural aerospace components. By designing a castable shape that, when the critical fraction of solid (f_s(crit)) changes, the porosity distribution changes, one can analyse the effectiveness and effect feeding has on porosity between the two alloys. Castings in both alloys and measurement of thermophysical properties will enable calibration of the MAGMASOFT model to produce consistently accurate future modelling of component integrity and processes for their manufacture.

CHAPTER 2 LITERATURE REVIEW

2.1 Background to Al-Cu based casting alloys

The development of A201 was originally for improving corrosion resistance in aluminium 4.5% copper alloys in 1967. The mechanical properties of the alloy A201 are the highest among all cast aluminium making it the subject of much investigation. Interestingly, when compared compositionally with another Al-4%Cu alloy, A206, A201 has an addition of silver (between 0.4 and 1.0 wt %) which can be attributed to the improved corrosion resistance. A206 has composition: (Si 0.1 wt%, Fe 0.15wt%, Cu 4.0-4.5wt%, Mn 0.2wt%, Mg 0.15-0.55wt% and Ti 0.15-0.35wt %). (Kuo et al 1989) investigated the influence of this silver addition on the mechanical properties of A201. They cast test bars with varying quantities of Ag testing tensile strength and elongation. They reported an increase in tensile and yield strength with increasing Ag content but a decrease in percentage elongation. This contrasts with the findings of (Chien et al. 1973) and (Mollard 1970) who found both an increase in both tensile strength and percentage elongation.

(Din and Campbell 1996) compared the mechanical properties of four high strength casting alloys with ageing at high temperatures; A356, A357, A201 and A206 to produce reliable property data from sound castings for these alloys. The alloys were sand cast to produce test bars which were then measured for their properties. The copper based alloys; A201 and A206 presented with better mechanical properties overall compared with the A356 and A357 alloys as they exhibited better ultimate tensile strength, elongation to failure and proof stress over ageing of 10 hours at 200°C. The major problem for the A201 alloy is its poor castability, with many casting factors affecting the microstructures formed thus producing a range of unreliable components with undesirable properties (Berry 1999).

Clearly A201 was the starting point for further development of a lightweight aluminium alloy that exhibits high strength and can be cast successfully and reliably. A20X was subsequently developed to improve castability and provide this increase in strength across the board. A20X is a dilute Metal Matrix Composite (MMC) alloy which, in essence is A201 with the addition of titanium diboride (TiB_2) particles. (Taghiabadi et al. 2003) investigated the tensile properties of TiB_2 additions in A356 alloys. The MMC's exhibit higher ultimate tensile strength over that of the un-reinforced aluminium alloys, an increase of 30% on average.

2.2 A201 Microstructure

(Mollard 1969) studied the microstructure of cast A201 (KO-1) components demonstrating how metallography can be used as a quality control measure for castings. In doing so he describes the sand cast A201 alloy as consisting of principally aluminium rich dendrites with a partially connected framework of eutectic phase particles, with Al-Cu-Mn phases present near to the grain/dendrite edges. (Backerud et al 1990) describe the solidification process of A201 as follows: In the early stages of solidification after nucleation, aluminium rich dendrites start forming becoming increasingly enriched with alloying element. At fraction of solid around 30%, the coherency point is reached, leaving the remaining metal to solidify through interdendritic feeding over a long freezing range (120°C). The implications of this long freezing range are discussed in depth later. In the latter stages of solidification each dendrite has formed a grain which then rejects solute into the remaining liquid phase until the eutectic composition is reached. This eutectic liquid is last to solidify and becomes trapped either between grains or dendrite arms forming this semi connected framework of eutectic phases (figure 1). Table 1 shows the chemical reactions and summary of reactions during solidification of an A201.2 alloy.

Table 1: Reactions and summary of the solidification of alloy 201.2 (Backerud et al 1990).

Reaction No.	**Reactions**	**Suggested Temperature, °C**
1	Development of a dendritic network	651 - 649
2	Liq. – Al + $Al_6(MnFeCu)$	649
3	Liq. + $Al_6(MnFeCu)$ – Al + $Al_{20}Mn_3Cu_2$	616
4	Liq. – Al + Al_2Cu + $Al_{20}Mn_3Cu_2$ + Al_7FeCu_2	537
5	Liq. – Al + Al_2Cu + Al_2MgCu + Mg_2Si	500

Cooling rate (°C/s)	**Reaction No**	**T (°C)**	**T (s)**	**Fs (%)**	**Acc. Fs (%)**
0.3	1	651 – 649	40	12	12
	2	649 – 643	60	13	25
	(2-3)	643 – 631	101	27	52
	3	631 – 618	125	23	75
	(3-4)	618 – 524	353	18	93
	4	524 – 523	22	5	98
	(4-end)	523 - 521	10	2	100

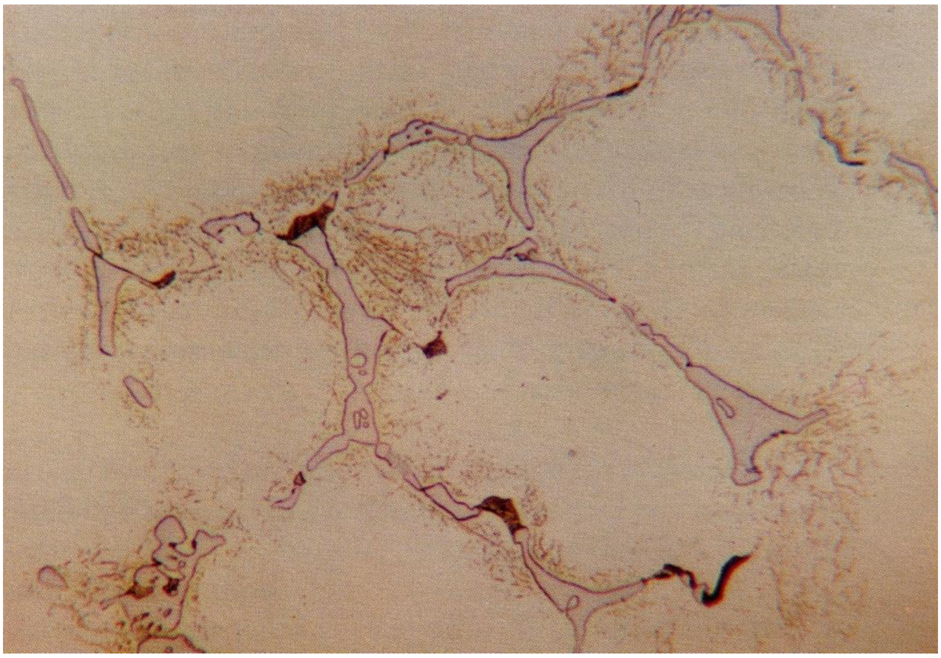

Figure 1: Micrograph showing the primary eutectic Al_2Cu and complex $Al_{20}Mn_3Cu_3$ eutectic phases at the boundary edges of grains at X560 magnification. (Backerud et al 1990)

The uniformity of phase distribution and microstructure of castings has a substantial influence on the resulting properties.

2.3 Grain Refinement

It is well understood that under normal casting conditions with slow cooling metallic alloys solidify with a coarse columnar grain structure. It is possible to develop a much finer 'equiaxed' grain structure and this is predominately done by increasing the number of active nucleation sites during solidification. This process of transforming the grain structure from coarse columnar to fine equiaxed grains is known as grain refinement (Mccartney 1988) and is utilised in almost all aluminium alloys. The benefit of grain refinement originates from the fact that mechanical properties are much improved when a fine equiaxed structure is present and it was Sicha and Boehm (1948) who first reported this with improved tensile strength and elongation in Al-4.5%Cu test bars when titanium was added. A review of grain refinement in shape aluminium castings, (Spittle 2006), has shown that a much finer grain structure (anything below 220µm (Jones and Pearson 1976)) like that seen after grain refinement also improves fatigue strength along with fluidity. Feeding is an important casting property and is also improved with grain refining as shrinkage porosity is reduced. It also leads to better distribution of microporosity on a much finer scale throughout a casting (Apelian et al 1984). Secondary phases are refined also resulting in improved machinability, conclusions echoed by a similar review into the heterogeneous nucleation of aluminium alloys (Murty et al. 2002). The A20X alloy has typically 2-4 volume % TiB_2 and makes for a very different microstructure to that of a cast A201 alloy with less or no TiB_2 addition.

2.3.1 Liquid to Solid Transition during Solidification

When an alloy freezes, to become solid from the liquid two processes occur: nucleation and growth. Nucleation is the process of forming clusters of atoms that represent the start of a new phase. Growth is then the enlargement of that initial cluster resulting in the formation of a new solid grain phase. When considering nucleation at the beginning of solidification, there are two types: homogeneous and heterogeneous. These are described below.

2.3.2 Homogeneous Nucleation

When the initial cluster of atoms that grow into a solid phase forms in the melt without the aid of foreign materials (for example: dirt, entrained oxides and inclusions, contact with the mould wall, grain refiners) it is considered to have nucleated homogeneously (Flemings 1974a).

Assuming solid forms in the liquid in a spherical shape which has a radius (*r*), volume (*V*) and surface area (*A*) with a change, *G*, in the total energy of the system: a reduction in volume free energy due to transformation of liquid to solid, given by -*V*□ which has a radius (*r*), volume (*V*) and surface area (*A*) with a change, *G*, in the total energy of the system G_V, where G_V is the volume free energy difference between liquid and solid and an increase due to the new liquid-solid interfacial energy, given by *A*□, where □ is the interfacial energy per unit area. For small values of *r* the total energy change on formation of solid is often insufficient to overcome the 'energy barrier' created by the dominant effect of surface energy. This is the case when $r < r^*$ and means that the free energy of the material is increased further by additional growth of solid and the small particles are therefore likely to re-melt . Particles whose radius exceeds r^* are stable, as their further growth (increase in r^*) leads to a decrease in *G* such that their growth continues. This is described schematically in Figure 2 where the maximum value on the ΔG_r curve denotes the 'turning point' or critical radius of a particle, r^* (Flemings 1974a)

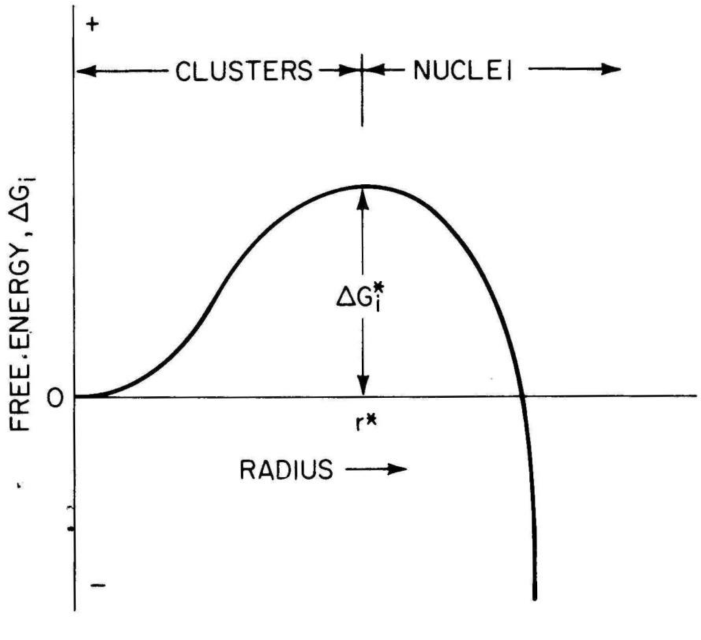

Figure 2: The free energy change associated with homogeneous nucleation of a sphere of radius (r) (Flemings 1974b).

The critical particle size (r*) is obtained by differentiation of the expression for the total energy change:

– (2.1)

and putting the first derivative as zero to find the turning point yields

— (2.2)

where $\square_{SL}$ is a solid-liquid interfacial energy and hence ΔG^* is:

—— (2.3)

Generally ΔG_V varies in proportion to the degree of undercooling, ΔT, and in simplest form can be expressed as $=L\ (\Delta T/T_m)$ where L is the latent heat of fusion and T_m the absolute melting temperature (K). Therefore, as the undercooling is increased the critical nucleus radius is decreased (Porter and Easterling 2008).

2.3.3 Heterogeneous Nucleation

The classic theory of heterogeneous nucleation (Turnbull 1950) describes nucleation as the process of forming a solid particle on foreign impurities. These foreign substrates act as catalytic surfaces that reduce the size of the 'energy barrier' $\square G$ that produces stable nuclei for growth to then occur. These solid nuclei form as a spherical cap shape at the catalyst-liquid surface (figure 3) and the energy barrier ΔG^* is expressed as:

——— (2.4)

Where $f(\theta) = \frac{1}{4}(2 - 3\cos\theta + \cos3\theta)$ which is the catalytic efficiency of the substrate, θ is the contact angle of the catalyst-solid-liquid triple point and $\cos\theta$ represents the resultant energies of the catalyst-liquid and catalyst-solid interfacial energies (Flemings 1974a).

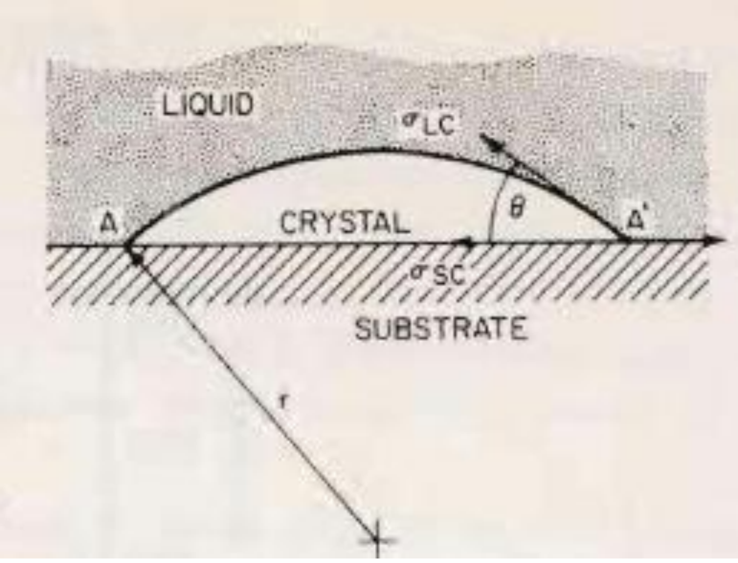

Figure 3: Formation of a solid particle on a substrate where θ is the contact angle and r is the radius of the particle (Flemings 1974a)

At low values of θ where the substrate is wetted by the solid the energy barrier to nucleation is dramatically reduced compared to homogeneous nucleation (Flemings 1974a) and alloys require only a very small undercooling maybe two or three degrees for nucleation to occur. By resembling at a crystallographic level the phase to be nucleated the solid 'wets' the substrate with a low contact angle θ. Under such conditions the spherical cap of solid has satisfied the critical particle size (r^*) but done so by reducing the volume and interfacial area of the newly nucleated site within the liquid and thus reduced the free energy required ΔG^* (figure 4).

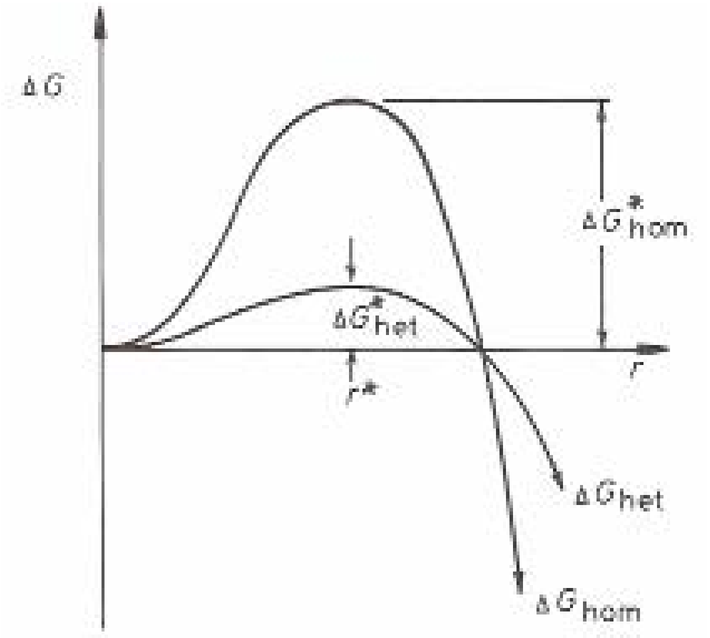

Figure 4: the free energy difference of solid clusters for homogeneous and heterogeneous nucleation at the critical particle size r*(Porter and Easterling 1981)

2.4 Grain Refinement of Aluminium

Although there has been extensive research reported that focuses on grain refinement in aluminium alloys there is still ambiguity as to its precise mechanism. From the literature there are six groups that the theories can be summarised in.

- Carbide/Boride theory
- Phase diagram/peritectic theory
- Peritectic hulk theory
- Hypernucleation theory
- Duplex nucleation theory
- Solute theory

The details of these theories can be seen in reviews by: (Glasson and Emley 1968): (McCartney 1989); (Easton and StJohn 1999) and (Spittle 2006). This review though will aim to concentrate more on the effects of grain refinement on casting aluminium alloys.

2.4.1 Methods of Grain Refining

There are various methods that can achieve refined grain structures in aluminium alloys. The most widely used method is the addition of inoculants into the melt before casting, typically as bars, waffles or salts but usually a master alloy (typically Al-5Ti-1B) in which the boron is locked in the compound, TiB_2 and the titanium is in solid solution as $TiAl_3$. These take advantage of the well known concept of heterogeneous nucleation during solidification (section 2.3.3). This method of refining has become an industrial norm for foundries and can be added at any stage in the casting process. (Jones and Pearson 1976) however, studied the effect of dwell time in the melt on the effectiveness of the refiner (Al-5Ti-1B master alloy) in a high purity aluminium system and found that there was a required time to achieve the smallest grains and then a drop off point at which grain size started to increase again (figure 5).

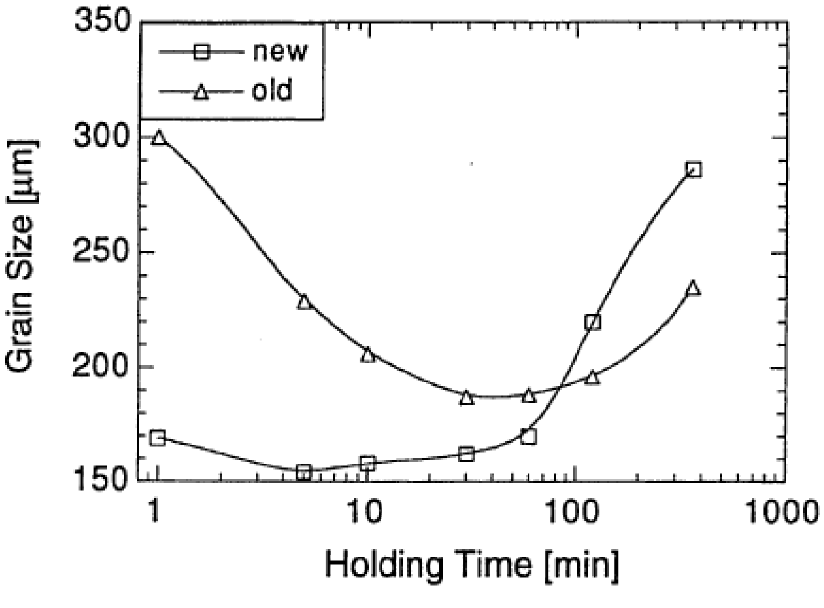

Figure 5: Effect of holding time on the effectiveness of Al-5Ti-1B grain refiner in a high purity aluminium system (Jones and Pearson 1976).

How long it takes for the refiner to dissolve evenly throughout the melt will affect the contact time (Schumacher et al. 1998). The role of the TiB_2 compound and the fundamental constituents titanium and boron as nucleants, is dependent on the alloy composition and the weight ratio. Figure 6 shows that with an increasing Ti/B weight percentage in the melt, the average grain size decreases with increasing boron content.

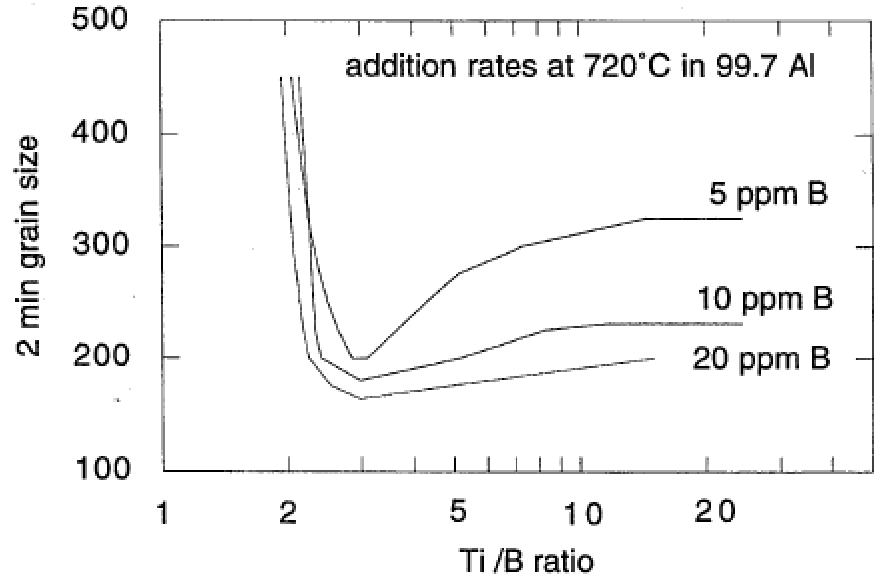

Figure 6: Average grain size of commercial purity aluminium in Alcan test after two minute holding time, as a function of Ti/B weight ratio in the melt, for various Boron additions. Refining performance improves sharply as the stoichiometric ratio of 2:2.215 is exceeded but decreases at higher titanium contents (Schumacher et al 1998; based on original data from (Pearson and Birch 1979)).

Another method of refining the grain structure of cast alloys is ‘melt shearing’. Zuo and co-workers (2011) melt sheared a commercial AA7032 alloy using two intermeshed rotating screws in the melt before casting into thin-walled steel moulds to evaluate the use of fragmented oxide films as potent grain refiners. Metallographic analysis of samples anodized using HBF_4 (figure 7) shows the effects of this method of grain refining on the microstructures formed.

Other similar methods reviewed by (Murty et al 2002) include the disruption of the alloy melt during solidification through mechanical agitation and vibrations (Cahoon et al 1992) (Fang and Bruno 1991) as well as mould coating with metal particles (Reynolds and Tottle 1951) all of which have been proven to produce a refined grain structure.

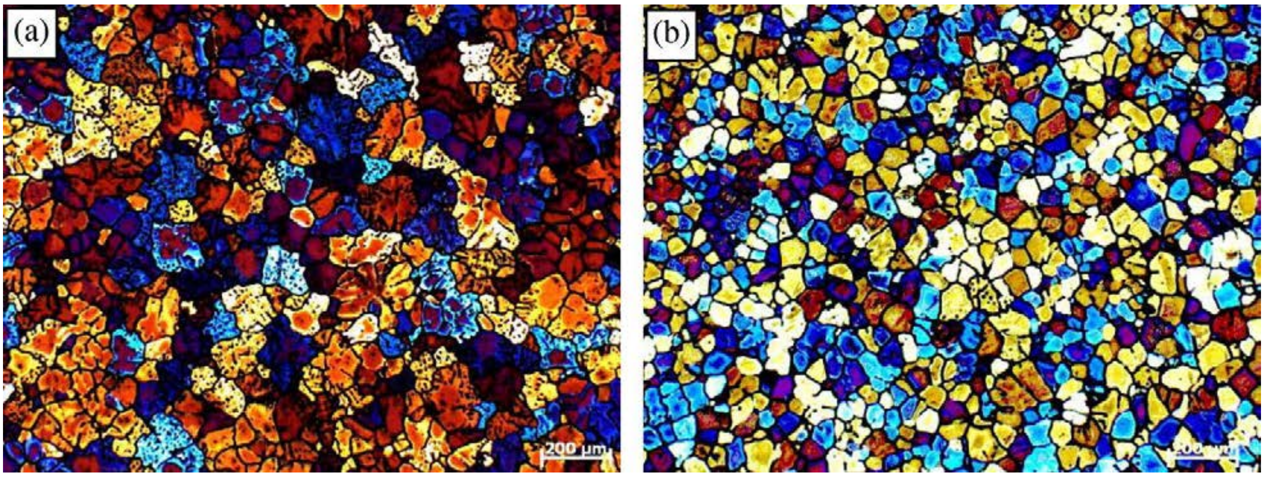

Figure 7: Microstructure of AA7032 alloy cast in a thin walled steel mould at 660°C: (a) without shearing; (b) with shearing; (Zuo et al. 2011)

2.6 Effect of Grain Refinement on Grain Morphology

Aluminium alloys like A201 without the addition of grain refining, solidify with a dendritic grain structure. Figure 8 shows schematically these dendrites as tree like structures with a primary trunk and various 2° and 3° branches. The morphology of a growing interface depends a lot on localised thermodynamic properties, solute concentration and diffusion as well as growth rates of the solid/liquid interface. During solidification, nuclei that grow to form grains are typically stable as spheres but the solid-liquid interface is often subject to random spacial disturbances, caused possibly by local temperature fluctuations, insoluble particles and often chance natural vibrations that cause interfacial instability leading to dendritic growth. In this case the development of perturbations on the spherical interface surface causes the sphere to become distorted creating a wave-like interface with peaks and troughs. The nuclei then grow into an undercooled melt and the latent heat from growth reinforces the negative temperature gradient in the liquid and flows down the perturbation peaks of the solid interface reinforcing the temperature gradient and rejecting more heat at those growing tips making the morphology unstable and growth rate fast which causes the dendritic structures forming as solid (Kurz - Fisher 1989).

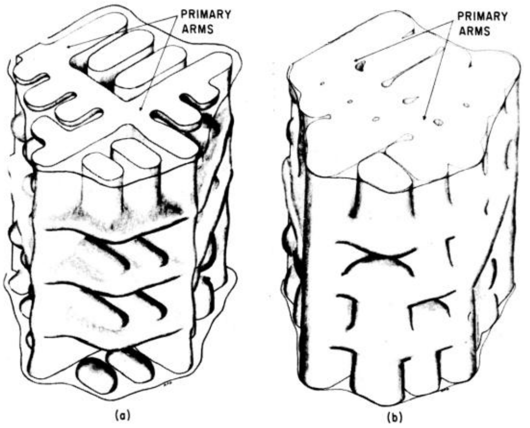

Figure 8: Dendrite structure of Al-4.5%Cu alloy at a) 50% solidified and b) 90% solidified. (Flemings 1974)

(Mullins and Sekerka (1963) confirm that the growth of a spherical particle during phase transformation is stable below and unstable above a certain radius R_c. By introducing an infinitesimal deviation into the growing particle interface and then calculating the time dependence of the coefficient of expansion Mullins and Sekerka were able to define the critical radius as:

(2.5)

Where the radius R_c is seven times the critical radius for nucleation and growth of a solid particle.

As reported by Kurz and Fisher (1989) there is a sizeable change in the concentration ahead of the solid-liquid interface due to solute build up ahead of the front which will change the local equilibrium solidification temperature of the liquid. This build up of solid must be expelled down the interfacial concentration gradient that is caused by this concentration variance at the interface by a heat flux diffusion phenomena. It can be said that this rate of rejection is proportional to the growth rate of the solid and so the gradient becomes steeper. A zone or state of constitutional undercooling is then reached when the temperature of the melt ahead of the interface is lower than the local solidification temperature at the solid interface. A perturbation on the surface causes the gradient of the local solute concentration to rise and with it, the rise in liquidus temperature and the preservation of the undercooling effects.

The zone of constitutional undercooling can be defined in terms of the critical growth velocity of the interface:

$$— \qquad (2.6)$$

Where V_c is the critical growth velocity rate for constitutional undercooling, G is the temperature gradient of the interface, D is the diffusion coefficient of the liquid and ΔT_o is the liquidus solidus range at a composition $C_{o.}$

Adding a grain refiner to an alloy increases the number of growth centres for solid grain initiation (TiB_2). They increase the nuclei by many orders of magnitude and as a result the growth rate of each interface is slowed and so the interface growth rate is smaller than the critical growth rate for the undercooling ($V< V_c$), and so the growing solid-liquid remains stable resulting in the preferred original spherical globular shape forming.

2.7 Castability of Metal Alloys

(Di Sabatino and Arnberg 2009) stated that the castability of an alloy is its ability to be cast to a given shape with a given process without the formation of casting defects. Alloy dependant phenomena that determine the castability of an alloy are: feeding and shrinkage, hot-tearing, segregation and fluidity, (Campbell 2003), (Mollard et al. 1987). The effects of microstructure (grain size and morphology) are important to understand when trying to reduce the negative impact these phenomena have on castings. Regarding alloy composition, it is accepted that some alloying elements affect castability. Specifically with regards to aluminium, the addition for example of copper (2000 series) typically 1-5wt% results in a long freezing range and increased susceptibility to hot-tearing (Di Sabitino et al 2009). These four phenomena are explored in further detail with regards cast aluminium alloys.

2.7.1 Segregation

Segregation refers to any variation in chemical composition throughout a casting. During solidification there are three zones or states: solid, liquid, and the solid-liquid mixture known as the mushy zone. The fundamental cause of segregation is the partitioning of solute (in the case of aluminium A201 this is predominantly copper) ahead of the advancing front of solid forming during solidification. The solute (Cu) is rejected from the solid and is pushed back into the surrounding interdendritic liquid feeding through the mushy zone. This happens because the solubility of the solute in the solid is less than that in the liquid. The extent of partitioning is expressed as a coefficient:

$$- \qquad (2.7)$$

Where k is the equilibrium partition coefficient (the ratio of the solubility of the solute in the solid C_s compared to the content of the liquid C_L in equilibrium at temperature T).

In alloys where $k < 1$), the higher tendency there is for segregation of solute into the remaining liquid during solidification (Ghosh 1990).

Figure 9 illustrates the build up of solute ahead of the solidifying front and the corresponding compositional changes that occur. When a liquid is flowing through the solid dendrites of the mushy zone ‘equilibrium portioning’ of the solutes can occur.

To quantitatively describe and account for segregation, the Gulliver-Scheil equation was established. A consequence of independent work (Gulliver 1913) and (Scheil 1942), their work was credited with linking the concentration of the solid (C_S^*) as a function of the solid fraction (f_s) when equilibrium is not attained in liquid and solid during solidification. This is the case in almost all castings due to limited diffusion back into the solid as the temperature falls. Under such circumstances the concentration of the solid C_S* was shown to be

(2.8)

Where kC_0 is the initial solid composition. This equation has been used to predict certain phenomena: that for example alloys of a constant k, some eutectic will always form no matter how low the solute content and has been demonstrated experimentally in aluminium-copper alloys; interdendritic eutectic $CuAl_2$ has been found in alloys of composition of 0.5%Cu, when the limit of solubility is in excess of 5% and the eutectic composition is 33% (Brody and Flemings 1966).

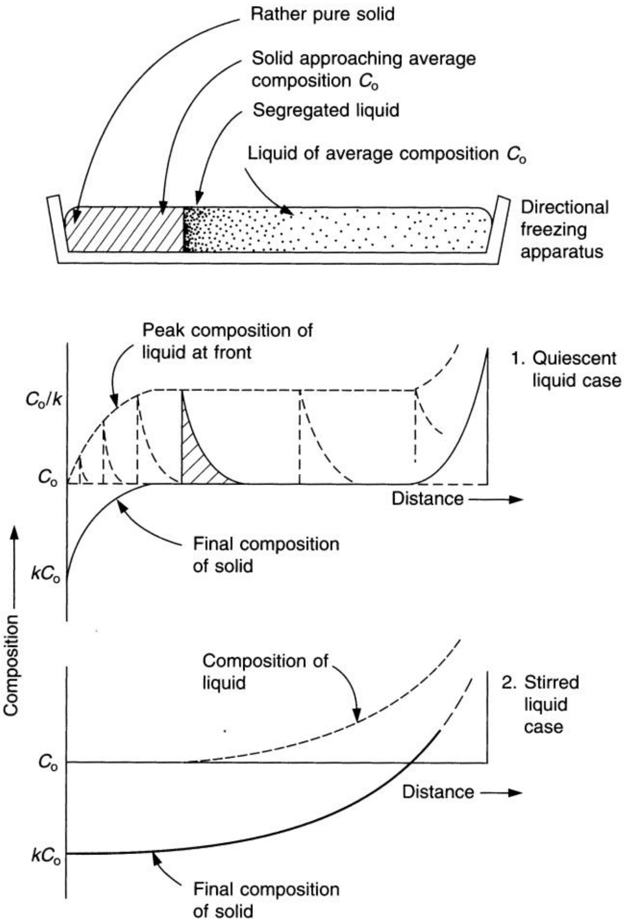

Figure 9: Directional solidification on a planar front giving rise to two different patterns of segregation depending on whether there is a build up of solid or whether it's stirred away by mixing (Campbell 2003)

The implication segregation has on Al-Cu based alloys is that because of their very long freezing range and particularly in the last 10-20% of residual liquid over a wide temperature range (120°C), the eutectic phases form a semi connected network throughout the structure which impacts on properties. Figure 10 shows the fraction of solid curves for three aluminium-copper alloys A201, A206 and an Al-4%Cu alloy. It is clear that the first 70% of the solid formed is done so over a short temperature range (mass feeding). Once the coherency point is reached the remaining 30% of solid feeds through the mushy zone through the interdendritic regions and solidifies. This behaviour promotes segregation of the alloys.

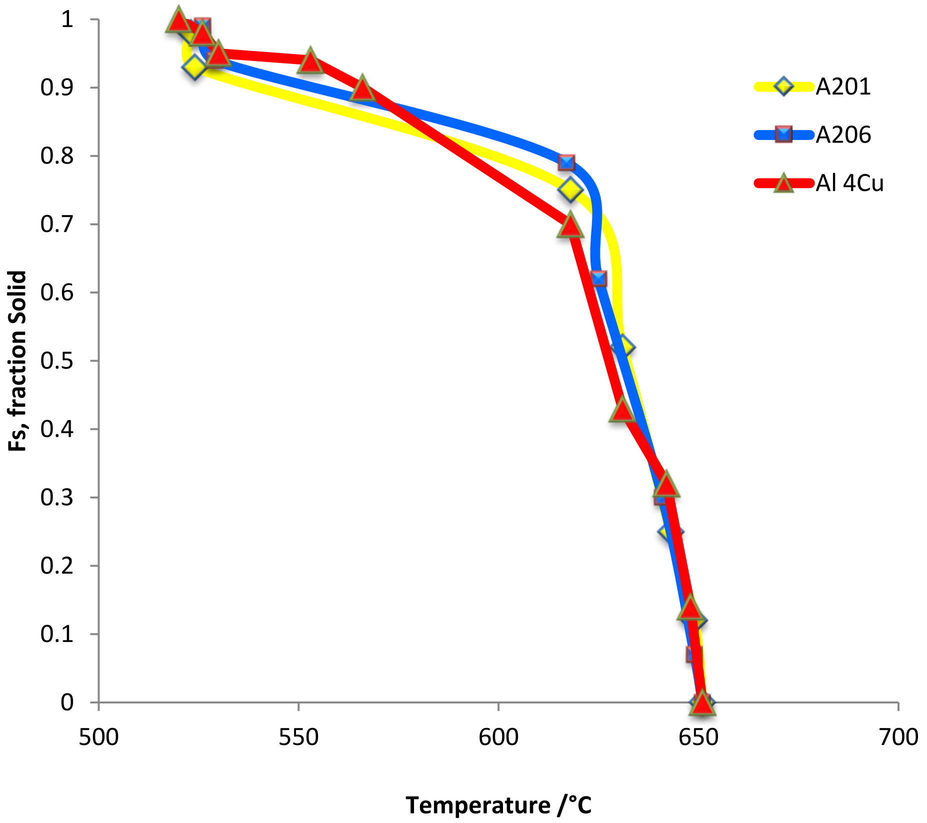

Figure 10: Fraction Solid curves for three aluminium alloys: A201, A206 and Al-4%Cu. (MAGMAsoft4.0 material database, and Backerud et al 1990)

2.8 Porosity

In general terms porosity describes any void or hole in a casting. It is one of the major defects that can be found in a casting. The main sources of porosity are:

- Shrinkage as a result of poor feeding during solidification.
- Hydrogen gas dissolved from melting
- Inclusions
- Entrapped air from filling (turbulent flow or blowholes)

Of these, hydrogen gas and shrinkage are the most prominent sources of porosity and form as a direct result of solidification behaviour. Whereas inclusions (both metallic and non-metallic) and entrapped air are a result of prior melt handling and fluid flow in the mould during filling. Regardless of the origin the negative impact porosity has on mechanical properties is significant. The presence of voids and pores create stress concentration sites an which result in premature failure and particularly reduced ultimate tensile strength and fatigue strength (Campbell 1991).

2.8.1 Shrinkage Porosity

Aluminium castings can exhibit a volumetric contraction in the range of 5-6% during solidification, due to the difference in density between the liquid and solid phases (Anson et al 1999). As areas of a casting solidify, this shrinkage is compensated for by a flow of liquid through the semi-solid regions in surrounding areas feeding it. As solidification progresses the interdendritic channels that feed the shrinkage become smaller and eventually freeze, blocking off the supply of liquid. If shrinkage is present in these isolated regions it puts tension on the liquid and voids form as a result to try and relieve the stresses, creating pores. If shrinkage continues these pores can grow and spread creating widespread shrinkage porosity. Shrinkage can be reduced significantly when the feeding to a casting is improved but unless there is sufficient pressure through the mushy zone to enable the flow of liquid, porosity will result.

2.8.2 Hydrogen Porosity

A result of the decrease in solubility of hydrogen between the liquid and solid phases of solidifying aluminium, cast aluminium alloys can be affected by hydrogen porosity. Hydrogen is less soluble in solid aluminium as compared with liquid aluminium (i.e. k«1) (Figure 11a). As solid dendrites grow, hydrogen is rejected into the interdendritic liquid. When the levels of hydrogen in the last remaining liquid reach a critical level, the gas precipitates from solution, forming discrete bubbles (pores) (Figure 11b).

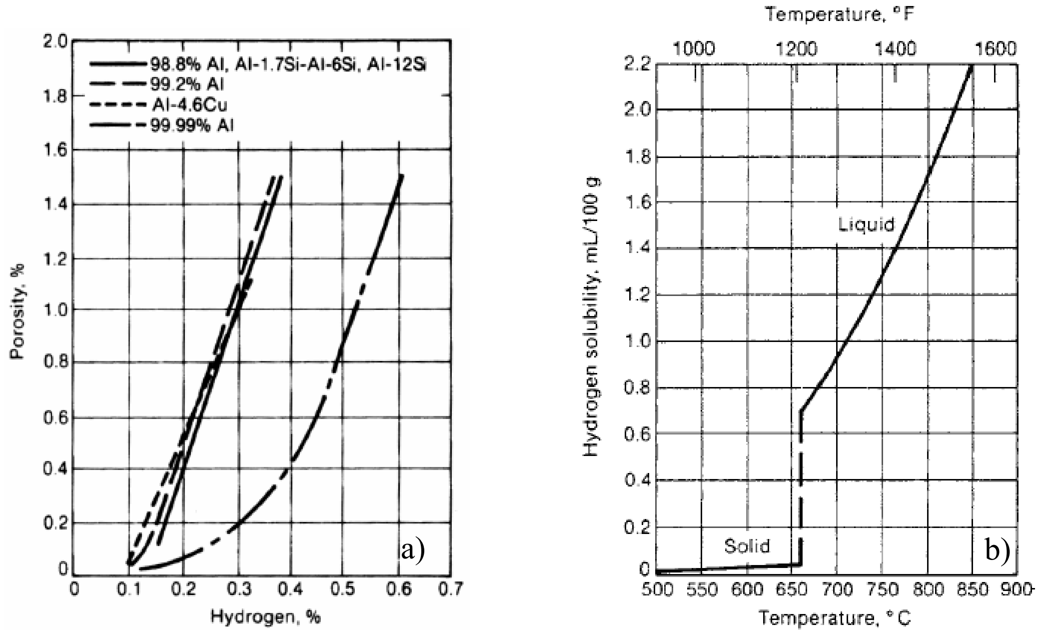

Figure 11: a) Solubility of Hydrogen in aluminium in 1atm hydrogen pressure (Fang and Granger 1989) b) porosity as a function of hydrogen content in four cast Aluminium alloys (Monroe 2005).

Recent experience of casting the A20X alloy has highlighted its superior feeding characteristics and integrity when compared with the conventional A201 alloy and the challenge is how to predict integrity and design feeding systems that can be used for this new alloy.

2.9 Mechanisms of feeding to avoid shrinkage porosity

The effectiveness and adequacy of feeding during solidification has a critical effect on the formation of possible defects in a casting. As a casting solidifies, the resultant solid formed, usually comprises a mass of dendritic grain envelopes, the dendrites comprising a tortuous intertwined network. As the fraction of solid increases it then becomes increasingly difficult for the remaining liquid to flow through the mush and reach isolated areas (feed). The resistance to flow is defined by the liquid permeability and the magnitude of resistance given by the Darcy equation (Darcy 1856). Thus, the volumetric contraction of the solid on freezing can cause substantial pressure drops within the mushy zone resulting in large local hydrostatic tension which in turn lead to the initiation and growth of pores and so shrinkage. (Campbell 1969) first identified five mechanisms (figure 12) by which the production of a pressure differential in the casting can be reduced, *i.e.* feeding. By a process of feeding the solidifying casting through these five mechanisms, the production of pressure related defects can be reduced substantially. They are:

- Liquid Feeding
- Mass Feeding
- Interdendritic Feeding
- Burst Feeding

- Solid Feeding

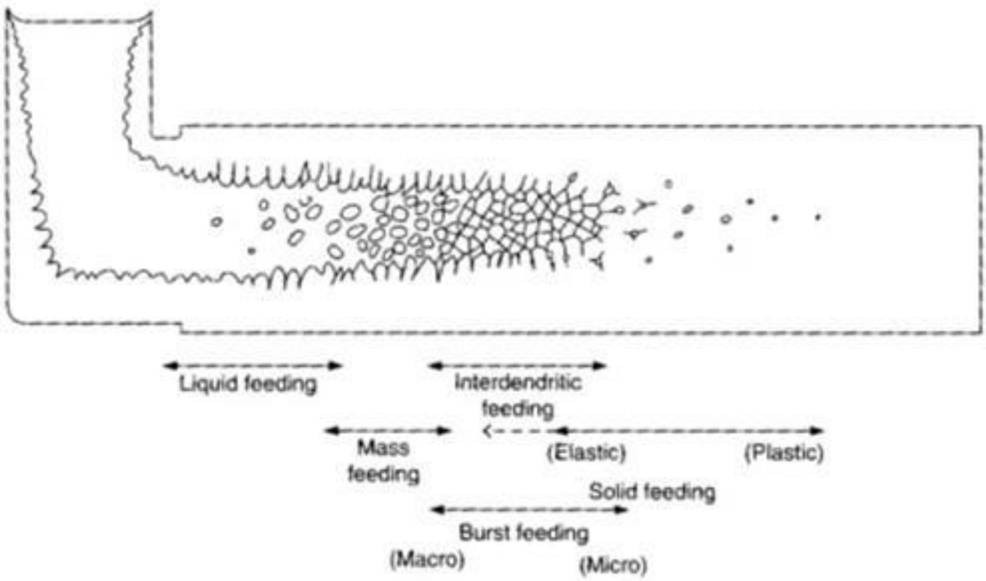

Figure 12: Schematic representation of the five feeding mechanisms described by (Campbell 1969)

2.9.1 Liquid Feeding

Liquid feeding is the first mechanism to operate in a casting and because it is early on during solidification the feed path is usually wide, unblocked and the pressure drop required to overcome resistance to flow small, so formation of shrinkage related defects are rare at this stage. The viscosity of the feed metal is also at its lowest point throughout solidification and so flows freely. In reality for long range freezing alloys, like A201, the development of initial solid (dendrite network) is early on during solidification so liquid feeding stops at a relatively early stage and thus is a less important feeding mechanism during solidification.

2.9.2 Mass Feeding

Mass feeding is the next mechanism to take effect after liquid feeding and it is a key mechanism of interest in A20X. It denotes the movement of the slurry of solidified metal and residual liquid (Baker 1945). Mass feeding can occur from anywhere between 0-50% and up to 68% solid (Campbell 1969) and the coherency point and rigidity points mark the impingement of dendrites and the transition to interdendritic feeding and then the dominance of Darcy flow depending on the pressure difference driving flow in the casting before the dendrites form a solid network. Figure 13 shows the difference in these points when the freezing range is varied. (Backerud et al 1996) performed numerous torque tests on alloys during solidification to measure the strength of the mushy zone.

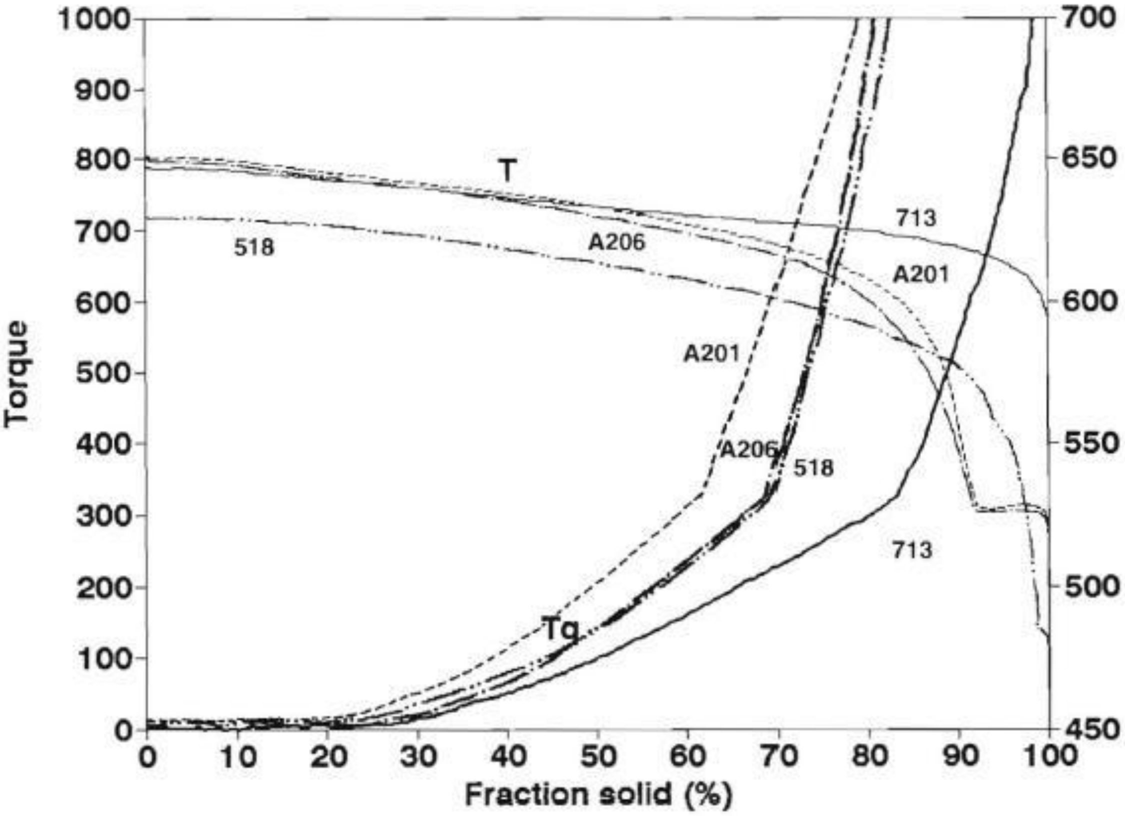

Figure 13: A grouping of temperature (T) and torque (Tq) curves for a series of aluminium casting alloys: Alloy 713, Alloy 518, Alloy A201 and Alloy A206 (Backerud et al 1996).

The 713 alloy has a short freezing range (58°C) and both coherency and rigidity points are reached at much higher solid fractions (24 and 79% fs) compared with the A201 alloy which has a long freezing range (133°C) and consequently lower solid fraction values for the two points (21 and 62% fs). Important then, is the assessment of mass flow. Knowing the ratio between casting section thickness and average grain size one can make this assessment. The larger the grain size and smaller the cross-section of casting, the more flow of metal will be impeded and greater porosity seen. This highlights the importance of grain refinement with the flow of this mass slurry being possible for longer during solidification.

2.9.3 Interdendritic Feeding

Thirdly is interdendritic feeding which is the flow of residual liquid through the mushy zone. During solidification, the developing dendrites eventually impinge and connect together creating a solid frame. This happens at what is known as the dendrite coherency point. When this happens the strength of the network is sufficient to prevent mass feeding from continuing and fluid flow through the network channels starts. This flow is likened to the flow through a capillary.

2.9.4 Burst feeding

The existence of the next feeding mechanism, burst feeding, is reasoned but speculative. When a poorly fed region of a casting becomes isolated, owing to the increasing hydrostatic pressure build-up it has been argued that the strength of the semi solid shell may be insufficient to sustain the stress arising from the internal pressure drop and ruptures (bursts) leading to liquid metal feeding the isolated region a bit like a dam bursting (Campbell 1969). As the pressure increases, both the strength and stress of the dendritic barrier increase so depending on the nature of the blockage, the yielding maybe sudden or not at all.

2.9.5 Solid Feeding

Like in burst feeding it is possible for areas in the casting to become isolated during freezing. Near the end or solidification, regions that have solidified before others can block the path of feed liquid and isolate them. The resulting negative internal hydrostatic pressure can act on the external skin to deform the solidified region, via rapid creep or plastic collapse, sucking it inward by creep flow and thus relieving some of the locally reduced pressure. (Campbell 2003) described the stress model of solid feeding as the liquid being limited by the plastic yielding of the solid. This then makes it a function of the yield stress and the shape of the solid which in turn is a function of the strain rate at the given temperature. (Harinath et al 1979) looked at the effect of internal porosity and external sink formation with increasing casting temperature of an Al-12%Si alloy. A figure 14 show that as casting temperature was increased the external surface sinks (evidence of solid feeding) increased with a concomitant decrease in internal porosity. This elegant experiment is a good example of solid feeding because at lower casting temperatures the solid formed gains strength rapidly during solidification and therefore retains its shape leading to other feeding mechanisms dominating, whereas at higher temperatures the falling yield stress of the solidified metal allows for more collapse and so a reduction in internal porosity.

Al-Cu alloys have a long freezing range and as a result the mushy zone is effectively increased so the effectiveness of the feeding is crucial to reducing porosity formation in these alloys.

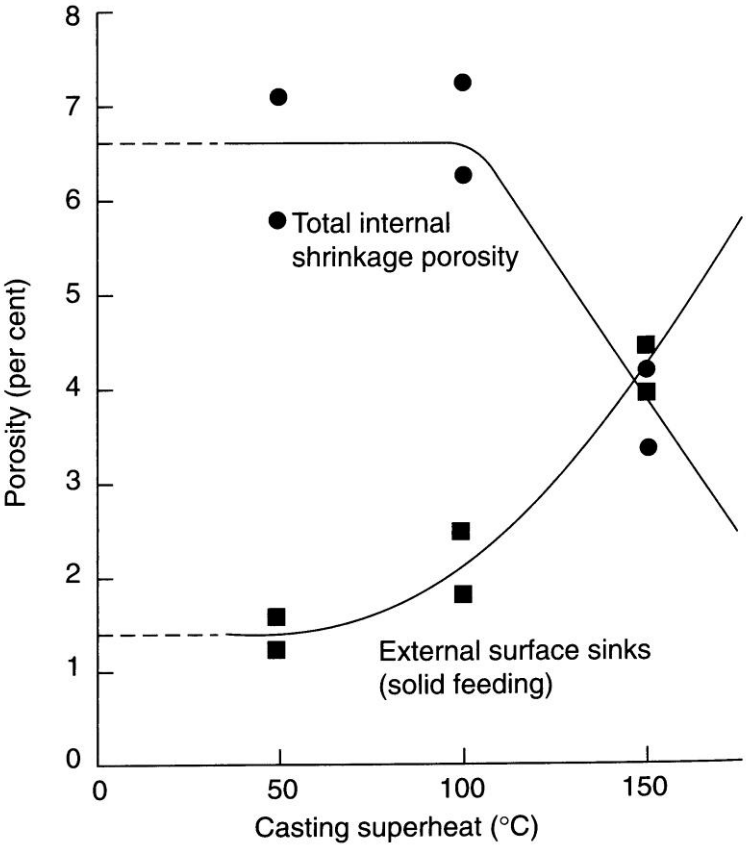

Figure 14: Al-12%Si Alloy casting into unfed shell moulds showing the full 6.6% porosity internal shrinkage at low casting temperatures then giving way to solid feeding at higher temperatures leading to external sinks. (Castings 2nd Edition Campbell 2003, original data from Harinath et al 1979)

These mechanisms act to counterbalance the loss of volume seen during freezing thus reducing shrinkage porosity. The effect then of hyper nucleation seen in the A20X alloy compared with a standard A201 alloy on the feeding properties during solidification poses an interesting, unanswered question. (Fuoco et a 1998) studied the effect of grain refinement on an A356 alloy. Fuoco and colleges studied the types of feeding present when casting bars in A356 with and without TiB_2 grain refiner.

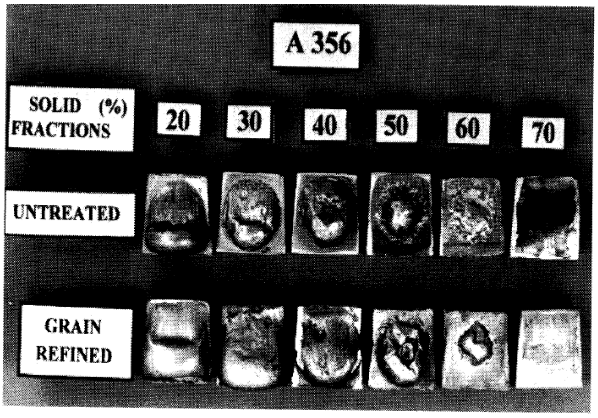

Fig. 9. Aspects of drops attached to bars after stopper remotion at 20, 30, 40, 50, 60 and 70% solid fraction in untreated and in grain-refined melts.

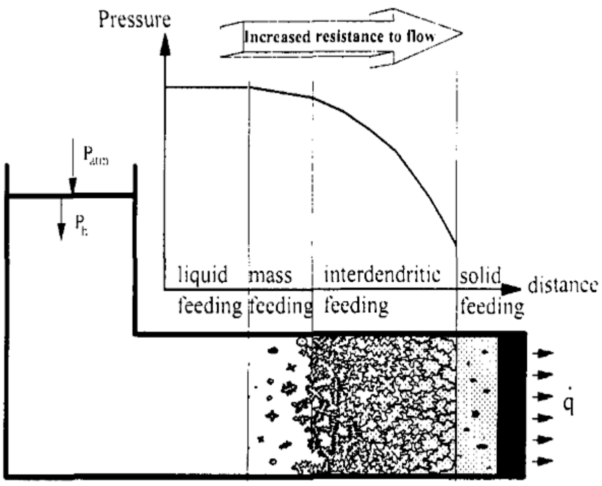

Figure 15: Aspects of Drops attached to bars after stopper removed at 20, 30, 40, 50, 60 and 70% solid fraction in un-treated and grain refined melts of A356 alloy (Fuoco et al 1998)

The bars had a steel sheet at one end acting as a stopper which was removed at varying solid fractions, 10-70%. The results showed a larger feeding capacity in grain-refined condition after the dendritic coherency point. Figure 15 shows more oozing of feed metal when grain refinement was increased. Metallographic detail showed that burst feeding was predominant in the grain refined TiB_2 A356 bars, whereas interdendritic feeding dominated the feeding in the untreated A356 alloy. Fuoco also goes on to suggest that grain refinement will increase mass feeding because the dendrite coherency point is delayed thus allowing more to occur. Work by (Dahle and StJohn 1998) into the effects of varying microstructure on the rheological behaviour of the mushy zone in an Al-Cu-Si alloys show that there is a significant change in shear strength in the mushy zone with varying microstructures (Al-Cu-Si with and without TiB_2 addition). Dahle indicates that dendritic coherency Tch and maximum packing fraction Tpk are lowered as dendrites become smaller and more globular in shape (figure 16).

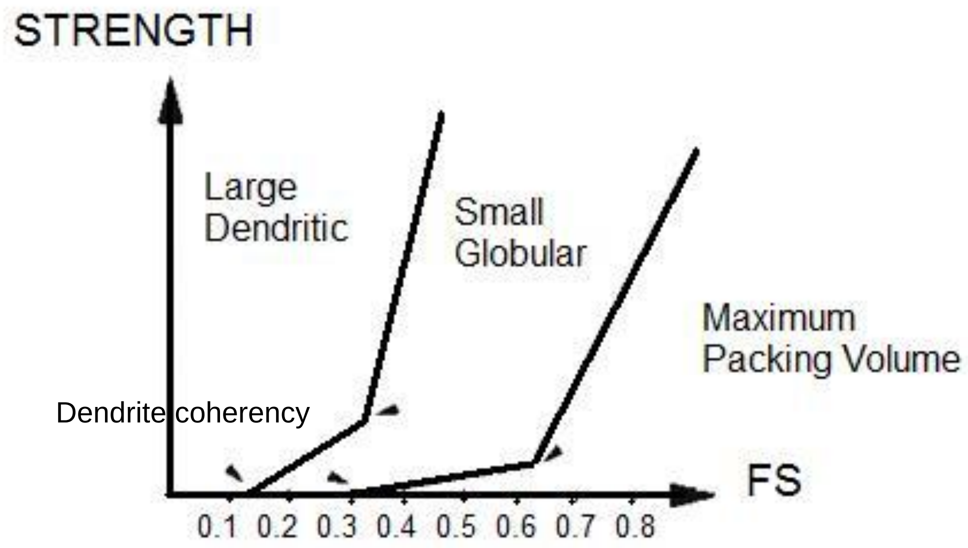

Figure 16: shows general behaviour of the increase of shear strength vs. solid fraction in the mushy zone for extreme microstructures: large dendritic and small globular grains (Dahle and StJohn 1998)

Larger more dendritic grains will interlock sooner thus decreasing the system's ability to feed effectively. The A20X microstructure has smaller more globular morphology and the work by Dahle suggests the feeding mechanisms at work have huge significance. The lack of study into the feeding mechanisms must be improved, with the need to establish the correlation between solidification characteristics and the feeding mechanisms involved during solidification.

2.10 Fluidity

The ability of a metal to flow through the gating system filling the cavity and conforming to the shape whist losing temperature and starting to solidify is an important property to understand when looking to improve casting practice and alloy integrity. (Flemings 1974) describes fluidity as the distance a molten metal can flow in a mould of constant crosssectional area before it solidifies. Fluidity is a complex property and is affected by a number of factors which can be split into three categories:

1. **Metal Variables:**
   - Chemical composition
   - Solidification range
   - Viscosity
   - Heat of fusion

2. **Mould and Mould/Metal variables**
   - Surface tension
   - Mould and metal thermal conductivity
   - Heat transfer coefficient and specific heat.

3. **Test Variables:**
   - Casting temperature (superheat)
   - Channel diameter
   - Applied metal head
   - Oxide/particle content

It is important to point out that fluidity data from aluminium alloys although not readily available yet is hugely important when looking to improve castability (Loper 1992). The two methods of evaluating fluidity are the spiral sand mould tests and vacuum tests which have been extensively reviewed (Di Sabatino et al 2005) and the accuracy of such tests are questioned continually as there are so many factors to control for and so this should be taken when analysing results from such tests. What is known is that casting temperature and alloy composition are the two largest factors affecting fluidity (Di Sabatino 2005).

The nature of the relationship between fluidity and solidification time is such that any increase in solidification time will increase fluidity (Campbell 2003). Increasing mould temperature or casting temperature will directly affect and improve fluidity in castings by keeping the metal above the freezing range for longer and was proved by the early work by Andrew (1936) when looking into the effects of temperature on fluidity in Fe-C alloys. A reduction in the rate of heat transfer will improve fluidity within a casting system. Al-Cu based A201alloy has poor fluidity at least in part because of its poor running characteristics but also mechanistically the early onset of dendrite formation during freezing causes a fragmented dendrite flow which develops into a slurry of growing dendrites which becomes 'thicker' and resists flow. Interestingly it has shown that grain refining is an effective way to increase the fraction of solid where dendrites form this interconnected network of dendrites or dendrite coherency point (Backerud et al 1996), meaning that the bulk metal had more time in a fluid, less structured state. It is therefore not unfair to make the assumption that grain refinement would improve fluidity properties of alloys with this addition. The literature however is much less definitive in this regard. Contrasting findings from Dahle and Arnberg (1996) between the two recognised methods for testing (spiral and vacuum tests) alone illustrates the lack of comparability and extrapolation between techniques and results when looking into this. Work by Chai (1994) however was in agreement with the assumption above when studying the effects of grain refinement in an Al-4%Cu alloy having found both an increase in fluidity and of the coherency point of the alloy. (Mollard et al 1987) however found the opposite in the same Al-4% Cu alloy when 0.15% Ti was added. The effect of grain refinement on fluidity in A357 and binary Al-Cu alloys using both spiral tests in sand

and the vacuum test in glass tubes was evaluated by Dahle and co-workers (1996). They found that average fluidity increased in an Al7%SiMg alloy with increased grain refiner above a certain level, 0.12%Ti in an Al5wt%Tiwt%B master alloy and below this level, fluidity was reduced. With Boron additions in Al-Si alloys they found increased fluidity and higher fraction solid at coherency which fits in with the above assumption made on dendrite coherency. Tirkayioglu and co-workers (1994) found there to be no effect on fluidity in alloy A356 when adding 0.04%Ti as a refiner in an Al5%Ti1%B master alloy. Given that many parameters (as talked about initially) affect fluidity and the need for improved, reliable techniques it is hard to fully understand the effects.

2.11 Hot-Tearing

Hot-tearing is a severe defect within a casting and can be described as the formation of an irreversible crack failure in a still solidifying casting either on the surface or within the casting. It is generally accepted that hot tearing occurs as a result of the stresses brought about by restrained solidification shrinkage and thermal contraction of a casting (Arnberg 2008). It occurs at a region of low strength and poor feeding into the mushy zone but is a complex phenomenon and there are a number of factors that affect its formation: alloy composition, process parameters such, mould properties and casting design (Eskin 2004). It is well established that of these factors alloy composition has the most profound effect on hot-tearing (Arnberg 2008).

Much in depth study has gone into understanding and determining the mechanism of hot-tearing, and reviews in the field completed (Eskin et al 2004), (Sigworth 1996). From the literature there two schools of thought can be used to categorise the driving force for failure:

1. Hot-tearing is based on stress, strain and their rates of change with relation to thermo-mechanical properties of the alloy (Pellini 1952); (Campbell 1969); (Metz and Flemings 1970); (Davidson et al 2006).

2. Hot-tearing is based on the feeding network during solidification and the metallurgical factors associated (Pumphrey et al 1948); (Saveiko 1961); (Clyne and Davies 1975).

The basic occurrence of hot-tearing in aluminium alloys is understood and attributable to both of the above fields of study and an overriding mechanism is still debated.

Aluminium-copper alloy systems are known for their susceptibility to hot-tearing. (Li 2010) assessed why some aluminium alloys hot tear and others don't by comparing castings of A356 with A206 alloys whilst varying the mould temperature (200, 300 and 370°C) and pouring temperature (superheat increments of 50, 100 and 150˚C from each alloys liquidus). No cracks were seen in any of the A356 castings in any condition. In all conditions the A206 alloy showed tearing. With the casting a 'T bar shape' and the known sites of tearing predictable, load onset temperature and crack initiation temperature both decreased with increasing mould temperature. This suggests mould temperature has a strong effect on hot tearing susceptibility in Al-Cu casting alloys, suggestions strongly agreed with by all workers in the field and is likely to be because of a reduced cooling rate and thus a reduced load development on the stresses and strains of the solidifying metal. Fortunately for aluminium alloys, hot-tearing can be almost eradicated form castings with much improved feeding systems and clean feed metal.

2.12 Casting Process Simulation

2.12.1 Overview of the basic premise of simulation modelling

Simulation modelling is the process of representing real phenomena using the laws of physics and mathematical equations implemented within a computer program. The real process of metal casting in whatever form is subject to many influences. It is therefore no surprise that to create a complete, physically accurate simulation that satisfies all the mathematical laws of these influences across all length scales is not feasible, so the most active and important factors are concentrated on. There are three major areas to consider when metal casting: casting material, casting geometry, and casting process; and when trying to simulate these, there are many other considerations to take into account that could affect the simulation:

1. **Casting Geometry** – features like sharp or smooth corners, whether there are holes, thick to thin sections as well as mould thickness all affect the flow and solidification of metal along with heat transfer of the cooling metal. The feeding system of the casting will have a huge impact on the end result.
2. **Casting Material** – Thermo-physical properties of the alloy, thermo-physical properties of the mould and metallurgical properties like grain structure need to be considered.
3. **Casting Process Parameters** – Filling/pouring rates, pouring temperature.

Thus a numerical process model is required to calculate fluid flow, heat conduction and phase transformation, utilising the thermophysical properties of the mould and casting materials and external boundary conditions. Examples of current such simulation software programs are: MAGMASOFT, ProCAST, AutoCAST and SIMTEC.

2.13.2 Modelling of Porosity

At the macro scale, prediction of porosity formation is less advanced than filling and general solidification but significant resources and time have been invested over the past two decades into development of high fidelity models. Taking the prediction of porosity in castings as a fitting and relevant example, the development of such a tool that will predict porosity during solidification from concepts like localised pressure drops and thus the nucleation and growth of pores has only recently been possible (Lee et al 2003). Before the prediction of porosity from first principles, early prediction tools used parameters that could be simply calculated from local (bulk) thermal parameters and be able to estimate the potential for pores forming. These are known as criterion functions. Section 2.16.3 describes these current functions and the original work used to derive or parameterise them. To predict porosity quantitatively and accurately however, better models are needed that take into account phenomena like the pressure of the interdendritic liquid feeding through the mushy zone during freezing as well as hydrogen solubility and evolution, secondary dendrite arm spacing and pore size. Concepts have been put forward to simulate for these factors based on their approach and reviews: (Lee et al 2001) and (Stefanescu 2005), define those as follows: interdendritic flow models, pore growth models and cellular automata models. These are the new approaches researchers are focusing on to develop more accurate modelling of porosity defects.

2.13.3 Criterion Functions

Criterion functions are a set of rules that relate casting solidification conditions for example cooling rate, solidus-liquidus interval and local thermal gradient to the tendency for porosity formation within an alloy system as a result of a debit in feeding effectiveness. These functions are based usually on statistical data from experiments (Tynelius et al 1994) and quantitative porosity results are used to calibrate criterion function values (for example: higher criterion value equates to higher porosity formation and eventually the creation of a criterion threshold limit whereby above a certain value, porosity is present) or the physics of one of the driving forces (Pellini 1953) which make up the overall form of the equations whilst the coefficients are experimentally fitted.

Table 2 summarises five criterion functions designed for modelling the solidification behaviour of casting alloys and their development reviewed below.

Table 2: Criterion functions for solidification modelling. (Fundamentals of Numerical Modelling of Casting Processes 2005: Jasper Hattel)

		Gradient	Cooling Rate	Flow Velocity during feeding	Solidifi-cation time	Solidifi-Cation speed	Dimension	Length scale exponent
Criterion	Pellini	G_s	-	-	-	-	Km^{-1}	-1
	Niyama	G_s	$T^{-½}$	-	-	-	K m s	0
	Hansen & Sahn	G_S	$T^{-¼}$	$u^{-½}$	-	-	K m s	0
	Xue	-	-	-	$t_s^{-½}$	-	ms	0
	Lee, Chang and Chieu	G_S	-	-	$t_s^{-⅔}$	V_S	Ks	

2.13.3.1 Pellini Criterion 1953

Pellini and co-workers collated a series of experimental data on feeding behaviour and defect formation in steel castings during solidification to draw some more applicable general concepts that could be widely accepted. By varying riser height in 0.2-0.3 percent carbon steel test bars along with varying the casting geometry from spheres to cylinders, long bars and large plates, Pellini concluded that it was metal and mould characteristics that affected solidification and that by using the volume to surface area ratio calculations, the heat transfer characteristics of the casting system establish the specific rates at which the solidification process proceeds. The castings and feeding systems could be designed in which the solidification proceeds progressively toward the feeder.

2.13.3.2 Niyama Criterion 1982

(Niyama et al 1982) built on the theory that ‘temperature gradient’ can be a simple and effective parameter of shrinkage prediction by studying centreline shrinkage in steel castings. Niyama, by determining the effect of casting size on the critical temperature gradient in differing grades of steel cylinders of differing diameter (3, 6 and 9cm) found that the critical temperature gradient was inversely proportional to the diameter of the castings leading to the development of a new parameter that was independent of the alloy, its size and shape as it corresponded well to the shrinkage distribution in the cast cylinders and larger production casts. In essence, by measuring porosity fraction along with the local thermal parameters cooling rate and thermal gradient, a criterion function was established that reflected the driving force for porosity formation based on the theoretical premise that shrinkage porosity forms at the base of dendrites due to a critical pressure drop and Darcy’s law of interdendritic liquid flowing through a porous medium (mushy zone). Experimental castings with shrinkage defects were produced and for those predicted in the model when the Niyama values for the steel castings were <1 the casting was seen to be sound. Values >1 indicate the presence of defects. It should be noted that the Niyama criterion is the most widely used as it is suitable for computer simulation due to its simplicity and limited parameters but is principally validated for short freezing range alloys that are skin freezing.

2.13.3.3 Hansen – Sahm Criterion 1988

Hansen and Sahm sought to improve the accuracy and breadth of applicability of the Niyama criterion. Using numerical simulation of Pellini's original work on cast steel plate and bar tests it was identified that the velocity of flow in round test bars was up to ten times higher than in the equivalent thickness of plates. By introducing a scaling factor, N, to the plates and bars of Pellini's work they found that the cooling rate, temperature gradient and flow velocity were also scaled by a factor; N^{-2}, N^{-1}, and N^{-1} respectively. They proposed a feeding flow velocity parameter, u, which computationally was based on Darcy's law of fluid flow and which removed the size-dependency of the function. Their numerical calculations on Pellini's work supported both a size-independent and shape-independent function.

2.13.3.4 Xue Criterion 1985

Whilst completing a masters degree, Xiang Xue developed the soon to be known Xue criterion (Xue 1985) for the prediction of shrinkage in carbon steel castings.The model is based on dendritic growth along with interdendritic feeding channels within a solidifying alloy system but the full details from the original work were unavailable. However (Tian et al

2003) describes the Xue criterion as establishing the relationship between the feeding channels and dendrite spacing. Tian explains that according to dendrite coarsening theory that the feeding angle θ varies with coarsening time and when θ = 0° shrinkage defects cannot be formed and when θ = 90° there is planar growth. This leads to a simultaneous solidification mode and unavoidable shrinkage but in doing so there must be a critical value θ_K where no shrinkage defects are formed. This value is determined by alloy composition and soundness requirements and is shape independent and through theoretical derivation a criterion was produced. When the criterion is not satisfied in the casting there will be defects. This criterion accounts for the dendrite structure and the temperature filed at the solidifying front with respect to feeding (Tian et al 2003).

2.13.3.5 Lee, Chang and Chieu Criterion (LCC) 1990

(Lee et al 1990) developed a new feeding efficiency parameter that utilised thermal gradient, local solidification time and solidus velocity to predict porosity formation in castings. Lee and co-workers used an Al7Si0.3Mg alloy to cast rectangular plate castings of a constant thickness and width (20 and 140mm respectively) but varying lengths (150 or 250mm) along with varying the riser size (40-110mm diameter) to model the interdendritic feeding using Darcy's law (Darcy 1856). They used the ideal gas law to link the final volume of porosity seen in a casting with the local pressure of the interdendritic regions of the mushy zone. Both metalostatic, atmospheric and localised feeding pressures were integrated into Darcy's law similar to Niyama, but different in that the pressure drop calculated included an additional thermal parameter; local solidification time. The LCC criterion fit well with experimental data but results were based on plates of a uniform thickness and it has not been shown how the criterion can be extrapolated to other geometries and sizes making it very much a size and geometry dependant criterion.

2.14 Comparability of porosity measurements and the Niyama criterion with experimental evidence

A study into the validity of the Niyama criterion with actual porosity results using an AlSi7Mg alloy was reported by (Liotti and Previtali 2004). Simple rectangular geometries with varying gating shapes were cast and optical image analysis used to quantify porosity. The results were then compared with the Niyama prediction for different areas in the casting and evaluated. They found that the criterion did correlate well with the areas of high and low porosity but underestimated the influence various feeding mechanisms have on the formation of defects (porosity) and consequently their severity. Actual values of porosity varied from 1% in the shorter castings to 20% in the longer section castings. The Niyama values varied from 0.2 to 0.5 in the eight cast bars castings validating the observation that values below one are not structurally sound and that aluminium alloys fall in the bracket N= 0.2-0.4.

Niyama criterion is the most widely used criterion as it is size independent, it has been used in many alloys to predict feeding related shrinkage porosity (Chiesa 1996) and (Morthland 1995). However by nature they are applied to the prediction of shrinkage porosity based on a grouped expression describing the thermal field. This is both dependant on the alloy, casting and geometry and with so many process variables the extrapolation of criterion functions in general to new alloys is not accurate. The application of criterion functions to evaluate porosity in solidification analysis is important but predicting the severity of defect formation quantitatively is very limited. Further reviews and comparisons of other criterion functions and their accuracy can be read; Suri et al 1992 and Viswanathan et al 1993.

CHAPTER 3 PROJECT AIMS

Within the literature review it has been identified that the highly grain refined alloy A20X is of interest to manufacturers of light weight high performance structures, such as the aircraft and premium automotive sectors. The microstructures arising are substantially different to those of normal cast aluminium alloys and it is therefore necessary to understand the mechanisms of feeding and how these can be reflected within commercial casting process simulation software for the design of components. It is the objective of the research reported below to:

1. To design and produce a series of castings of simple geometry in which porosity of differing extent is predicted throughout the volume and to quantify the effect of alloy and grain refinement on the resulting microstructure and porosity distribution. The alloys have varying levels of grain refinement and compositional elements but are based on the Al-4%Cu, A201 alloy. They shall be referred to as: Ingot (I) A201, Grain-Refined (GR) A201 and A20X throughout the project.

2. To develop, using the commercial casting simulation software MAGMASOFT, a solidification model of A201 and A20X alloys, measuring thermophysical properties where necessary and possible.

3. To calibrate the porosity module in MAGMASOFT to reflect accurately the effect of grain refinement on porosity distribution.

The work was undertaken as part of the Midland Aerospace Alliance Aerospace Technology Exploitation Programme on casting of A20X structural components, a project involving Aeromet International Ltd., Aero Engine Controls, London Scandanavian Metallurgical, Grainger&Worral Ltd and The University of Birmingham.

CHAPTER 4 EXPERIMENTAL METHODOLOGY

4.1. Cast Tooling Design

A series of three dimensional geometric shapes were designed in the 3D mechanical CAD program DS SolidWorks® to create a casting tool that would induce the development of large amounts of porosity in castings of the aluminium alloy A201. The cast shape chosen (figure 17) was similar to a 'keel' shape and shall be named as such throughout. Down sprue, runner and filter block dimensions were calculated for each design using a nomogram chart. Along with the 'keel' shaped casting block, all the elements of the running system were assembled into three dimensional models in SolidWorks® and saved as .stl files. (.stl files are triangular representations of 3D objects that a variety of industrial software programs recognise and interpret.)

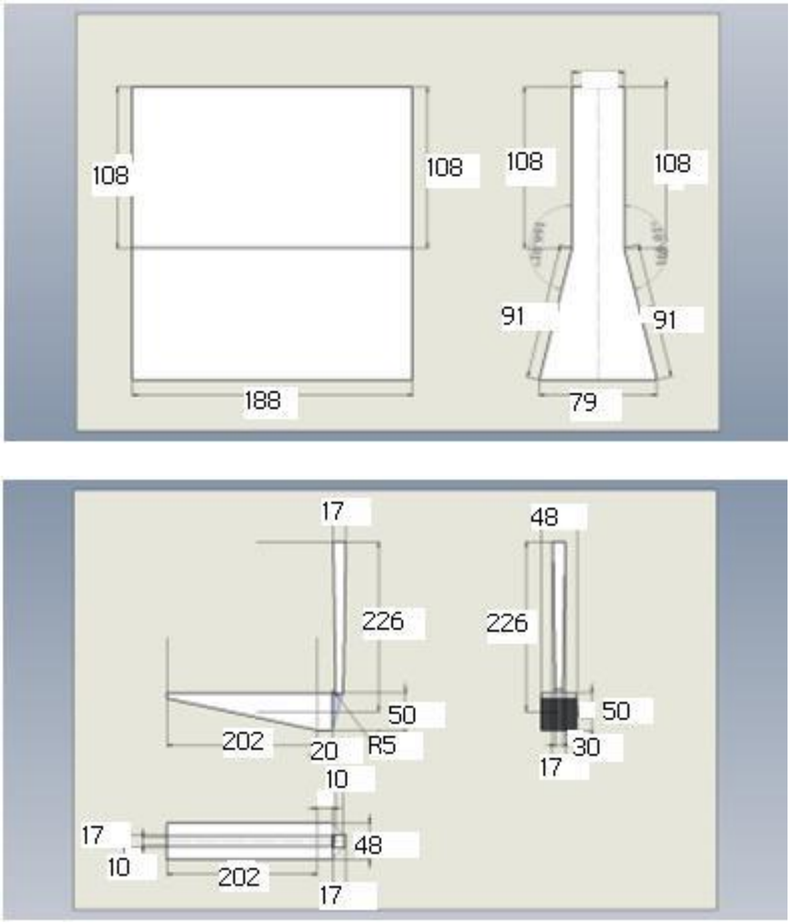

Figure 17: Dimensions and geometry of the down sprue, runner system and casting block in mm.

4.2 Casting Simulation

MAGMASOFT, a computer simulation software program was used to simulate the casting using an aluminium-copper $AlCu_4$, A204.2 alloy. The geometries of the casting system assembled in SolidWorks® were imported separately into the same ‘sheet’ as .stl files within the MAGMASOFT software.

4.2.1 Emeshment

Emeshment of the uploaded casting geometry is important as it can influence the outputs of the model. 99,216 elements were used to mesh the geometry. This number sufficiently reflects the nature of the geometry and provides enough detail for the system to accurately calculate flow behaviour and other outputs from the simulation. A higher element count increases the simulation time significantly. Figure 18 schematically represents the meshed geometry in MAGMASOFT.

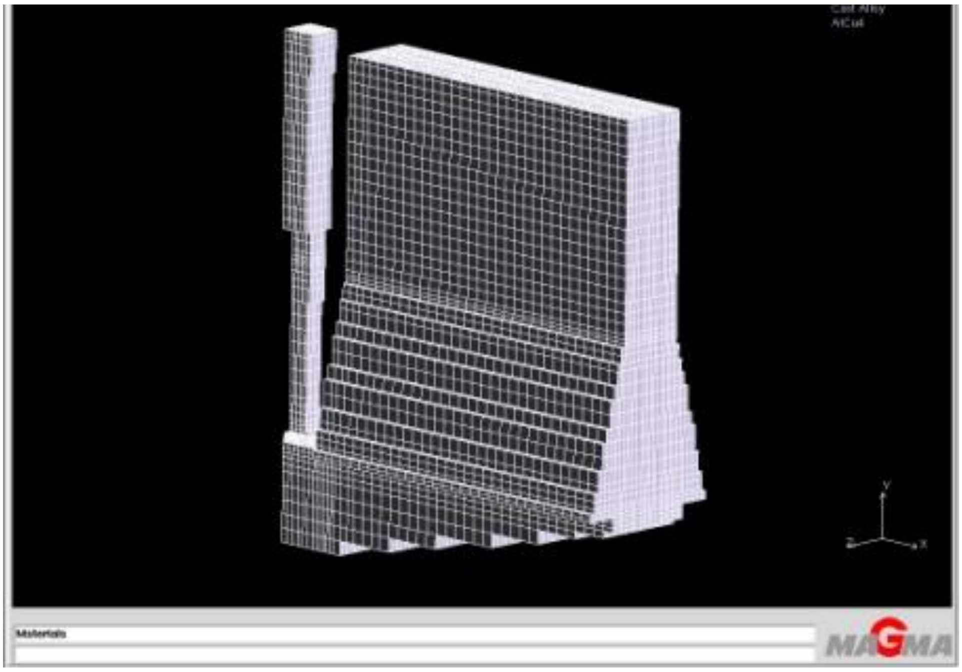

Figure 18: Emeshment of the casting geometry in the MAGMASOFT software.

4.2.2 Thermophysical/Material Property Data for MAGMASOFT

Each part of the cast has to be assigned a material and their properties known and recorded in order for the simulation to accurately reconstruct a casting simulation. In this case the cast metal was an Al-4%Cu alloy with solidus temperature 520°C, liquidus temperature 651°C, initial temperature 720°C and latent heat of 389.3 $kJkg^{-1}$ and whose total thermophysical property database can be seen in Appendix 1. The mould was defined as silica sand according to the standard MAGMASOFT material database. The interfacial heat transfer coefficient (IHTC) was set to a constant value of 1000 $Wm^{-2}K^{-1}$ (C.1000) but was also assessed at C.800 and C.600. Filling of the casting depended on a pressure boundary of 12 mbar metal head. Solver 4 was used to calculate filling.

4.3 Experimental Castings

4.3.1 The Alloys

Three alloys were used in this project: A20X, Grain Refined A201 and an Ingot A201 alloy. Table 3 below shows the compositions of each alloy in percent.

Table 3: Chemical composition (Wt %) of each of the three casting alloys

Alloy	**Ag**	**B**	**Cu**	**Fe**	**K**	**Mg**	**Si**	**Ti**	**V**	**Al**
A20X	0.70	1.33	4.07	0.02	0.07	0.26	0.05	3.17	0.04	90.29
IA201	0.72	0.01	4.41	0.05	<0.01	0.31	0.03	0.24	0.01	94.22
GR201	0.83	0.04	4.10	0.02	<0.01	0.30	0.05	0.28	<0.01	94.38

4.3.2 Mould Manufacture

Sand Moulds were produced from the tooling shown in figure 19 using a grade60 silica sand and a phenolic urethane two part resin binder (Pepset 5112 and Pepset 5230) using and addition of 0.6% of each by weight of sand mass. Moulds were made in three parts; the base/running system complete with filter slot, the down sprue and casting cavity (keelblock) and finally the pouring basin.

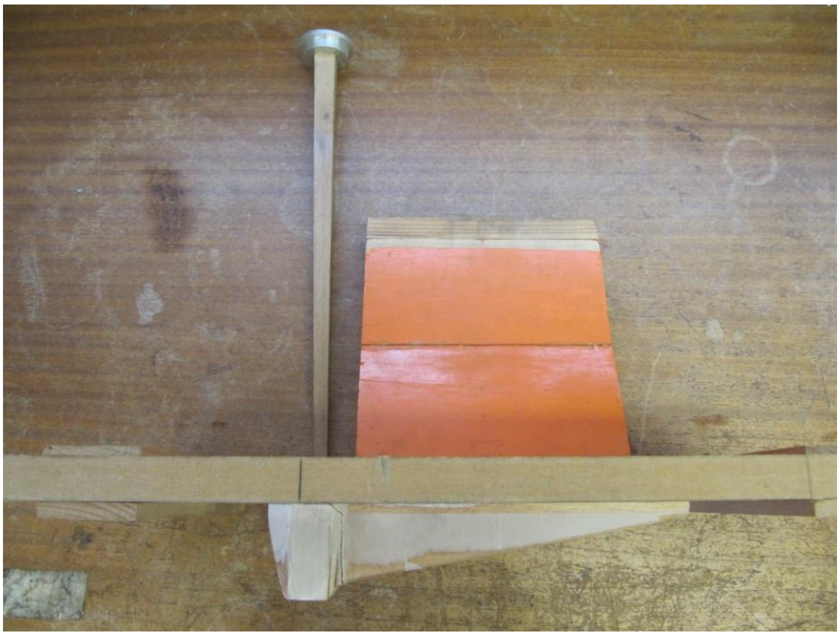

Figure 19: Tooling used to produce the sand moulds from which the three alloys were cast. Down sprue, runner system and mould

4.4 Temperature Measurement in Castings

For each casting produced, nine Type-K bare wire thermocouples were made. Double glass lapped 2mm Type-K thermocouple wire was obtained, sectioned, stripped of their glass fibre sheath and the spot welded (Voltage: 1V Speed: 40ms) creating a measurement junction. The welded junction was then layered in emulsion paint to electrically insulate it and ensure accurate recording of temperature at the tip.

These thermocouples were then placed along the centreline of the mould cavity at specific locations (Table 4) to map the thermal behaviour of the casting upon solidification. Holes of 3mm diameter were drilled through the casting using a pillar drill. The thermocouples then fixed in place with a nitrocellulose solvent based adhesive (Corfix). Figure 20 illustrates the thermocouples installed in a mould.

Figure 20: Images showing the thermocouple locations in the castings and how they held in position

All thermocouples were placed along the centreline of the casting which was 91mm across from either end.

Table 4: Shows the placement of the thermocouples along the centreline of each casting.

Distance from the bottom of the casting (mm)	**Alloy**		
	A20X	**GR A201**	**IA201**
160		TC4	
140	TC7	TC24	TC6
120	TC25		TC25
100	TC3	TC2	TC24
80		TC6	
60	TC27	TC3	TC4
60	TC24	TC25	
60	TC6	TC27	

4.5 Temperature Datalogging

Temperature/time measurements were carried out in each casting using ‘type-K’ thermocouples connected to an analogue-to-digital conversion board linked to a PC.

4.6 Melting and casting of the Ingot A201 and Grain-Refined A201

Grain refined and ingot A201 alloys were sand cast from production melts of A201 provided by Aeromet International, Worcester. A201 was melted in an induction furnace (Inductotherm-175R) in a clay bonded-graphite crucible. The charge of weight 9kg was degassed before pouring (see section 4.8 for degassing) and once at 720°C, was cast. An argon gas flow covered the crucible and the charge temperature checked with a Type-K thermocouple. Compositions of both alloys can be seen in table 3.

4.7 Melting and Casting of A20X Alloy

Continuously cast A20X ingots were supplied by Aeromet International. The composition is summarised in Table 3. The 9kg charge was melted in an induction furnace (Inductotherm-175R) and degassed before cast (see section 4.8 for degassing). The melt was cast at 810°C. There was an argon cover flow both in the melt and around the crucible and temperatures checked with a Type-K thermocouple.

4.8 Degassing

Each of the three alloys was degassed to using an appropriate industry standard method.

4.9 Microstructural Analysis (Porosity Quantification)

Castings were sectioned to obtain a set of 10, 1x1cm specimens from differing locations that could be used to measure and therefore accurately map porosity distribution within each casting. Samples were sectioned at the same eight heights as the thermocouple placements, see table 4.

4.9.1 Sample Preparation

4.9.1.1 Sample Mounting

The sectioned 100mm^2 samples were mounted in non-conductive Bakelite using a Struers sample mounting machine under high pressure and temperature for 10 minutes to create a standardized cylindrical mount for grinding and polishing.

4.9.1.2 Specimen Polishing

The sectioned 10mm^2 samples were mounted in non-conductive Bakelite and polished using an automatic Struers (TegraPol-35) polishing machine with a variety of grinding papers/polishing clothes diamond suspensions and loads in a specific sequence for varying times as summarised in Table 5. To prevent contamination in between each step, samples were washed in an ultrasonic cleaner, removing all prior diamond lubricating suspension from the sample surface before the next step. The rotating disc and sample block was also cleaned and rinsed after each set to prevent the cross-contamination of lubricants.

Table 5: Polishing protocol used for all three aluminium alloys including the polishing pads, lubricants, loads and durations.

Surface	Suspension	Dosing	Load (N)	Time (mins)
SiC 320	Water	Constant	20	1
MD-Largo	DiaPro Largo 9µm	6	30	3.30
MD-Mol	DiaPro Mol 3µm	8	25	3
MD-Nap	DiaPro Nap-R 1µm	9	25	1.30
MD-Chem	OP-S Final 0.04µm	10	15	1

4.9.2 Optical Microscopy (Porosity Identification/Quantification)

Specimens were examined using a Zeiss AxioScop2 microscope at varying magnifications (50x, 100x, 200x) to identify the microstructure. 50x magnification was chosen to capture and quantify porosity in all three castings. This magnification provided a suitable balance between accuracy and quantity of data. A set of images of each sample was then taken (50x Magnification) in a 4x4 grid (16 images) and K.S.300 software used to quantify the porosity found in each image. By converting each image into a greyscale (of which porosity is black) and finding the percentage of pixels in each image that were black this can be used as a direct quantification method of porosity distribution.

4.10 Microstructural Analysis (Grain Size Quantification)

4.10.1 Anodizing

Two samples from each casting condition (60mm and 120mm along the centreline) were anodized to establish their grain size. Samples had to be removed from their Bakelite mounts due to the material's partial conductivity and thus inability to anodize the metal surface. Samples were removed from the Bakelite by covering them in soft tissue; placing them on a smooth surface and inducing a brittle fracture to break the bond between the metal surface and the Bakelite. Samples were then re-polished by hand using the sample protocol as reported in Table 5.

Tetrafloroboric acid was used as the etchant for anodizing. 5ml of the HBF_4 was used in a 200ml solution with water. The etchant was poured into a conductive stainless steel bowl and the bowl connected to a power supply using 'micro crock clips and wires'. The sample was connected at the back to another wire which was also connected to the power pack to complete the circuit. The polished surface was the dipped into the etchant and a current run through it. It was found that applying a potential of 20volts for 1 minute was the optimum condition for these alloys given their size and composition.

4.10.2 Optical Microscopy using Polarising Light (Grain Size Identification)

A Leica Leitz DMRX microscope with a polarizing light source was used to obtain colour micrographs of the anodized samples in order to quantify the grain size and structure of selected areas (centreline samples at: 60mm and 120mm from the top of the casting) in each casting in each condition. KS.300 software package was used to post process and analyse the images.

4.11 Differential Scanning Calorimetry of A20X

4.11.1 Sample Preparation

Two samples of A20X and IA201 were prepared for DSC analysis. Charges of 9.65Kg of the IA201 and 14.65Kg of A20X alloys were melted in graphite crucibles using an induction furnace and heated to 700°C. Once at 700°C the metal was ‘spatted’ onto an aluminium chill (which was polished and de-greased with acetone to remove possible contaminants) using a ‘sample scoop’ to create small beads of shot. It was not possible to produce shot small enough for the ceramic (alumina) DSC pans so thin cylindrical discs were cut from the rapidly cooled beads. Samples were cut to be as close to 30mg in weight as possible and measured. The alumina pans were first weighed and their weight stored onto the scales’ memory, the samples were then added to the pans and the weight recorded.

4.11.2 Alumina DSC Pan Preparation

The alumina DSC pans used for the DSC analysis were fired in a furnace for 15 hours at 800°C prior to use to ensure refractory dust and particles from the manufacturing process of the pans had been burnt off to eliminate interference during each cycle.

4.11.3 A20X Specific Heat Capacity Measurement

A high temperature DSC (Netzsch Petraeus 404C) was used to measure the specific heat capacities of solid and liquid A20X using sapphire standards. A20X from the chill cast described in section 4.11.1 was used. The sample was cut to a flat circular disc shape which would fit into the DSC alumina pans perfectly and weighed 30.31mg. The alumina pans underwent the sample pre-cycle treatment described in section 4.11.2.

The thermal cycle the samples underwent to calculate Cp on cooling is as follows:

1. Run 1 – Two empty pans with lids were heated from room temperature (20°C) to 720°C at 15°C/min. The pans were held for 30 minutes at 720°C and then cooled at 3°C/min to 450°C and then held at this temperature for a further 30 minutes. This run was to establish a baseline for the DSC.

2. Run 2 – Synthetic sapphire was then placed into one of the pans in the form of a disc. The previous procedure was repeated as described in Run 1. This established the values from which Cp was calculated.

3. Run 3 – The A20X sample then replaced the synthetic sapphire in the pan and the thermal cycle repeated again.

The thermal cycle used to obtain the specific heat capacity of A20X on heating was the same as the cooling cycle except samples were heated to 450°C at 15°C/min and then heated at the same rate (3°C/min) to 720°C. There was a 100cc/min flow rate of pure argon though the system during all cycle runs.

Having collected the three sets of data from each run on heating and cooling, the well established 'ratio method' was used in the DSC computer software (Proteus Netzsch) to obtain the specific heat curve for the sample.

The ratio method is given by (Overfelt et al 2002):

$$\frac{\quad}{\quad}\frac{\quad\quad}{\quad\quad} \tag{4.1}$$

Where $Cp;_s$ = sample specific heat, $Cp;_{std}$ = specific heat of sapphire standard, m_s = mass of sample, m_{std} = mass of standard, $\Delta\mu V_s$ = differential microvolt signal between the baseline and the sample, $\Delta\mu V_{std}$ = differential microvolt signal between the baseline and the standard.

4.12 Thermal Analysis of A20X, GR A201 and UGR A201

In order to use MAGMASOFT, fraction solid curves are required as a function of temperature. For the thermal analysis of each of the three alloys, the same experimental method was followed as described below.

A small lidded graphite crucible of internal diameter 30 mm, height 20 mm and wall thickness 10 mm was used to contain a molten charge of each alloy whilst a type K thermocouple inserted through the lid into the geometric centre of the sample was used to record the temperature/time data throughout solidification.

A 1kg charge was heated in a separate crucible in an EMA Pyrotherm furnace along with the empty crucible and thermocouple attached to the lid to 850°C. Once at 850°C the liquid A20X along with the crucible and lid were then taken out of the furnace, placed on a ceramic brick in a still air environment and the alloy poured into the crucible until full. The lid was then placed onto the crucible and the thermocouple submerged into the liquid and temperature-time data recorded at a rate of 10 s^{-1} until the temperature has reached around 350°C (fully solid).

4.13 MAGMASOFT Model Calibrations

A user-defined material was created in the MAGMASOFT software. The thermophysical properties were changed from the original $AlCu_4$ alloy in the software to the ones based on the experimental data calculated for A20X and sought from the open literature. Calculated data was directly inputted into the software and then the new material assigned in the simulation. The feeding effectiveness parameter in the model was then modified over a range to try and find a correlation with the experimental data.

CHAPTER 5 RESULTS

5.1 Thermal Analysis of A20X

Figure 21a summarises the cooling curves obtained using the method set out in section 4.13 of the methods for each of the three alloys: IA201, GRA201 and A20X. The individual cooling curves and their associated derivatives are figures 21b), c) and d). From this data the following solidus and liquidus temperatures were extracted and shown in table 6.

Table 6: Liquidus and Solidus temperatures for the three alloys determined by thermal analysis

Alloy	Liquidus Temperature (°C)	Solidus Temperature (°C)
IA201	658.4	509.9
GRA201	660.1	519.5
A20X	655.0	525.4

It should be noted that these values for both liquidus and solidus of each alloy are physically unrealistic. There is a systematic error present with an offset of approximately 10°C relative to the DSC data for the A20X alloy reported in section 5.12.2.4. In all subsequent analysis, all temperatures between the liquidus and solidus temperatures were scaled in linear proportion over the solidification range. The two arrows in figure 21a) indicate abrupt changes in cooling rate on the curves signalling the start and end of solidification. There is a marked difference in the rate of solidification for the ingot A201 alloy compared with the other two but this is most likely due to less metal being poured into the graphite crucible.

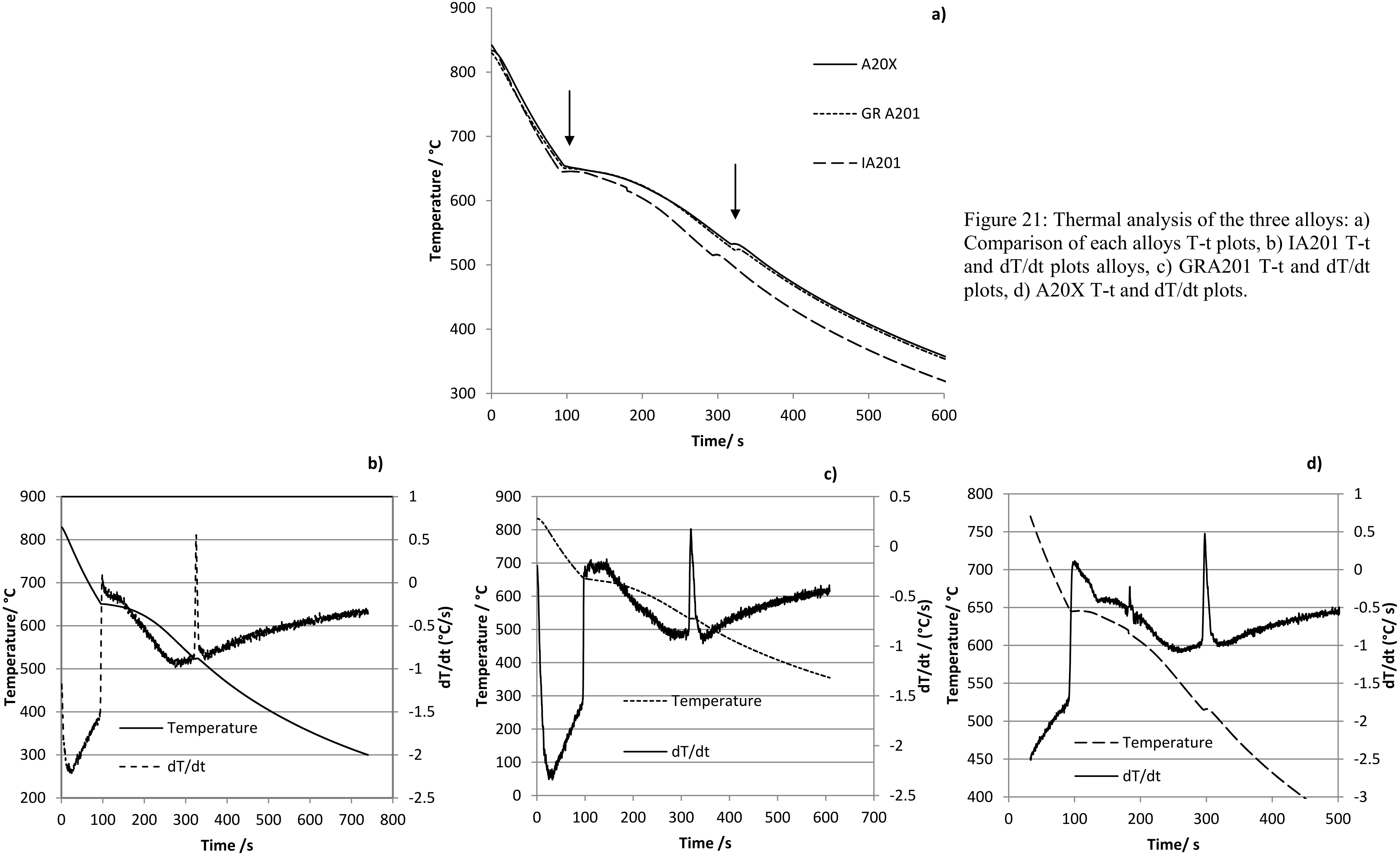

Figure 21: Thermal analysis of the three alloys: a) Comparison of each alloys T-t plots, b) IA201 T-t and dT/dt plots alloys, c) GRA201 T-t and dT/dt plots, d) A20X T-t and dT/dt plots.

5.2 Fraction of Solid Curves for the alloys

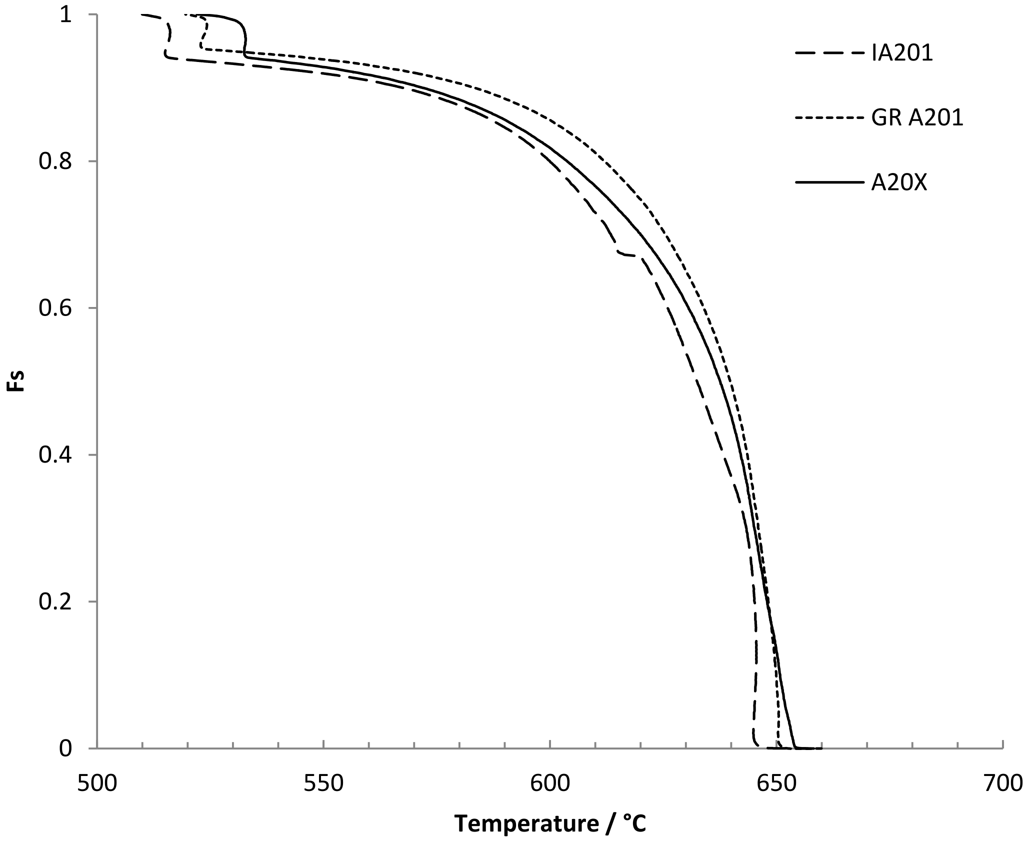

Figure 22: Fraction of solid curves calculated from the thermal analysis of each alloy: IA201, GR A201 and A20X.

The temperature-time data sets from the thermal analysis experiments seen in figure 21 were used to calculate the fraction of solid curves for each alloy (figure 22). A method based on the work by (Savitzki and Golay 1964) for smoothing and differentiation of data by simplified least squared procedures was used. A 17 point quadratic best fit curve and derivative function was used to obtain the instantaneous cooling rate *dT/dt* (figure 23).

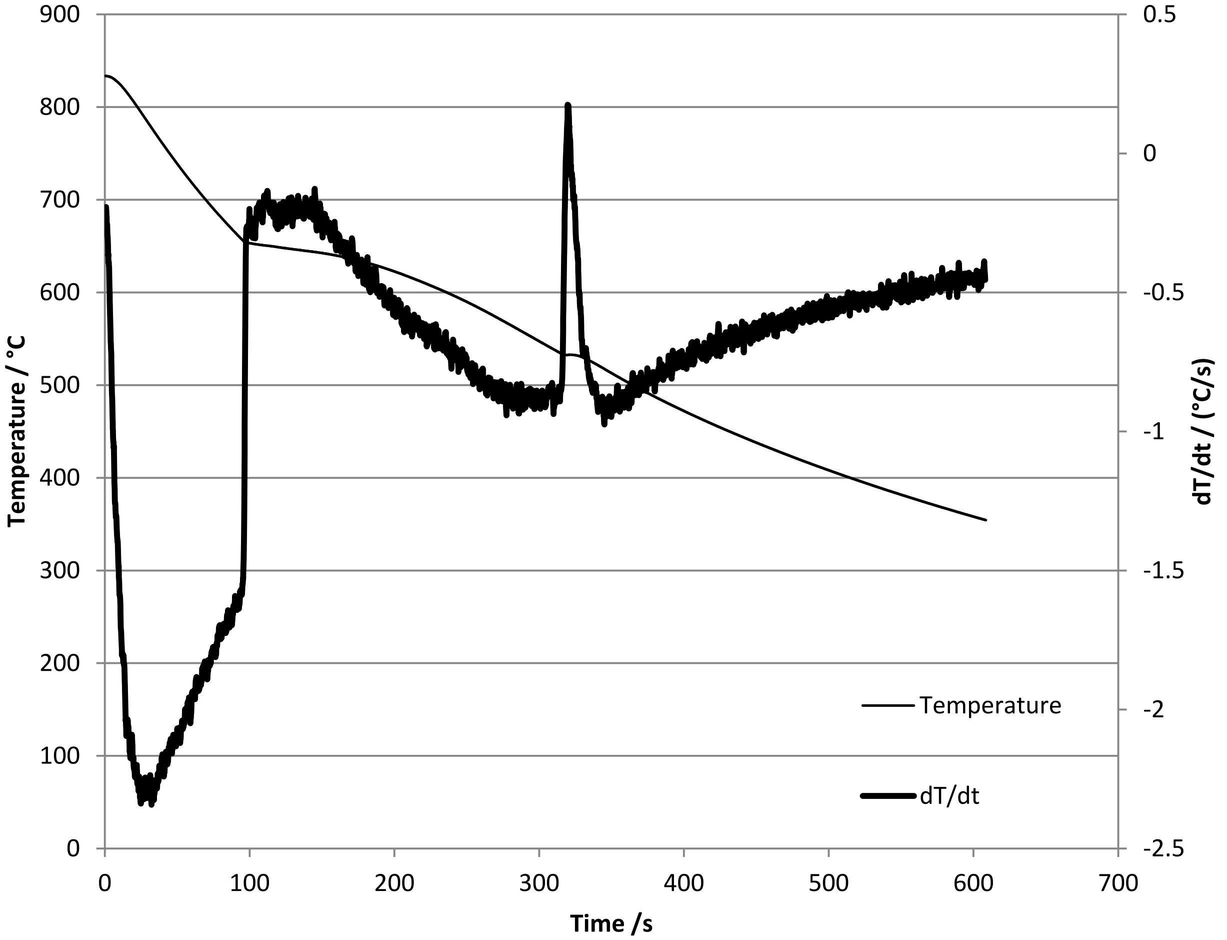

Figure 23: A graph showing the instantaneous cooling rate dT/dt as a function of the cooling profile for the A20X alloy.

Cooling data from before and after solidification, in which only specific heat of liquid and solid respectively is released was used to establish a 'baseline' cooling curve for the system as a function of temperature. By fitting a third order polynomial to the *dT/dt* data either side of the solidification range (Figure 24). By way of an example data processed for A20X is shown in Figure 25 (interpolated baseline derivative) points and the interpolated baseline appended to the derivative curve over the solidification range.

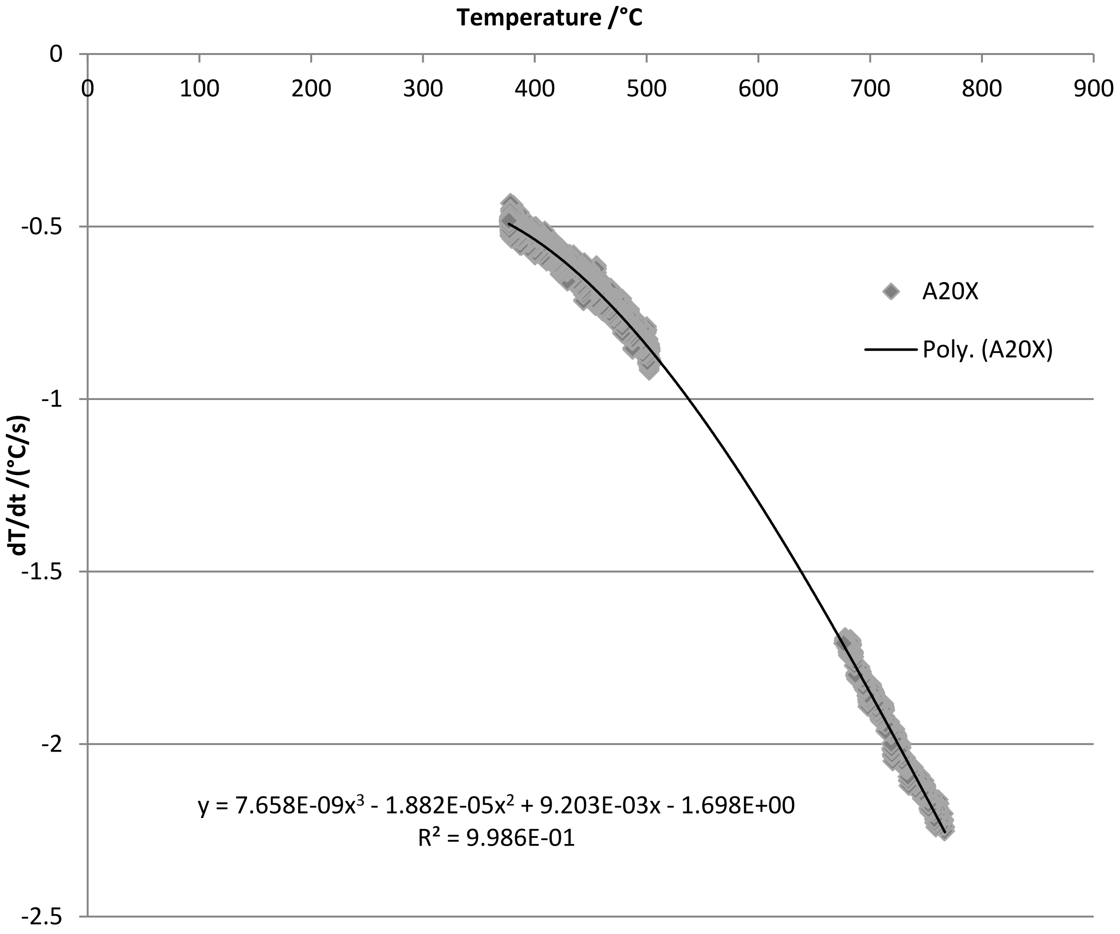

Figure 25: The construction of a baseline for the solidification range of the A20X alloy by fitting a 3rd order polynomial to the instantaneous cooling curve rate dT/dt

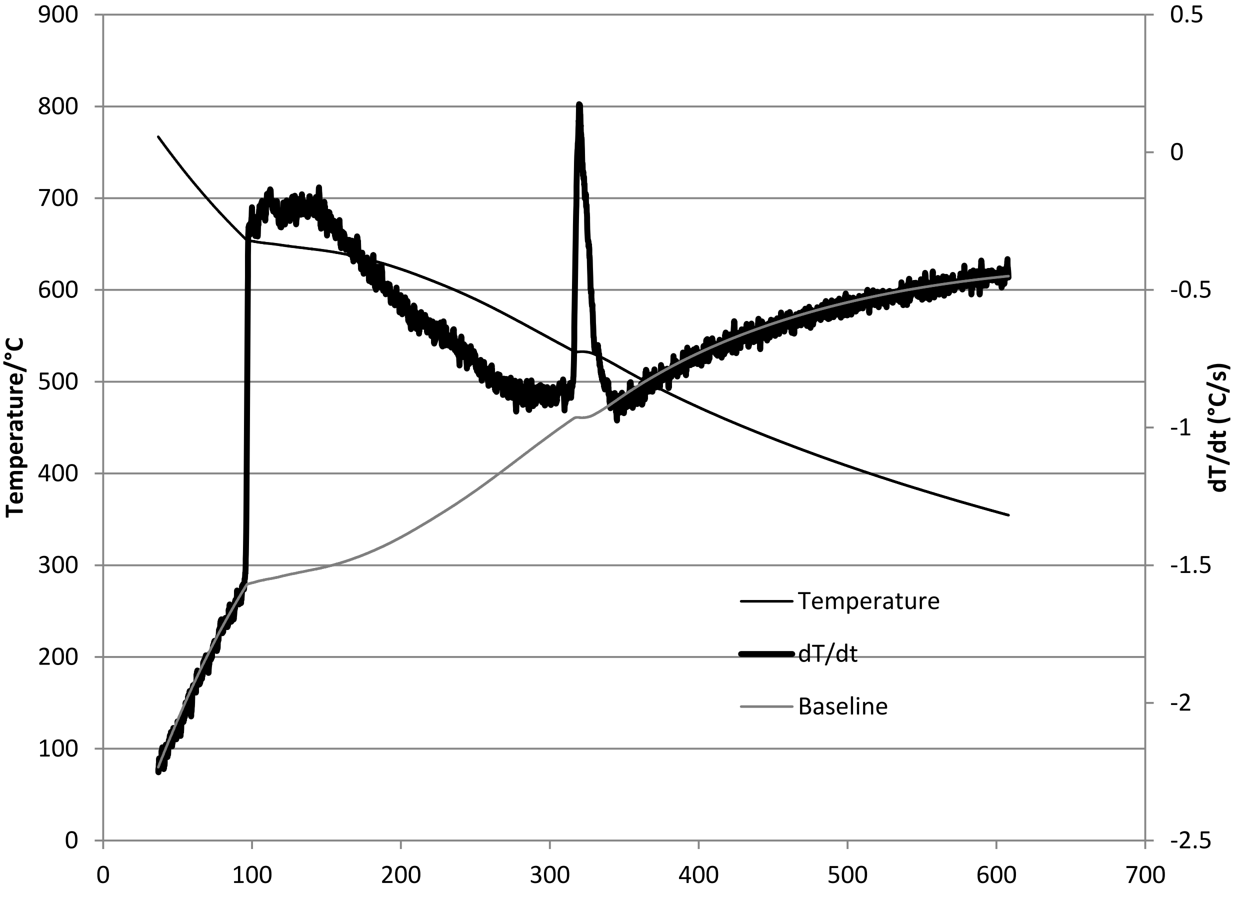

Figure 24: Collation of the temperature cooling curve, its derivative the instantaneous cooling rate and the interpolated baseline for solidification based on the 3rd order polynomial fit

5.2.1. Solid Fraction Calculation

Solid fraction was calculated using the relationship:

— — — (5.1)

where f_s = fraction of solid

C_p = specific heat capacity of the semi-solid alloy

ΔH = instantaneous change in entropy (latent heat) in time step *dt*

T = temperature

t = time

So by integration, — —— (5.2)

Where —— denotes the difference between the actual (measured) cooling rate and the baseline rate —

A solution for the fraction solid (f_s) was found in the following iterative manner:

1. The fraction solid was initialised based on the linear assumption that:

—— (5.3)

T = Instantaneous temperature

T_s = Solidus temperature

T_L = Liquidus temperature

2. Cp was calculated using the relationship:

(5.4)

It should be noted that due to the majority phase of the alloy being aluminium dendrites both the heat capacities of the liquid and solid and latent heat of fusion were derived from data for aluminium as reported in (Smithells Light Metal Handbook 7th Edition 1998).

3. ΔH was calculated using the relationship:

(5.5)

Where: denotes the change in fraction solid between the current and previous calculation step.

4. f_s was calculated for each time step and summed. This yielded a numeric value of f_s >>1
5. f_s was normalised to the range 0 – 1 over the temperature range T_L to T_s
6. The newly calculated f_s curve was used to initialise the next iteration to calculate the f_s curve. Normally, the calculation converged after 2 to 3 iterations.

Figure 26 shows the fraction of solid curve that was inputted into the MAGMASOFT material database. It is made up of a series of selected points that sufficiently represent the behaviour of the fraction of solid curve in figure 22 that is made up of many tens of thousands of points.

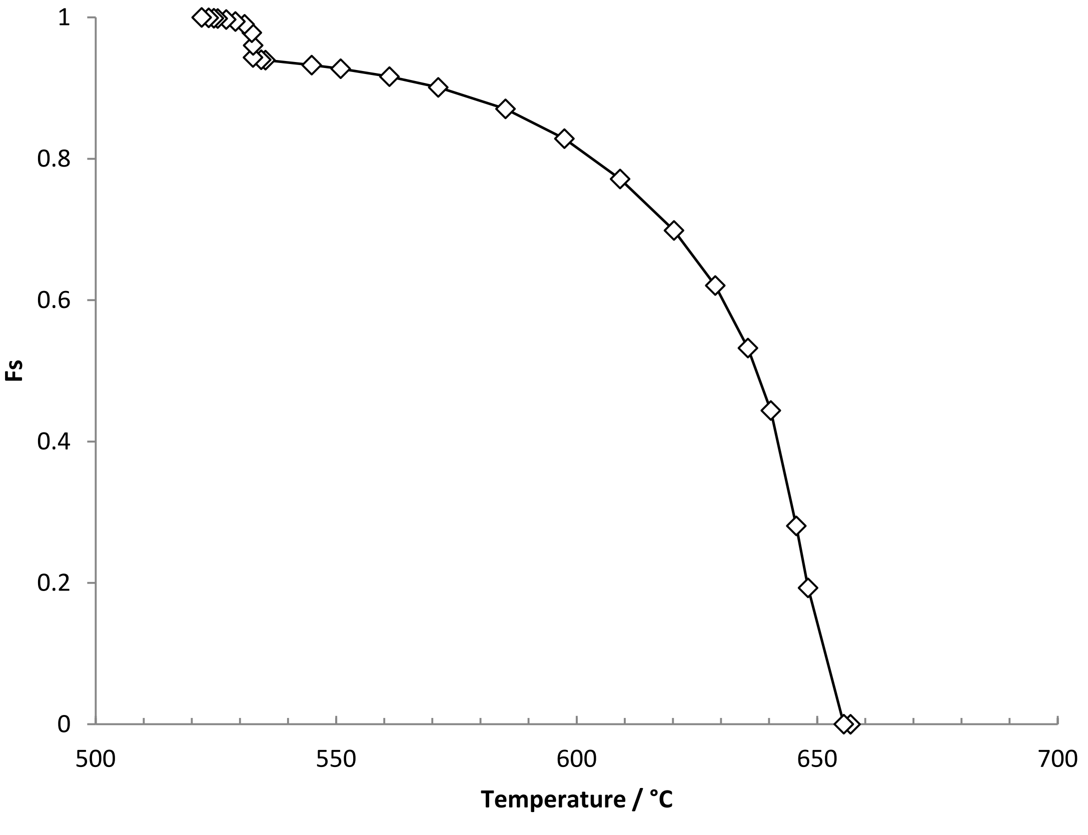

Figure 26: Fraction of solid curve (f_s) that was inputted to modify the MAGMASOFT casting model.

5.4 Initial MAGMASOFT Simulations

Initial simulations were performed to establish a casting system (down sprue, runner, casting shape, alloy and casting type) that would produce varying amounts of porosity when the effectiveness of feeding was altered to better determine feeding effects and grain refinement. Figure 27 shows the results from preliminary MAGMASOFT simulations, specifically the variation in porosity distribution and severity with increasing feeding effectiveness and a constant interfacial heat transfer coefficient (IHTC).

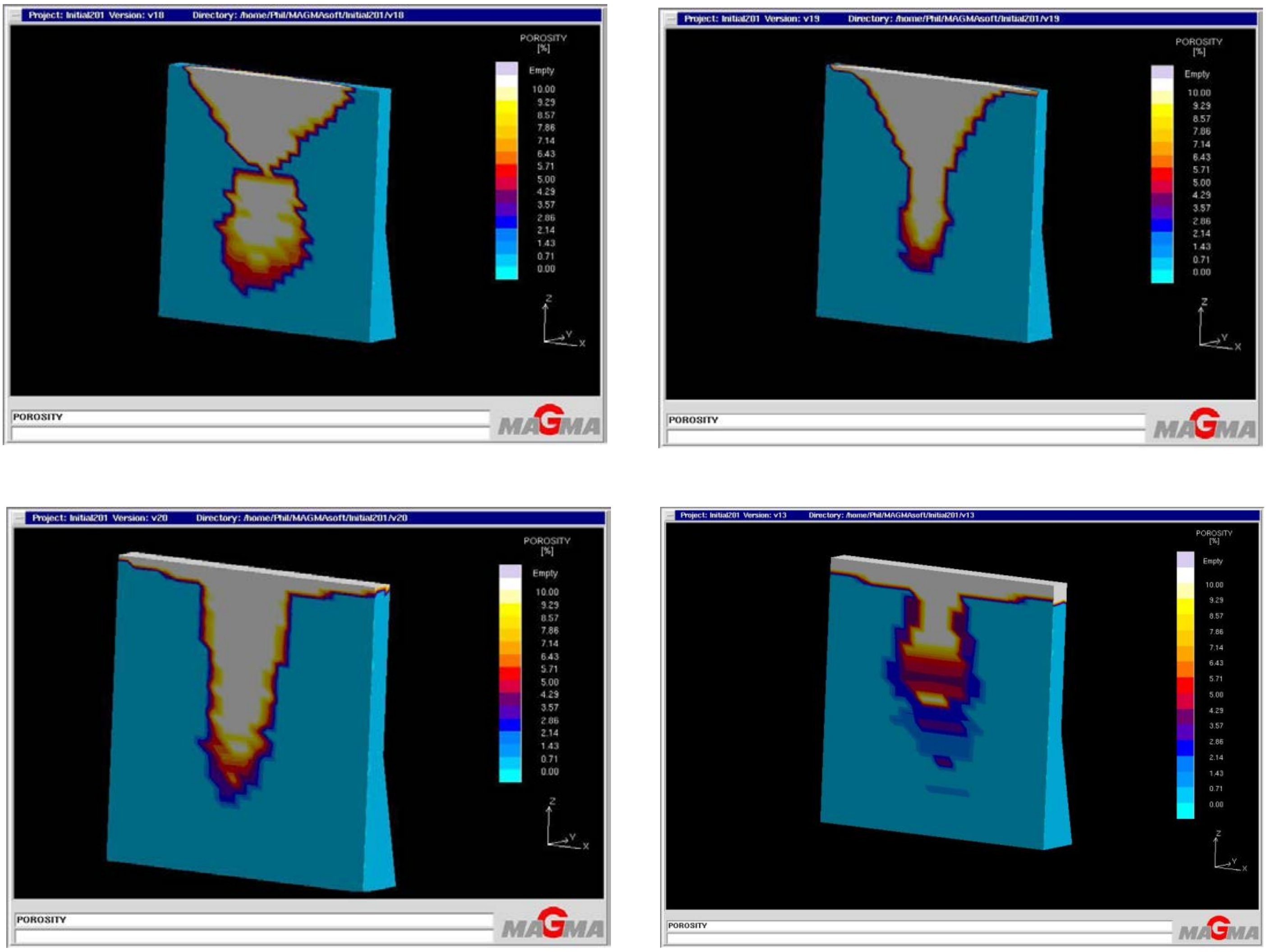

Figure 27: MAGMASOFT simulations of a sand cast Al-4%Cu alloy with varying feeding effectiveness, a) 10, b) 30, c) 50, d) 80% and the pattern of porosity formed as a result of the casting conditions (constant interfacial heat transfer coefficient of 1000 $Wm^{-2}K^{-1}$).

Clearly from Figure 27 there is a difference both in the amount and distribution of porosity in the sand cast Al-4%Cu simulations, going from a severe bulb-like structure formation that appears isolated from the top of the casting in the 10% feeding effectiveness condition, through to a more connected tongue-like formation that begins to reduce in length to the top of the casting as the feeding effectiveness increases. Simulations indicate that a change in the feeding effectiveness of an alloy cast into the mould substantially affects the porosity distribution.

5.5 Virtual Thermocouple Data

Figure 28 shows virtual thermocouple temperature data along the centreline from the Al-4%Cu sand casting in two differing thermal conditions. Image a) shows the cast simulation with an IHTC of C.600 $Wm^{-2}K^{-1}$ and image b) with an IHTC of C.1000 $Wm^{-2}K^{-1}$. Figure 28 shows that there is no significant change in either of the two sets of cooling curves with each corresponding thermocouple showing each step transition at almost identical times. This illustrates that for this casting system the IHTC has no significant effect on thermal properties. It should be noted that the virtual thermocouples were placed in identical locations to those of the thermocouples used in the real castings.

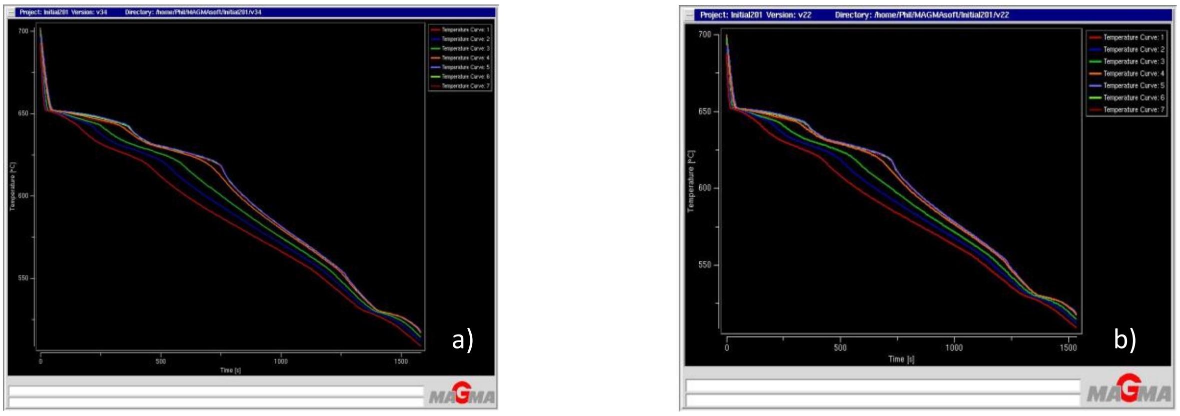

Figure 28: Sensitivity study looking at the effect of the interstitial heat transfer coefficient (ITHC) on solidification: a) C.600 $Wm^{-2}K^{-1}$ b) C.1000 $Wm^{-2}K^{-1}$on the virtual thermocouple temperature-time data from solidification of an Al-4%Cu alloy using MAGMASOFT. From the two images there it appears that the ITHC makes no difference to the cooling rates.

5.6 Thermocouple data from the IA201 casting

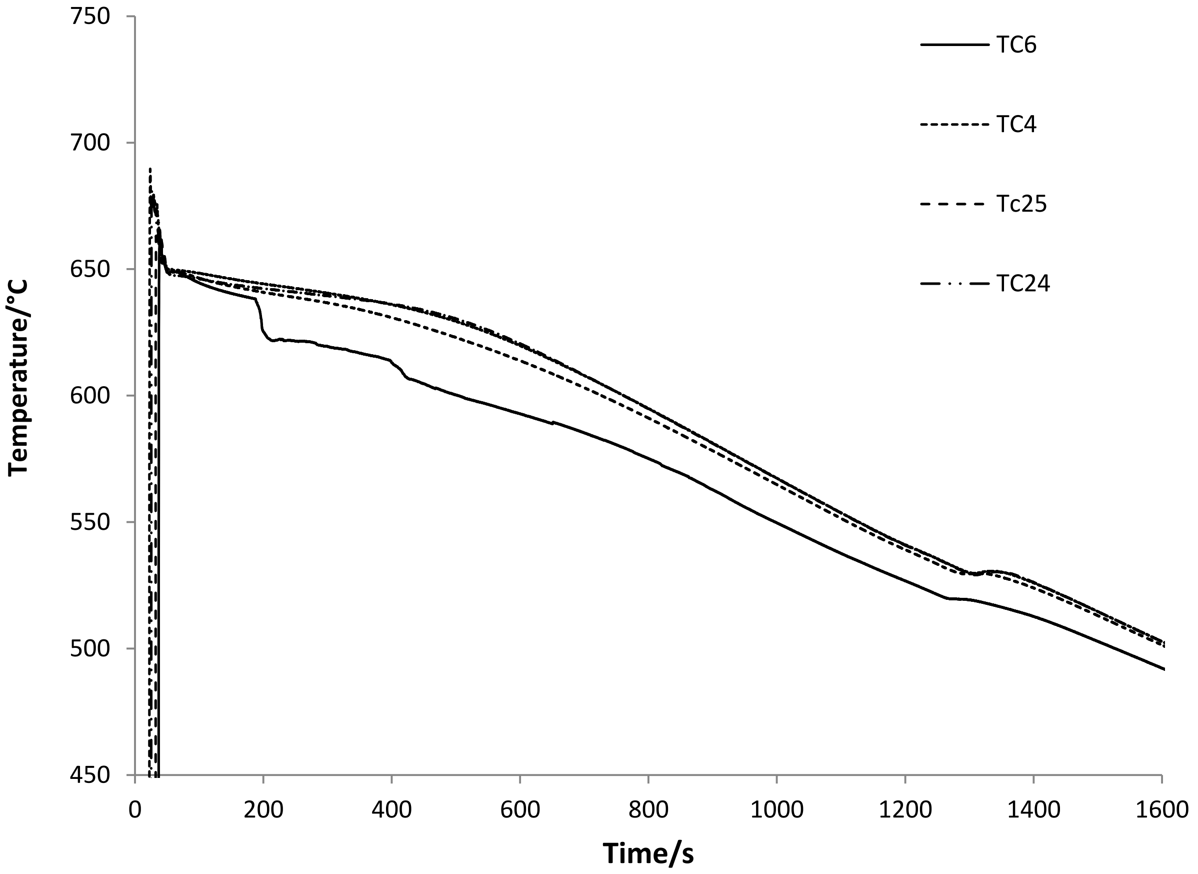

Figure 29: Thermocouple solidification data from the un-grain refined A201 casting at different points along the centreline of the casting.

Figure 29 shows the four curves corresponding to the four thermocouples that successfully recorded the temperature during the cooling of the IA201 casting. They clearly captures the start and end of solidification with initial deflection at approximately 660°C and then again at 520°C. Table 2 shows the thermocouple locations in the casting.

TC6 appears to have experienced interference on the signal during freezing. The cooling curve (solid line) has three noticeable step-like changes compared with the other data which have a smooth transitional curve from the start until the end of solidification. TC6 is also cooling much faster than the other thermocouples as it reaches the solidus temperature faster than the remaining thermocouples. This was due to an intermittent fault on the data capture system and could not be resolved in the time available.

5.7 Thermocouple data from GR A201 casting

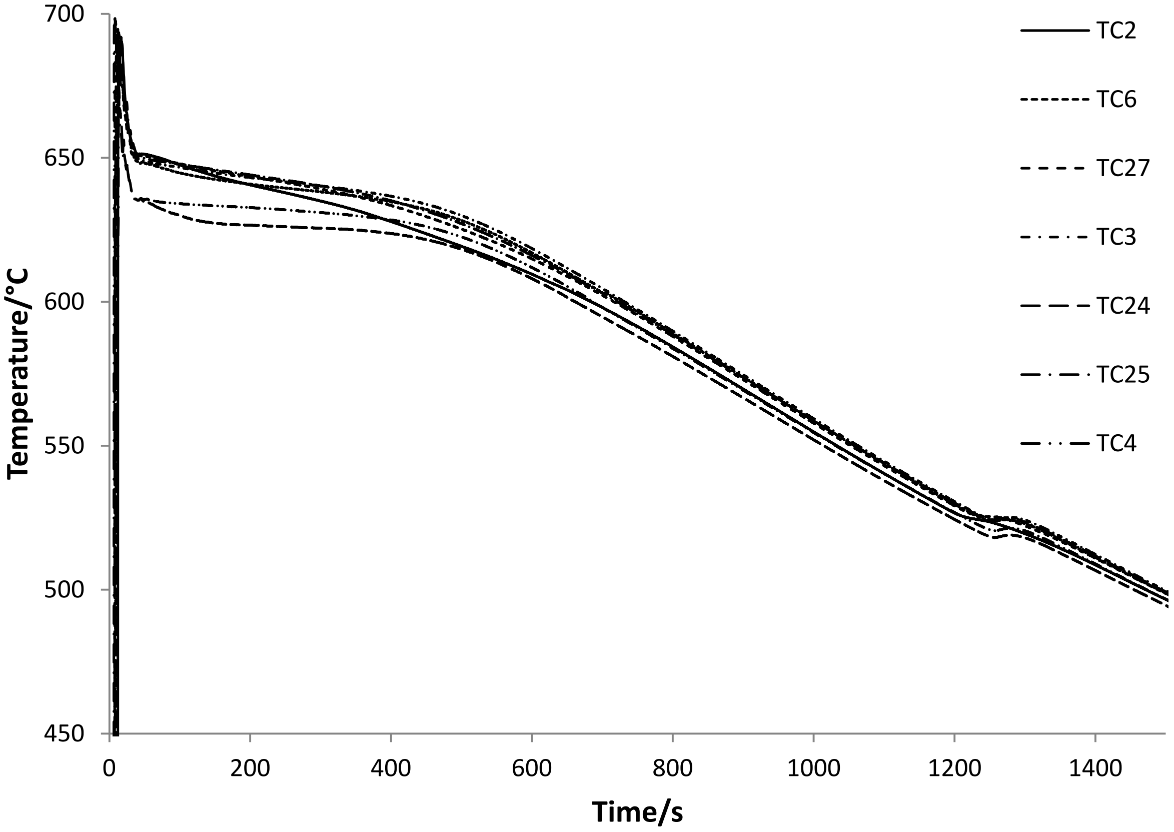

Figure 30: Temperature/time data from the grain refined A201 casting at different points along the centreline of the casting during freezing.

Figure 30 shows thermocouple profiles for grain refined A201 with solidification in the range 660.1°C and 519.5°C. TC4 and TC24 have recorded solidification starting at a lower temperature. This is likely to be the formation of small gas bubbles around the thermocouple tips from the organic binder in the paint used to prevent short circuits.

5.8 Thermocouple data from A20X casting

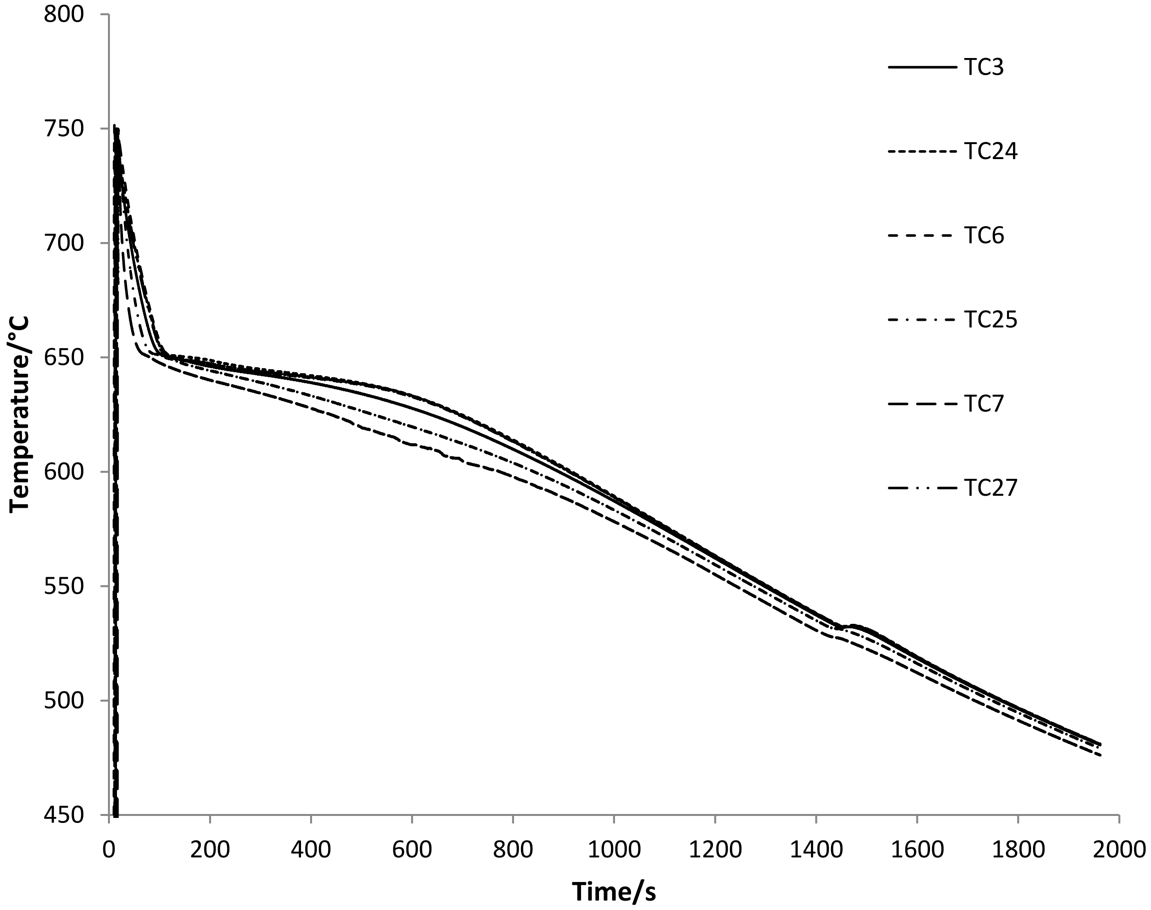

Figure 31: Temperature/time data from the A20X casting at different points along the centreline during freezing.

Figure 31 shows thermocouple traces obtained from the A20X alloy in differing positions along the centreline of the casting. The first noticeable difference is that in this figure the casting temperature is elevated (cast temp: 750°C) compared with the grain refined and ingot A201 alloys which were cast at 700°C. For all three castings a general statement can be made that solidification proceeds from the top section into the body of the keel block.

5.9 Porosity Analysis and Quantification of the three alloys

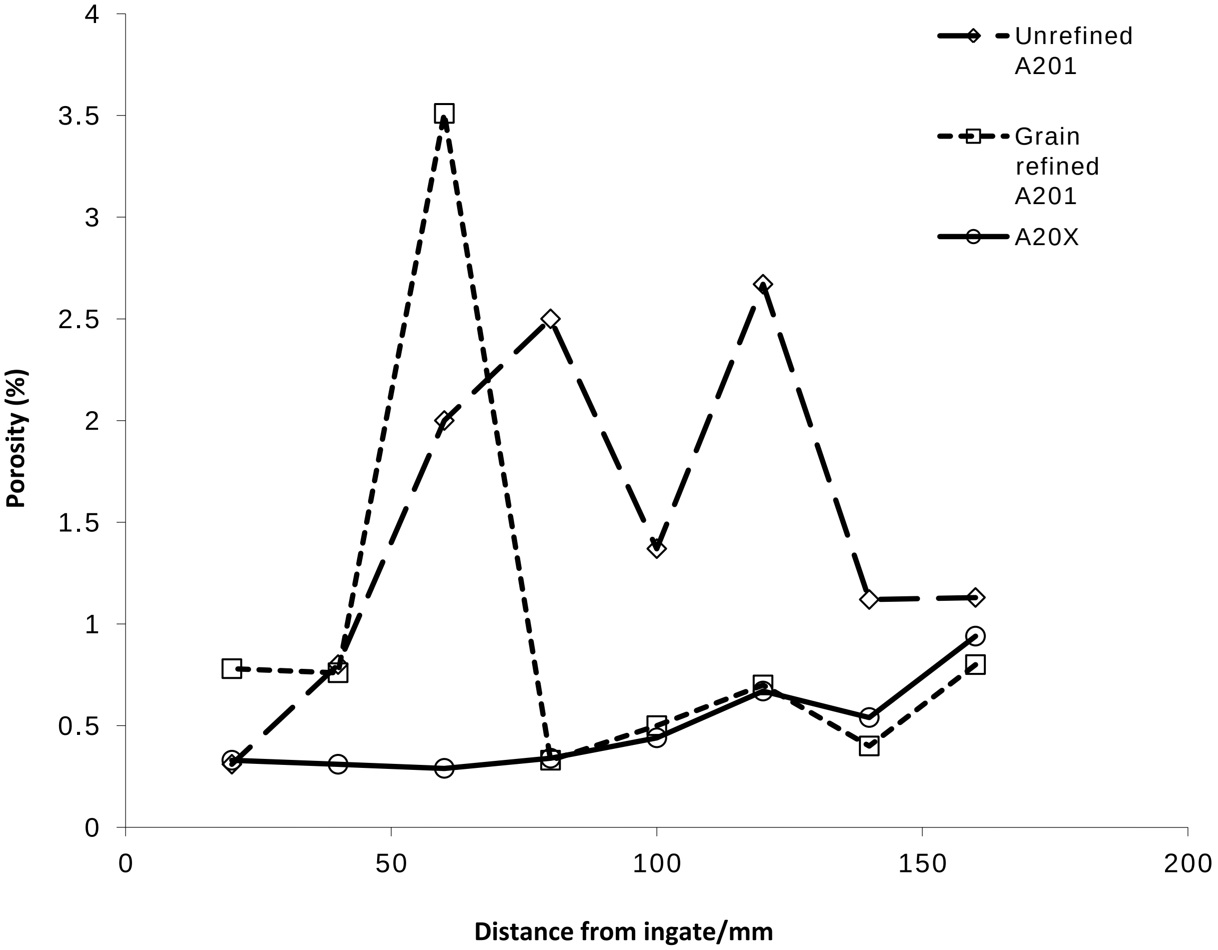

Figure 32: Porosity distribution in eight areas along the centreline of each alloy cast

Figure 32 shows the averaged porosity levels measured in different regions along the centreline of each casting. Table 7 summarises the averaged data. There appears to be a similar trend with regards to the grain refined (GR A201) and A20X alloys with the exception of the high fraction porosity measured at 60mm from the inlet of the GRA201 alloy. The ingot (I) A201 alloy has a higher level of porosity throughout the casting than the other two alloys. The porosity distribution is also more variable, but porosity levels are increased with distance from the ingate. The increased addition of a grain refiner to A201 reduced the levels of measurable porosity in these castings.

With the exception of the sample at 60mm from the ingate in the GR A201 condition, A20X and GR A201 have a very similar pattern of porosity, with levels not increasing above 1% and slowly increasing as distance from the ingate increases.

Table 7: 16 pt averaged porosity data for each of the three alloys when cast and their position and distance from the ingate.

Position in casting	**Distance from ingate (mm)**	**Ingot A201 (%)**	**Grain-Refined A201 (%)**	**A20X (%)**
1	160	1.13	0.80	0.94
2	140	1.12	0.40	0.54
3	120	2.67	0.70	0.67
4	100	1.37	0.50	0.44
5	80	2.50	0.33	0.34
6	60	2.00	3.51	0.29
7	40	0.80	0.76	0.31
8	20	0.31	0.78	0.33
9	40	1.23	0.83	0.62
10	40	0.93	1.55	0.48

5.10 Image Analysis

5.10.1 Microstructure of each alloy (Optical Microscopy)

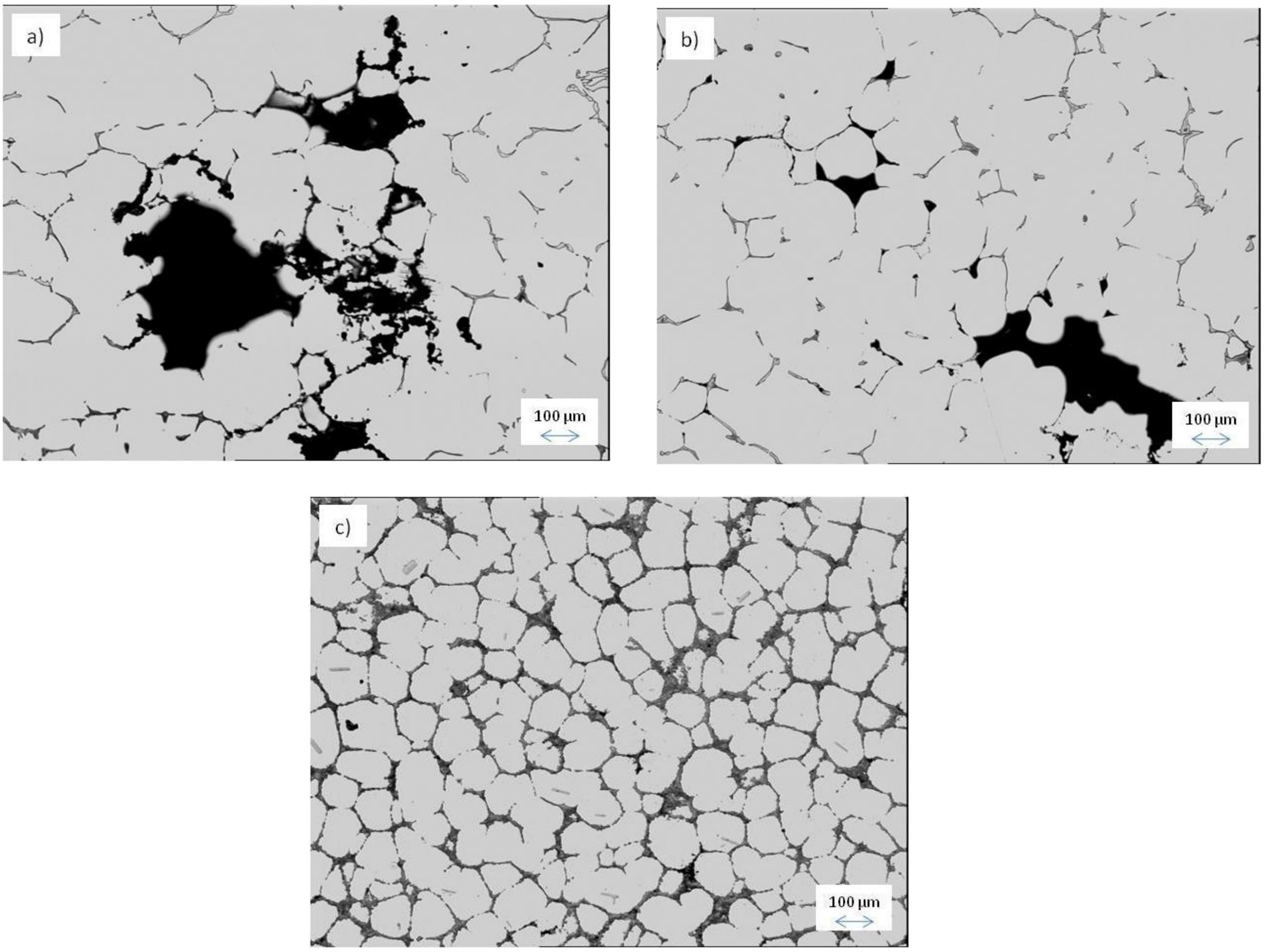

Figure 33: Optical micrograph at 50x magnification of each alloy's microstructure: a) IA201 alloy b) GR A201 and c) A20X. The black areas equate to porosity formation (pores) and the broken network of structures visible are the eutectic $CuAl_2$ phases that have formed last during the solidification process at the grain boundaries.

Figure 33 shows the microstructures of the three alloys 120mm from the bottom of the casting along the centreline. There is a big difference between the A20X alloy and the GRA201 and IA201 alloys. The apparent lack of porosity (black areas) and the more prominent presence of an interconnected (grey areas) network of $CuAl_2$ eutectic phases and TiB_2 particles.

5.10.2 A20X Mechanism of Grain Refinement

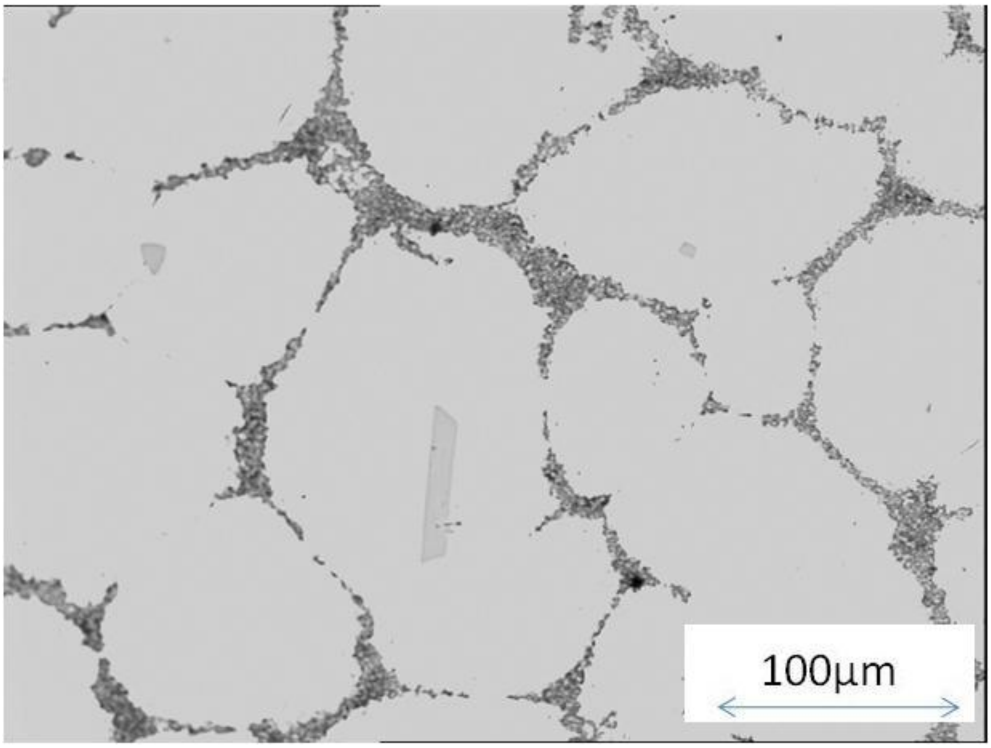

Figure 34: The thin film in the centre of the image is an illustration of where $TiAl_3$ has acted as a nucleation site for the growth of a grain in the A20X microstructure during solidification. This is common throughout the A20X microstructure.

Figure 34 illustrates the role of $TiAl_3$ in the heterogeneous nucleation of the A20X alloy. This micrograph shows a rectangular ‘shard’ of pre-peritectic $TiAl_3$ in the centre of a grain in the microstructure. The effectiveness of this phase as a grain refiner has been confirmed by many authors (Jones and Pearson 1976), (Guzowaski et al 1987) and (Mayers et al 1993) in a reivew of the grain refinement of aluminium alloys by heterogeneous nucleation by (Murty et al 2002).

5.10.3 Microstructure throughout the A20X casting

Figure 35 summarises the effect of local cooling rate within the casting in different locations along the centreline of the casting. The faster the cooling rate the smaller the grains are that develop. As stated in section 5.8, the casting solidifies from the top down which is demonstrated in this figure by the increase in the size the grains as you move down the casting.

Figure 35: The change in microstructure along the centreline of the casting. There is a noticeable difference upon visual observation in the size of the grains as you move towards the bottom due to the internal cooling rate varying along the centreline.

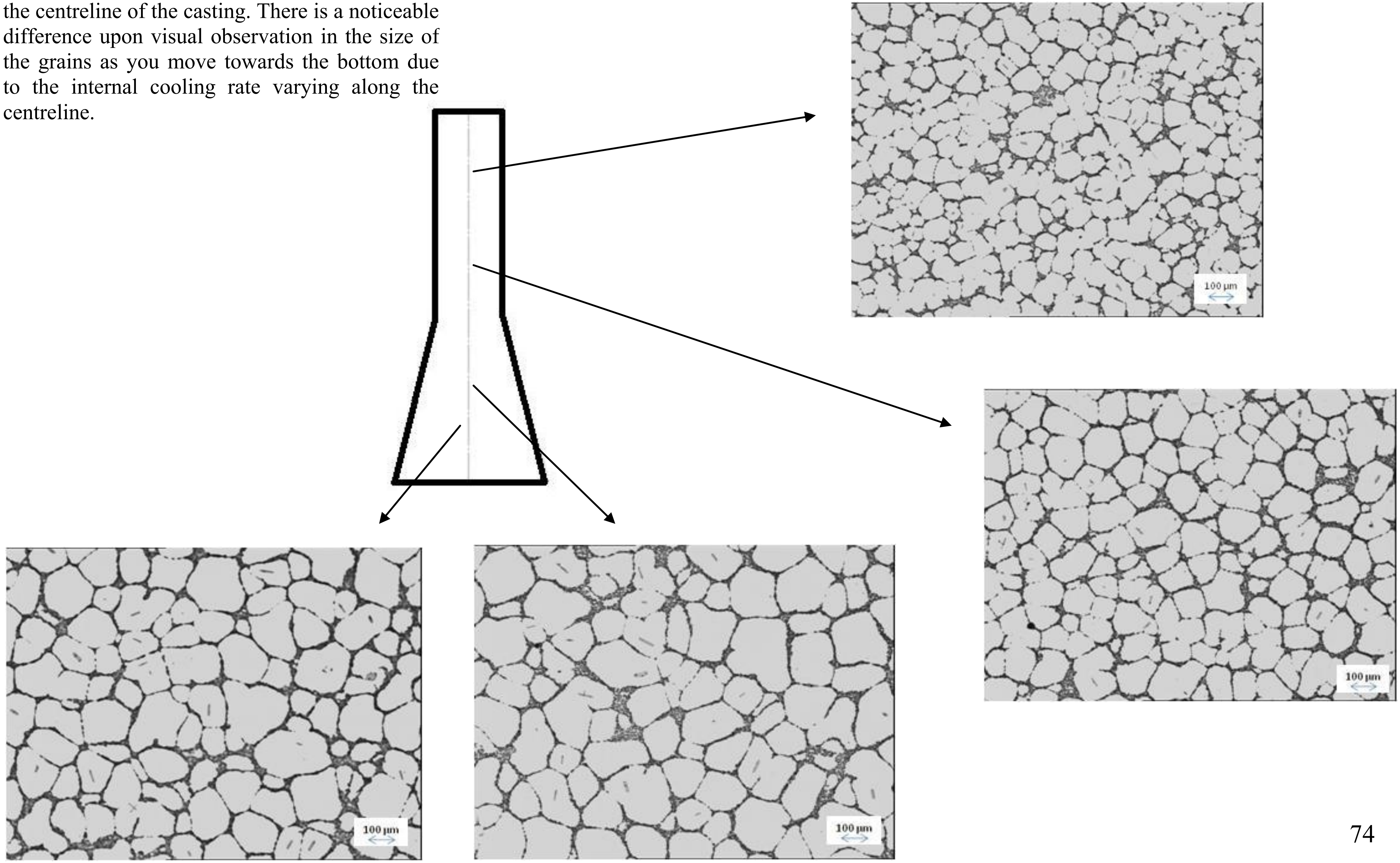

5.10.4.0 Grain Size (Anodizing)

The grain size and morphology of the three alloys was determined to elicit the effects of varying levels of grain refinement. By etching the surface with Floroboric acid the grain boundaries become distinct under polarised light. Figures 36, 37 and 38 show the microstructures of the three alloys at 60 and 120 mm from the bottom of the casting along the centreline. Table 8 shows the grain sizes of the three alloys at the respective locations in the casting. The two locations provide a representative measure of the grain size in the casting. The grain size was calculated using a standard linear intercept method (10 times) to get an accurate representation of the mean grain size from each location.

Table 8: The grain size of each of the three alloys at two locations: 60mm and 120mm along the centreline of the castings

Distance from the ingate (mm)	**Grain Size (µm)**		
	A20X	**GRA201**	**IA201**
60	98.59	167.26	165.61
120	76.80	116.08	124.446

From figures 36, 37 and 38 it is clear that solidification time has an effect on the grain size and morphology. The images taken at 60mm from the ingate in all three alloys show a much coarser, larger grain on average compared with the 120mm condition because that part of the casting has taken longer to freeze. Comparing the alloys themselves; there is a transition in microstructure and size from a globular, more uniform size of grains in the A20X alloy to an increasingly cellular, rosette-like grain structure seen in the GRA201 and IA201 alloys. This marks the transitional link between degrees of grain refinement and the resulting transition from a dendrite to cellular to globular grain structure.

- **A20X**

a)

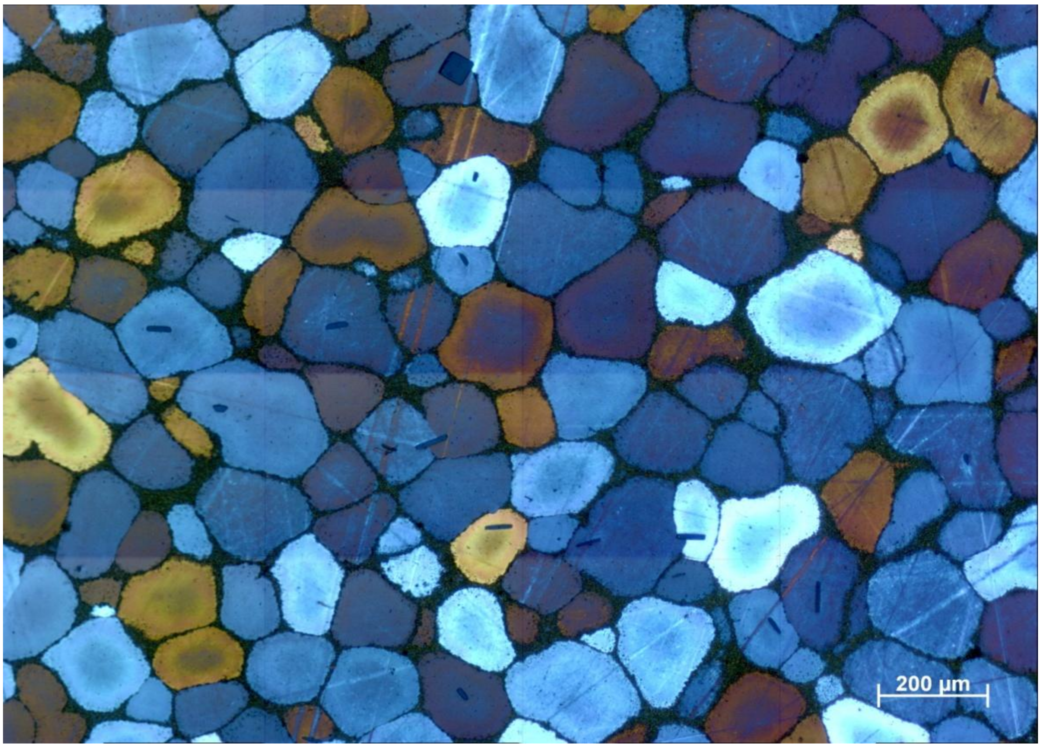

b)

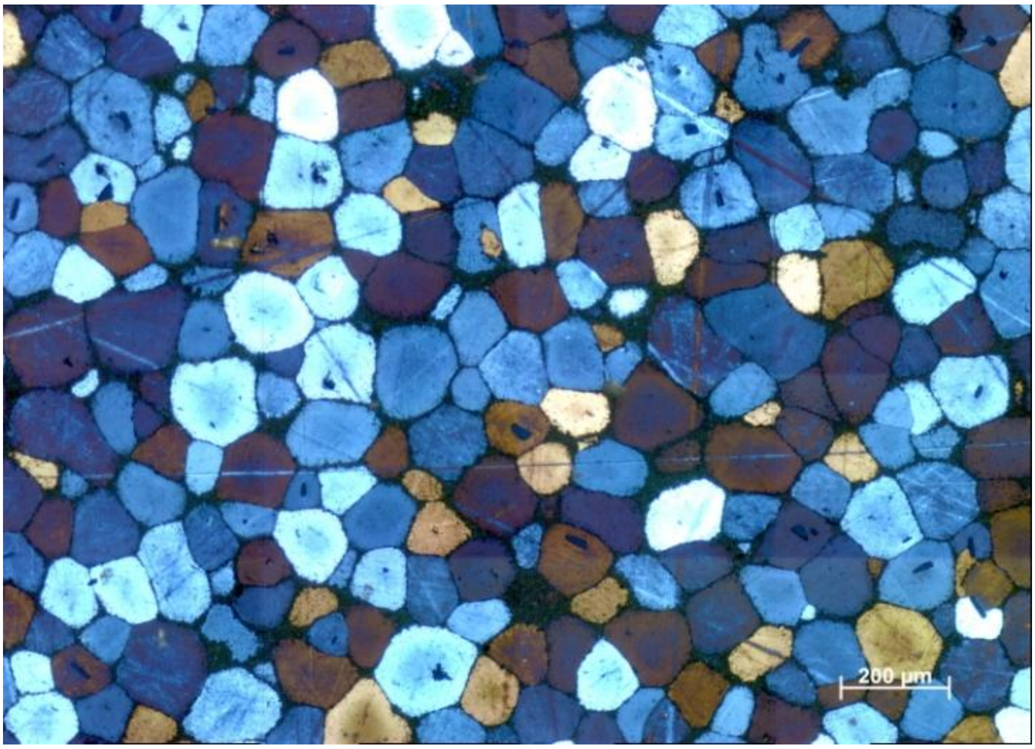

Figure 36: Micrographs of A20X casting at different points along the centreline. a) 60mm from the ingate b) 120mm from the ingate (anodised using 2% HBF_4 and viewed in polarized light).

- **GR A201**

a)

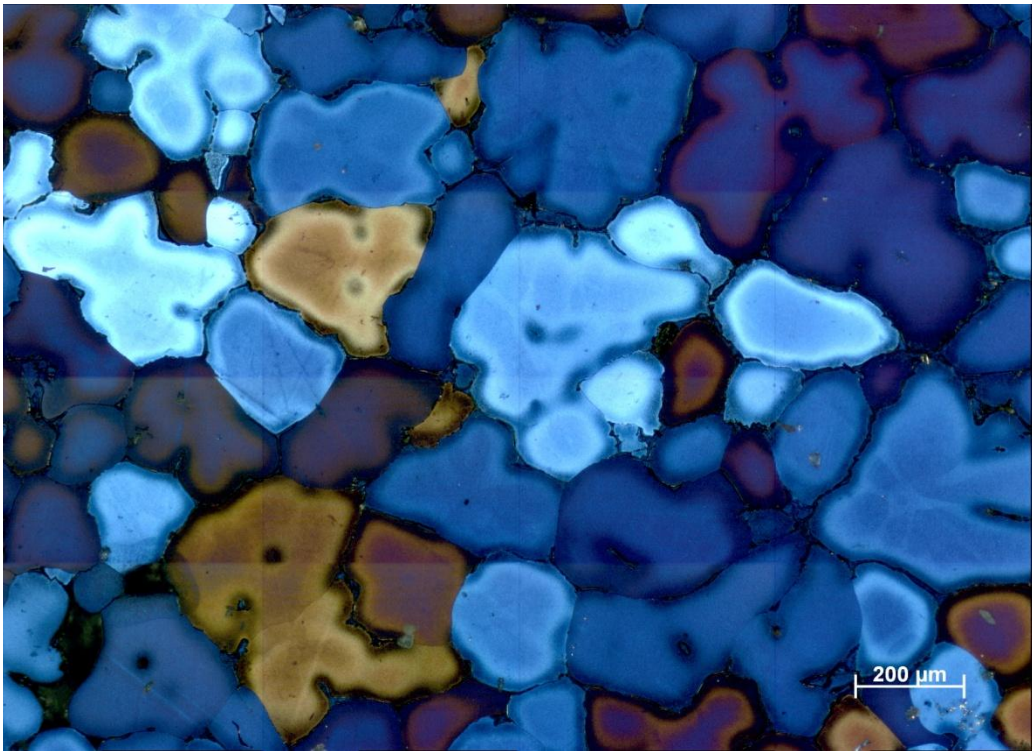

b)

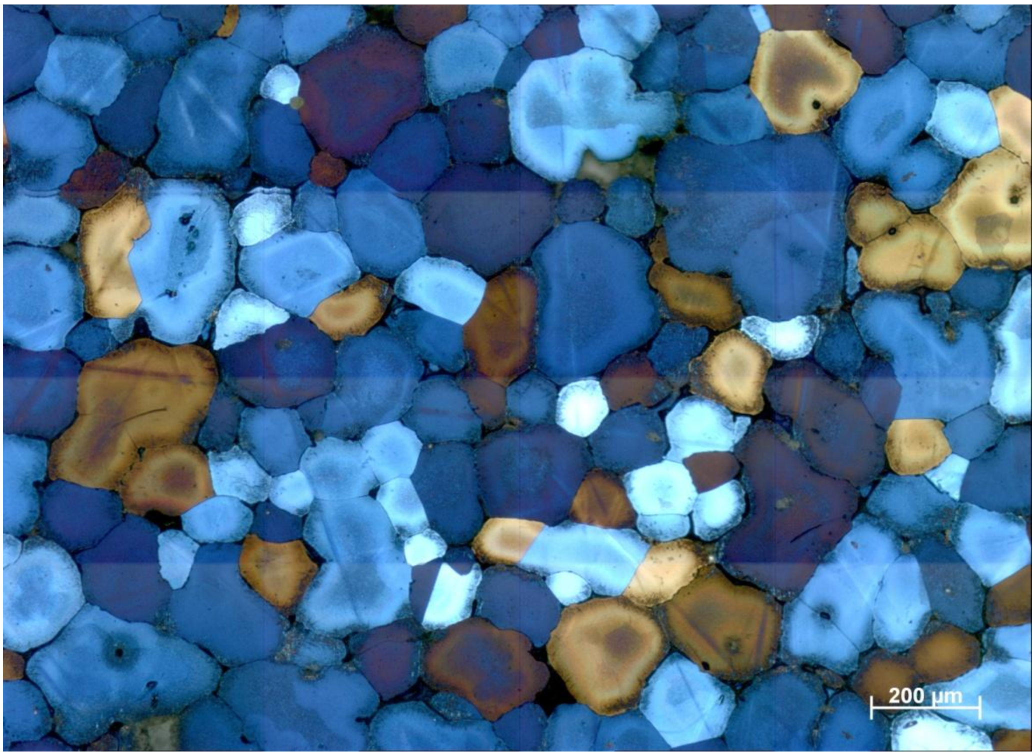

Figure 37: Micrographs of GRA201 casting at different points along the centreline. a) 60mm from the ingate b) 120mm from the ingate (Anodized using 2% HBF_4 and viewed using polarised light).

- **IA201**

a)

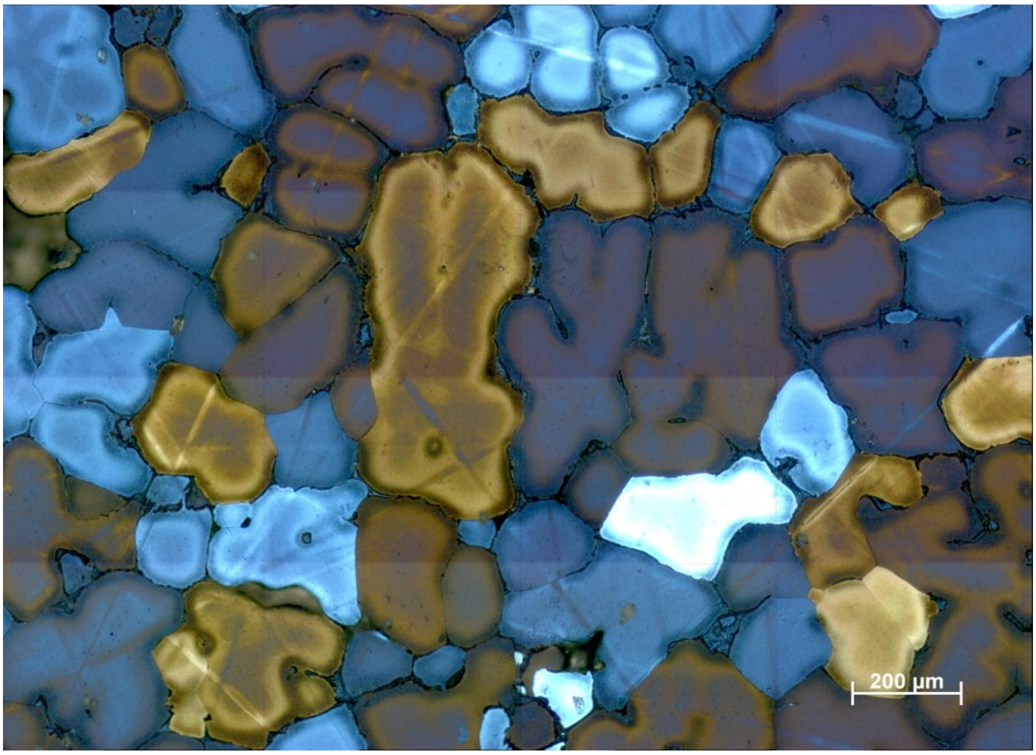

b)

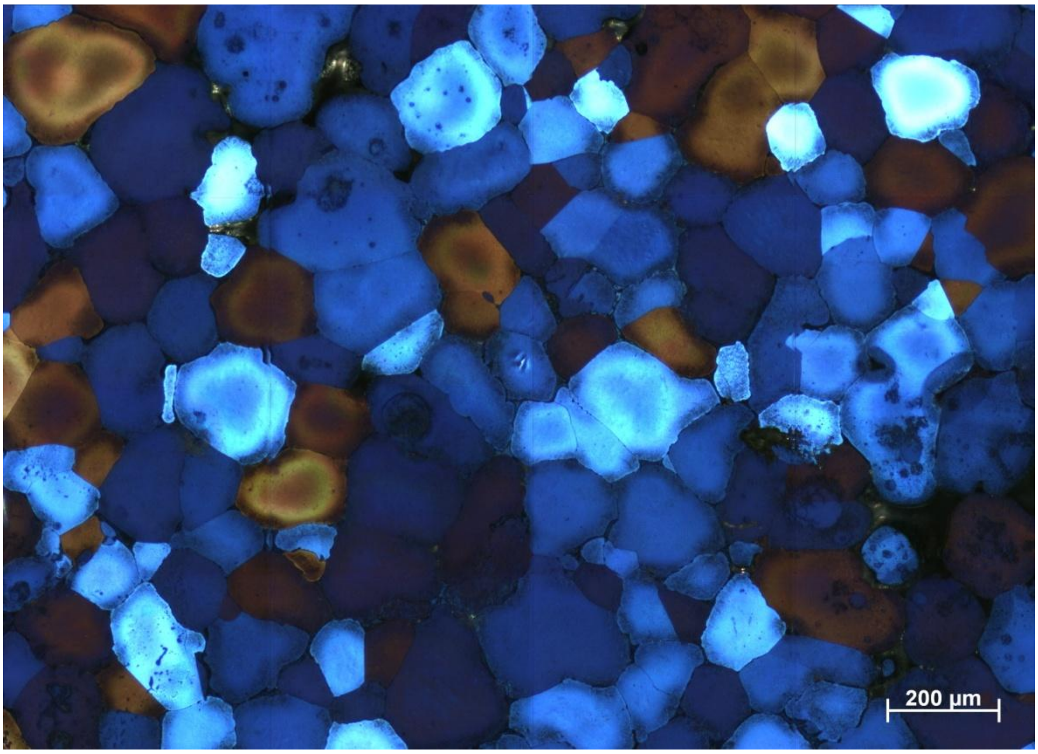

Figure 38: Micrographs of IA201 casting at different points along the centreline. a) 60mm from the ingate b) 120mm from the ingate (Anodized using 2% HBF_4 and viewed using polarized light).

5.11 Feeding Effects in the casting. (Top of the casting)

Figure 39 shows plan views of the tops of the castings of each alloy. Each of the castings shows large amounts of ‘sinking’ associated with liquid and mass feeding with substantial differences. IA201 (Figure 39a) exhibits the least sinking of the three alloys. The corners of the casting were rendered immobile during the early stages of solidification whereas the GRA201 and A20X castings (figures 39b) and 39c) with increasing amounts of grain refiner exhibited progressively larger sinks as a result due to improved feeding. The A20X casting has surface folding indicating a high level of liquid and mass motion during solidification.

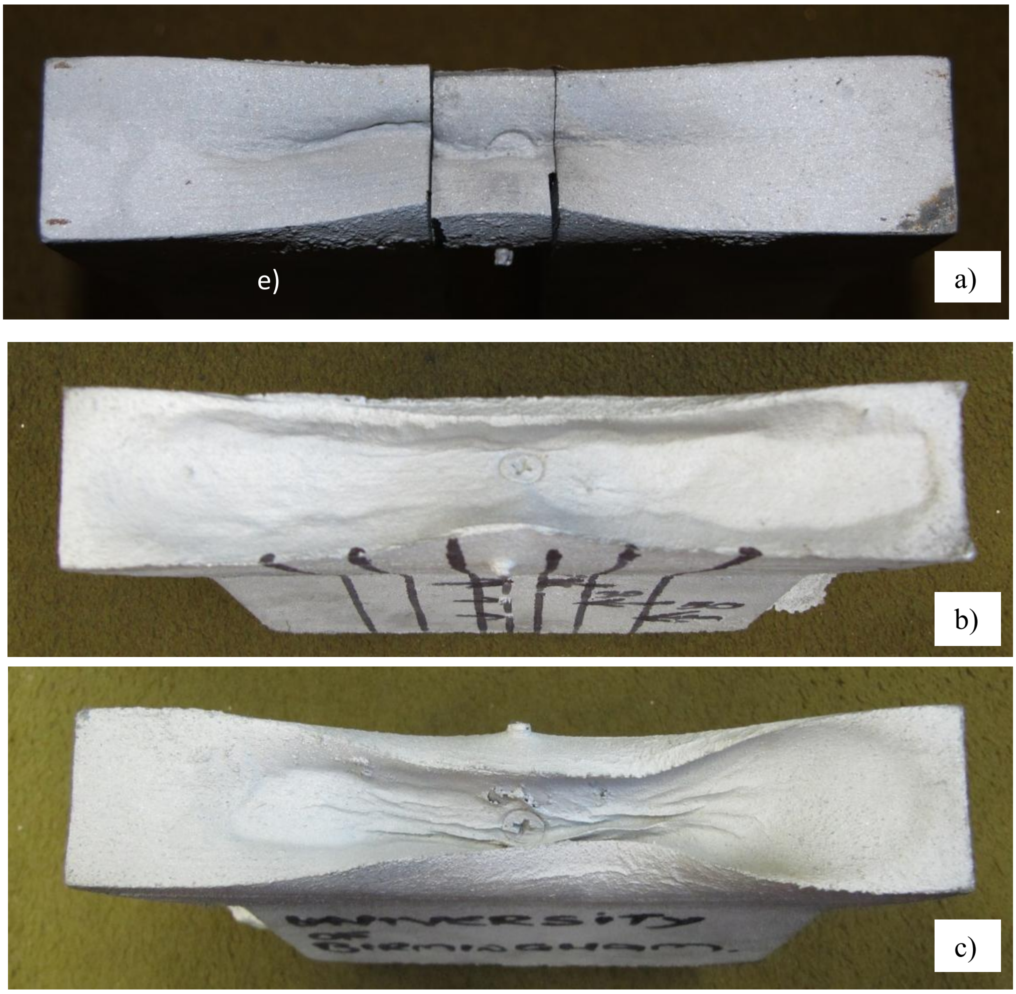

Figure 39: Plan views of the top surfaces of castings illustrating the effects of grain refinement on the feeding characteristics of each alloy. The top of the each casting has differing ‘sinks’ which can be linked to feeding. a) IA201, b) GRA20X1 c) A20X.

5.12 MAGMASOFT Model Calibration

MAGMASOFT modelling software has many adjustable parameters both in terms of material and process that facilitate accurate process simulation. Figures 40 to 48 report the measured and calculated data entered into MAGMASOFT to generate an A20X user material property database. Unless reported previously or below, data included has been generated in the project. These material parameters are the basis upon which all reported results were obtained. The original Al-4%Cu MAGMASOFT material database is reported in Appendix 1.

5.12.1 General Parameters

Data for surface tension coefficient was taken from MAGMASOFT Al-4%Cu database.

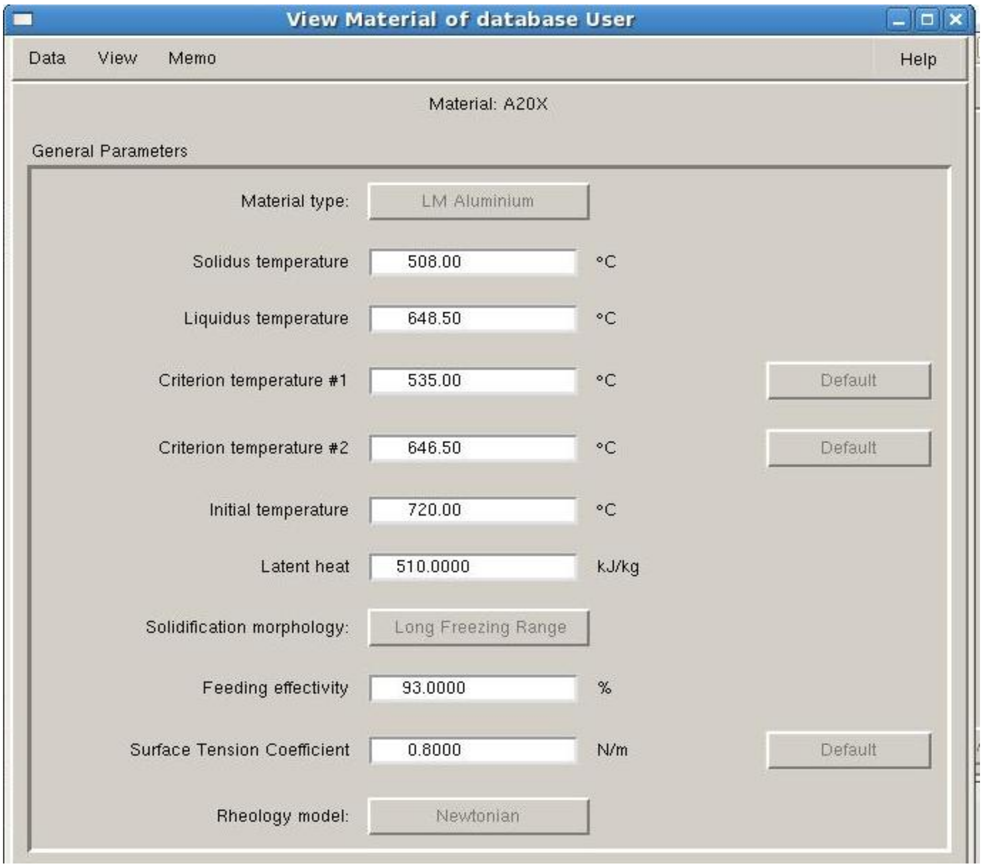

Material: A20X

General Parameters

Material type: LM Aluminium

Solidus temperature 508.00 °C

Liquidus temperature 648.50 °C

Criterion temperature #1 535.00 °C

Criterion temperature #2 646.50 °C

Initial temperature 720.00 °C

Latent heat 510.0000 kJ/kg

Solidification morphology: Long Freezing Range

Feeding effectivity 93.0000 %

Surface Tension Coefficient 0.8000 N/m

Rheology model: Newtonian

Figure 40: General parameters for the A20X alloy that were imported into the model, of which latent heat and the temperature parameters were calculated from the differential scanning calorimetry results of A20X

5.12.2 Thermal Conductivity

Data taken from MAGMASOFT Al-4%Cu database

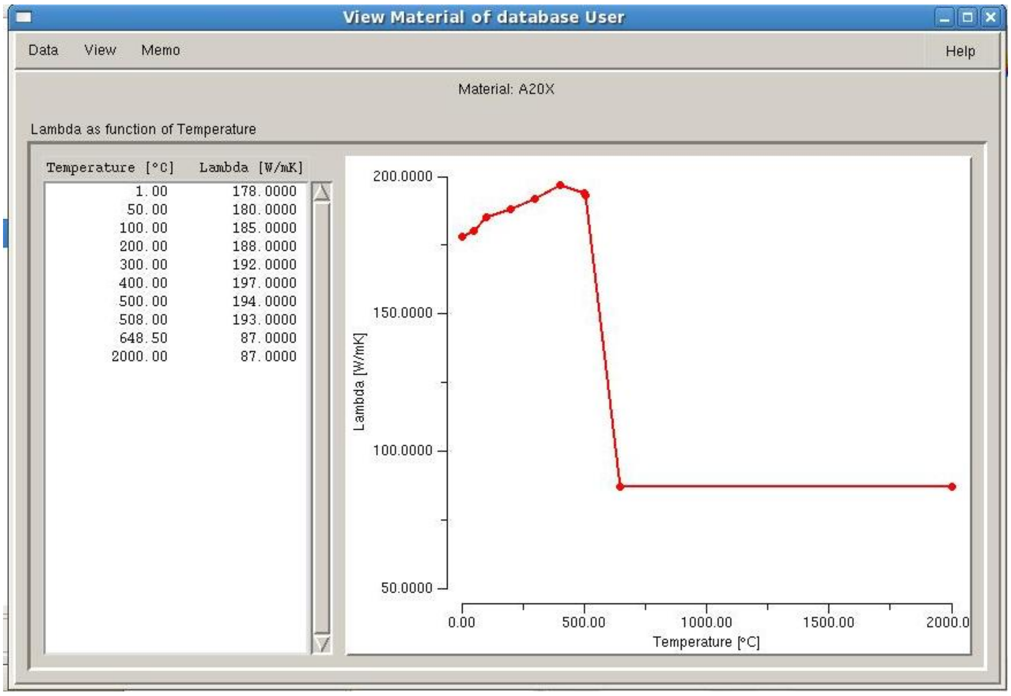

Material: A20X

Lambda as function of Temperature

Temperature [°C]	Lambda [W/mK]
1.00	178.0000
50.00	180.0000
100.00	185.0000
200.00	188.0000
300.00	192.0000
400.00	197.0000
500.00	194.0000
508.00	193.0000
648.50	87.0000
2000.00	87.0000

Figure 41: Thermal conductivity plotted as a function of temperature

5.12.3 Fraction Solid

Figure 22 shows the fraction of solid data acquired from the thermal analysis experiment of all three alloys (section 5.2). A series of data points were selected to sufficiently represent the fraction of solid curve (figure 26) and inputted into the material property database (figure 42).

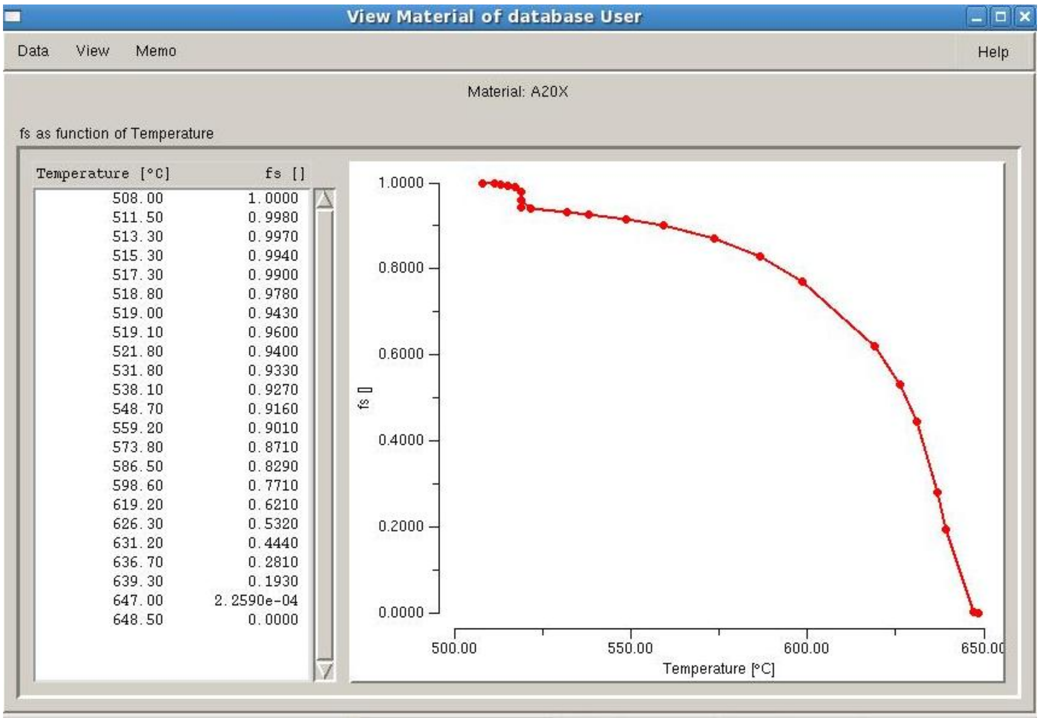

Material: A20X

fs as function of Temperature

Temperature [°C]	fs []
508.00	1.0000
511.50	0.9980
513.30	0.9970
515.30	0.9940
517.30	0.9900
518.80	0.9780
519.00	0.9430
519.10	0.9600
521.80	0.9400
531.80	0.9330
538.10	0.9270
548.70	0.9160
559.20	0.9010
573.80	0.8710
586.50	0.8290
598.60	0.7710
619.20	0.6210
626.30	0.5320
631.20	0.4440
636.70	0.2810
639.30	0.1930
647.00	2.2590e-04
648.50	0.0000

Figure 42: Fraction solid curve of A20X

5.12.4 Specific Heat Capacity (C_p)

The specific heat capacity of A20X was calculated both on heating and cooling using the DSC. Figure 43 shows the C_p on heating of A20X. Due to a fault on the DSC machine, the measurement of stable C_p data for cooling and solidification was not possible (figure 44). Data was corrected based on the heating data (figure 43) to obtain a normalised baseline curve for C_p (figure 45).

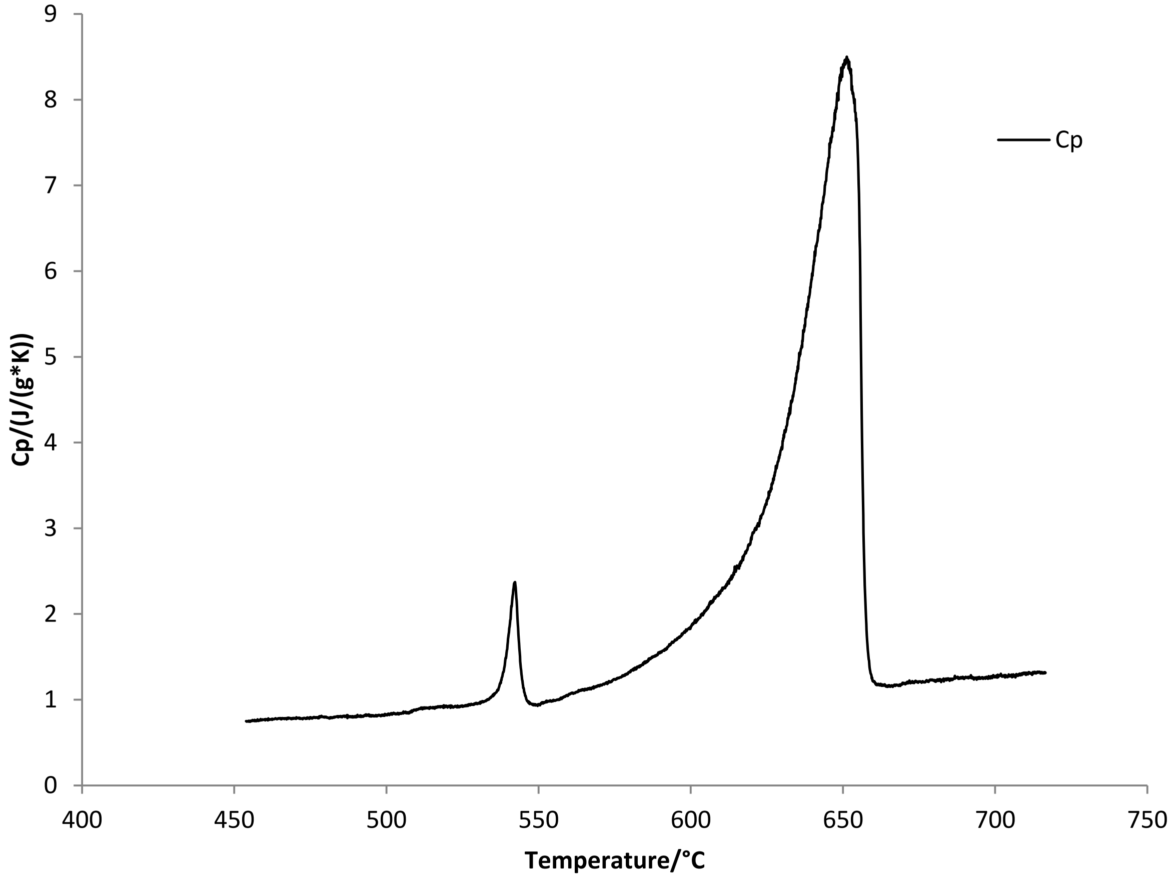

Figure 43: Specific Heat Capacity data from A20X alloy on heating. (450°C - 720°C at 3°C/min)

The A20X data exhibits two distinct peaks; the first high temperature peak represents the melting (heating) or solidification (cooling) of the primary aluminium phase and the second smaller peak is associated with the eutectic phases. The temperature boundaries (450°C and 720°C) used in the experiment encapsulates the solidification range for an Al-Cu based alloy. However due to restrictions with the instrument, could not be widened further down to room temperature.

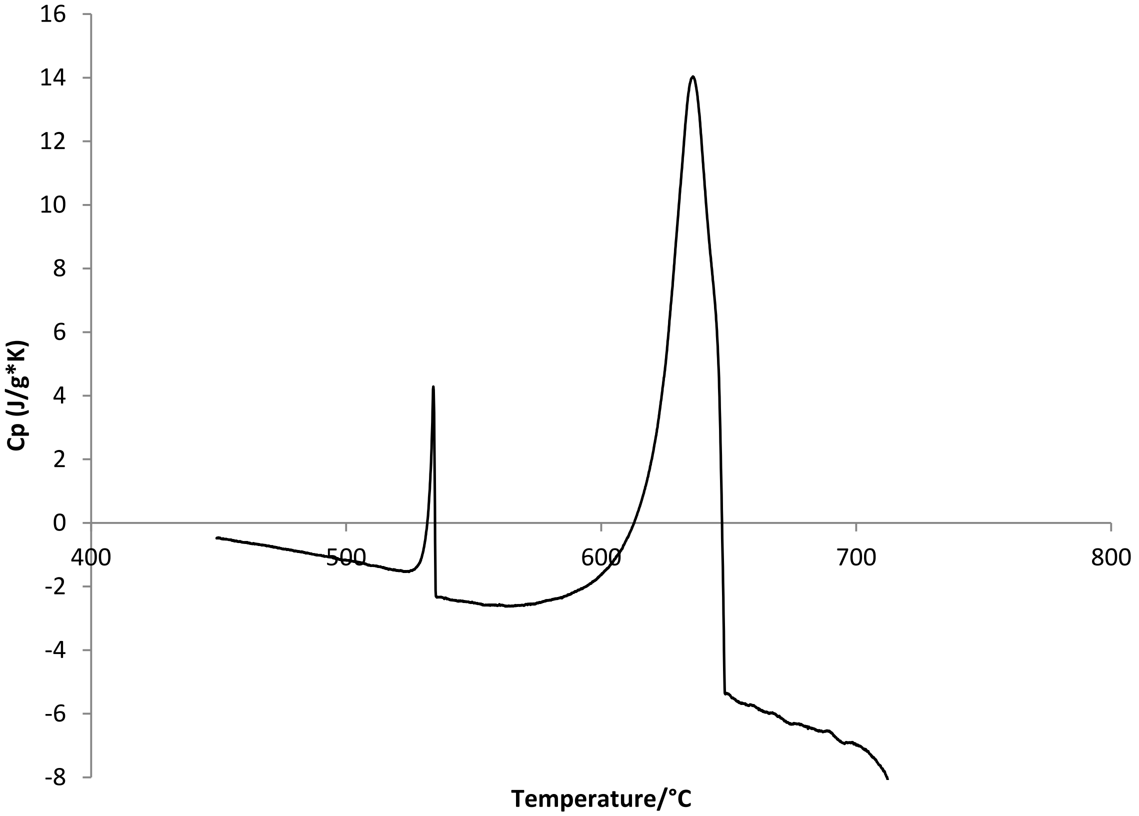

Figure 45: Apparent Specific Heat Capacity data for the A20X alloy on cooling. (720°C – 450°C at 3°C/min)

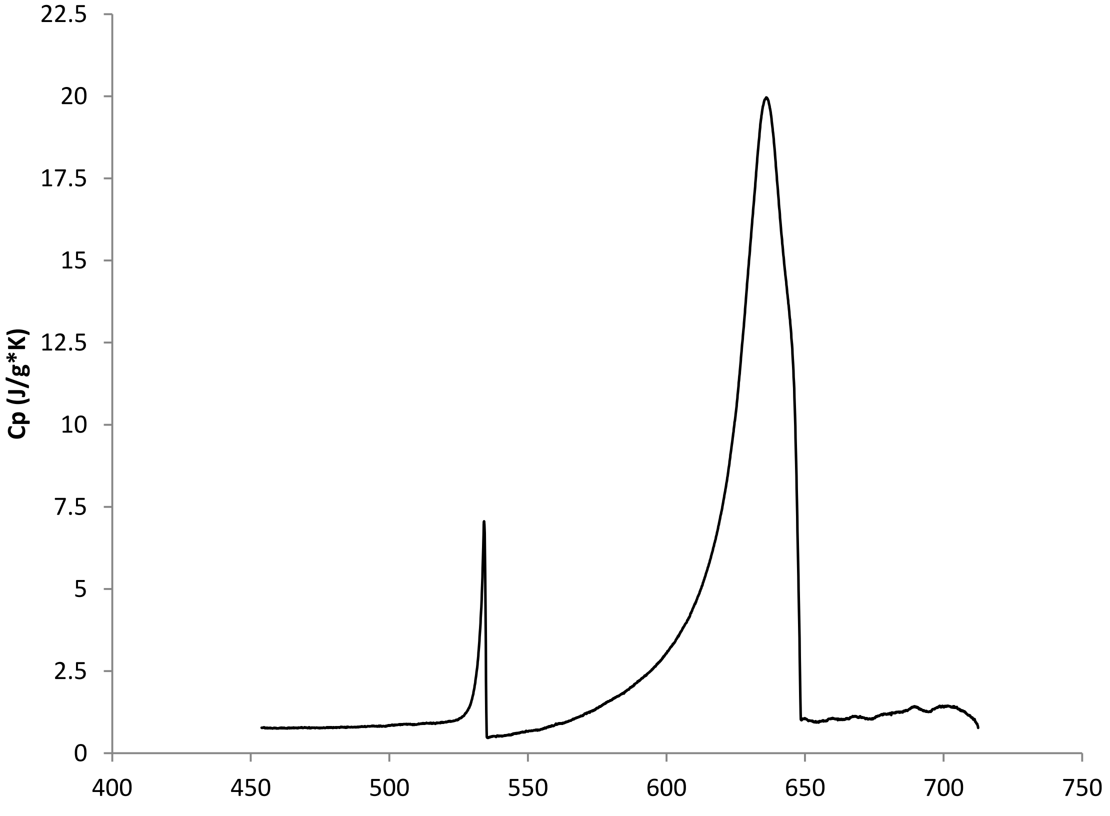

Figure 44: Corrected apparent Specific Heat capacity values on cooling of A20X including transformations (peaks).

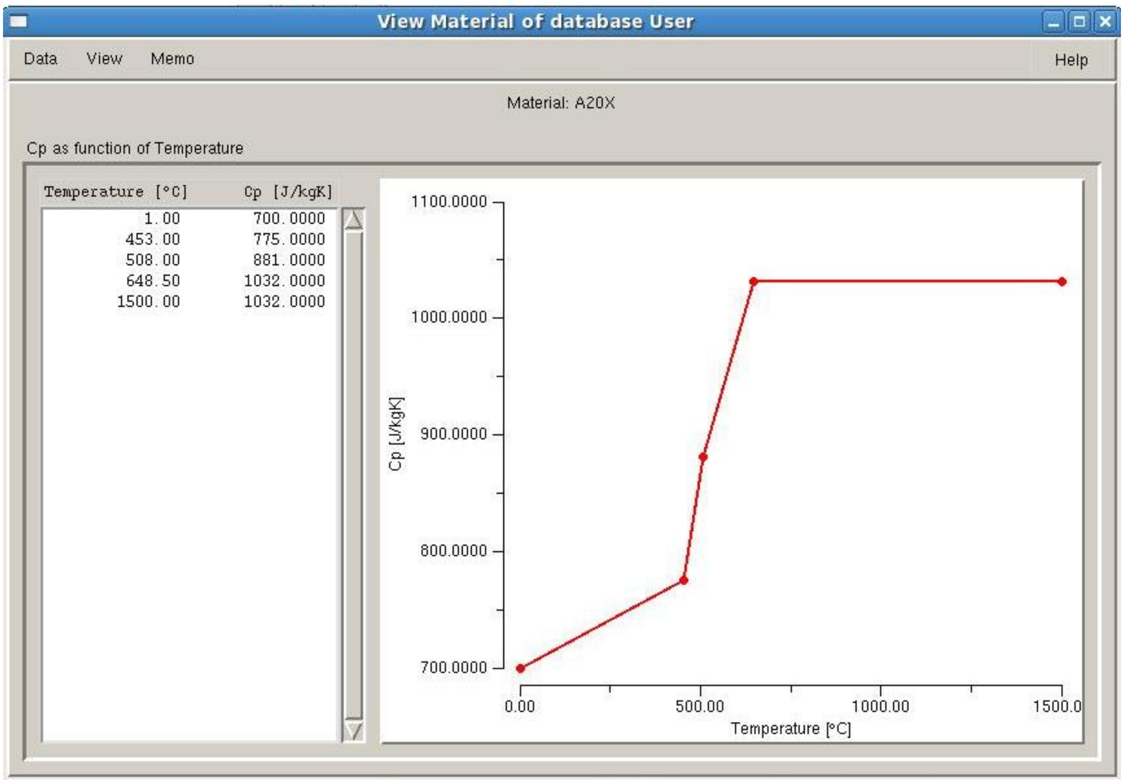

Material: A20X

Temperature [°C]	Cp [J/kgK]
1.00	700.0000
453.00	775.0000
508.00	881.0000
648.50	1032.0000
1500.00	1032.0000

Figure 46: Specific heat capacity data of A20X alloy entered into MAGMASOFT database

By taking C_p at the temperature at which the DSC just started recording (453°C), at the start of the solidus transformation (508°C) and the end of the liquidus transformation (648.5°C) and by assuming that the C_p remains constant after the liquidus temperature is reached (an assumption made by MAGMASOFT themselves with all other aluminium alloys) the actual C_p curve was determined.

Due to unavoidable flaws in the measured C_p data it was necessary to calculate the latent heat, L, of melting using the following approach. L was obtained by subtracting the baseline specific heat at temperature T from the measured specific heat obtained from the corrected DSC cooling trace using the assumption that fs and C_p varied linearly with T. However, it can be seen in Figure 45 that C_p at the start and end of the primary and eutectic transformations is significantly different. This was accounted for using the expressions:

Primary Phase: —— (5.6)

Eutectic Phase: —— (5.7)

$C_{p(l)}$ = C_p at liquidus

$C_{p(e)}$ = C_p at the start of the eutectic transformation

T = instantaneous temperature

T_e = eutectic temperature

T_l = temperature of the liquid

T_s = temperature of the solid

The latent heat, *L*, was then calculated by step-wise integration of the difference between measured (DSC) and baseline C_p according to the expression:

(5.8)

T_L = temperature of the liquid

T_S = temperature of the solid

dt = time step

5.12.2.5 Density: (Rho*)

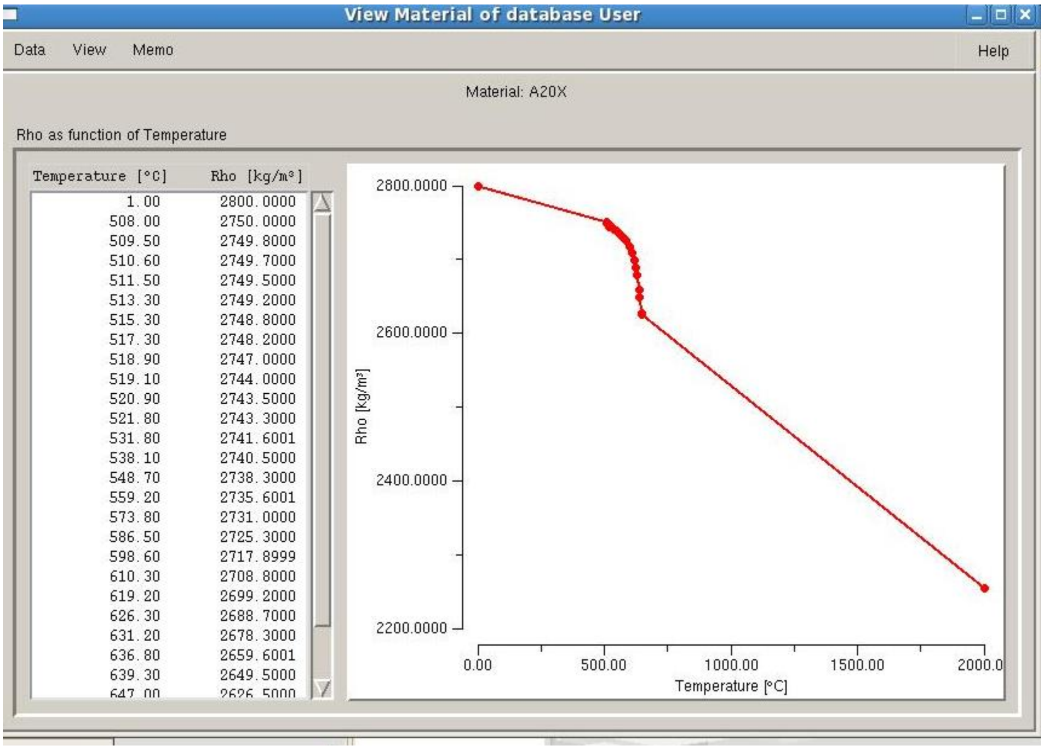

Temperature [°C]	Rho [kg/m³]
1.00	2800.0000
508.00	2750.0000
509.50	2749.8000
510.60	2749.7000
511.50	2749.5000
513.30	2749.2000
515.30	2748.8000
517.30	2748.2000
518.90	2747.0000
519.10	2744.0000
520.90	2743.5000
521.80	2743.3000
531.80	2741.6001
538.10	2740.5000
548.70	2738.3000
559.20	2735.6001
573.80	2731.0000
586.50	2725.3000
598.60	2717.8999
610.30	2708.8000
619.20	2699.2000
626.30	2688.7000
631.20	2678.3000
636.80	2659.6001
639.30	2649.5000
647.00	2626.5000

Figure 47: Density: Rho* plotted as a function of temperature.

5.12.2.6 Density Specific Heat Capacity

The density of the liquid and solid phases was calculated using data for Al-4%Cu and the solid and liquid data extrapolated into the semi-solid region. The density was calculated according to the expression:

(5.9)

Using the fraction solid data reported in Figure 42 and where:

$P_{(T)}$ = Density at temperature T

$P_{s(T)}$ = Density of solid at temperature T

$P_{L(T)}$ = Density of liquid at temperature T

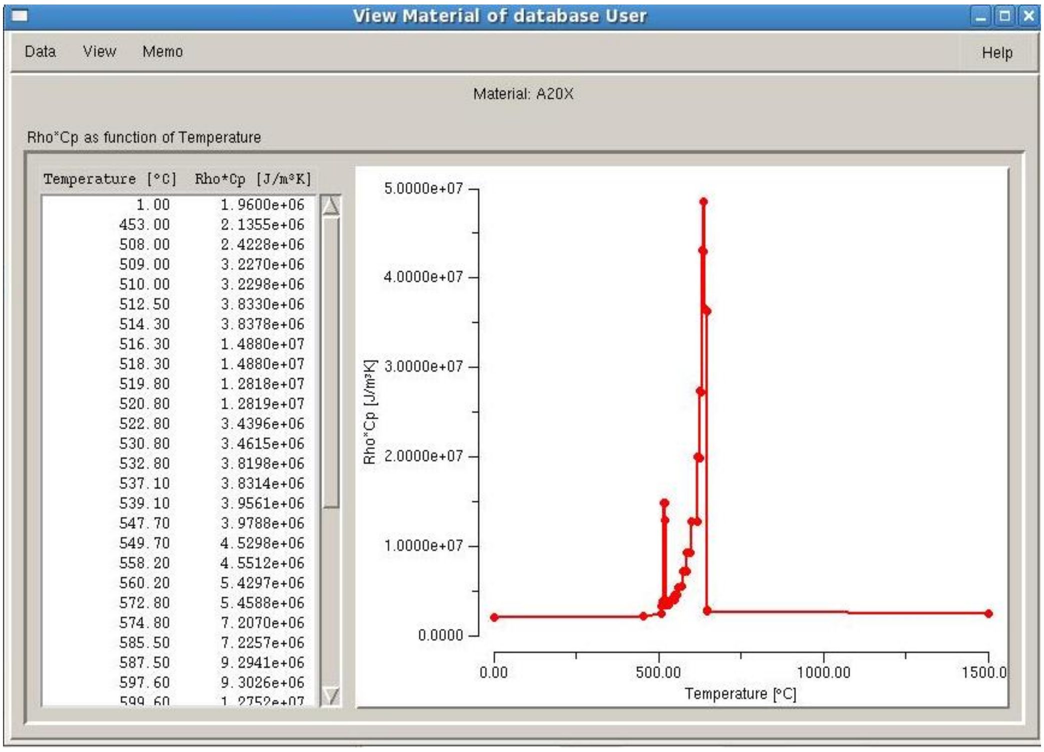

Material: A20X

Rho*Cp as function of Temperature

Temperature [°C]	Rho*Cp [J/m³K]
1.00	1.9600e+06
453.00	2.1355e+06
508.00	2.4228e+06
509.00	3.2270e+06
510.00	3.2298e+06
512.50	3.8330e+06
514.30	3.8378e+06
516.30	1.4880e+07
518.30	1.4880e+07
519.80	1.2818e+07
520.80	1.2819e+07
522.80	3.4396e+06
530.80	3.4615e+06
532.80	3.8198e+06
537.10	3.8314e+06
539.10	3.9561e+06
547.70	3.9788e+06
549.70	4.5298e+06
558.20	4.5512e+06
560.20	5.4297e+06
572.80	5.4588e+06
574.80	7.2070e+06
585.50	7.2257e+06
587.50	9.2941e+06
597.60	9.3026e+06
599.60	1.2752e+07

Figure 48: Rho Cp plotted as a function of temperature.

5.13 MAGMASOFT Simulation Results

5.13.1 Emeshment Sensitivity Study

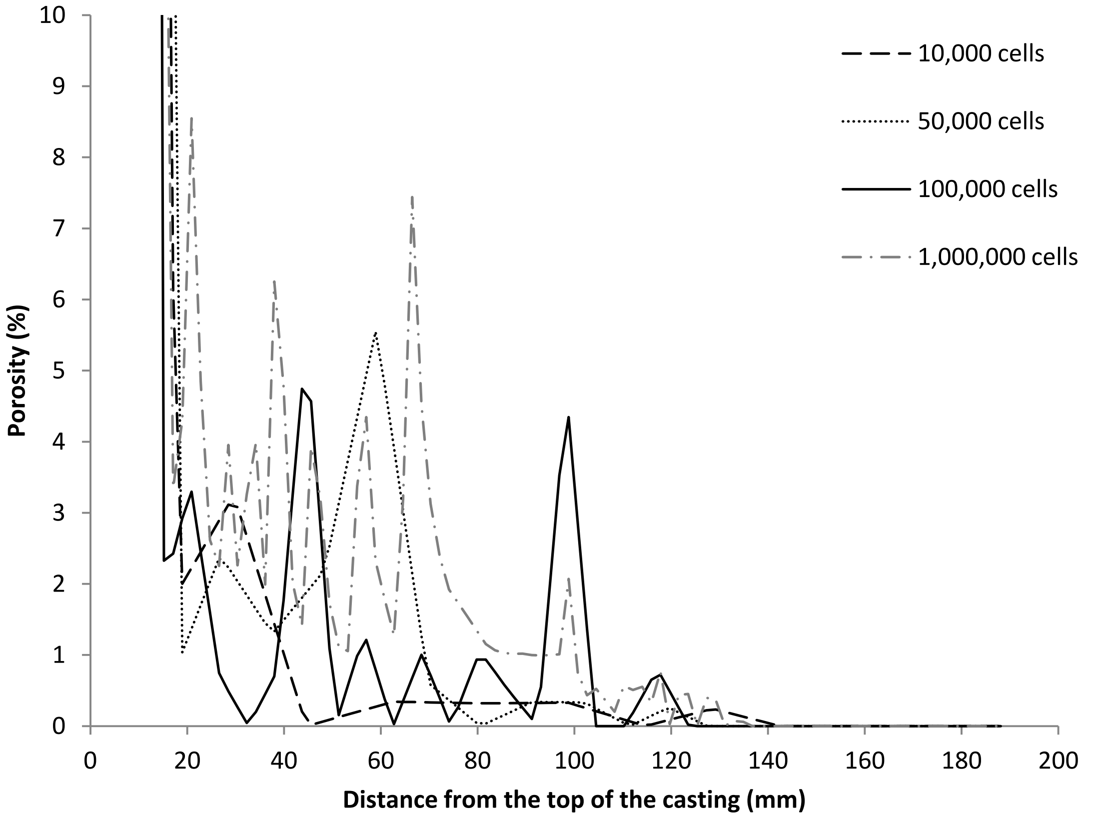

Figure 49: MAGMASOFT porosity distribution along the centreline of an A20X simulation casting with varying mesh densities (feeding effectiveness was 93%). The finer the mesh the more resolvable the porosity distribution becomes.

1D profiles of centreline porosity were created from the MAGMASOFT model for the A20X castings. The variation in porosity seen when the mesh size alone is changed within the model is significant. There is a difference in both position of the porosity peaks and the total amount of porosity predicted. However the greater variability from position to position in the 1,000,000 cell condition is unusual. The general trend observed is that for all meshes the porosity increases with distance from the ingate. 100,000 cell meshes were used for all further analysis as it was a compromise between simulation time, which was over three days for 1,000,000 mesh elements and improved accuracy in the model. Discussion with MAGMASOFT (MAGMASOFT, 2011) that for this geometry a 100,000 cell mesh was sufficient.

5.13.2 Porosity Distribution of A20X from Calibrated Model

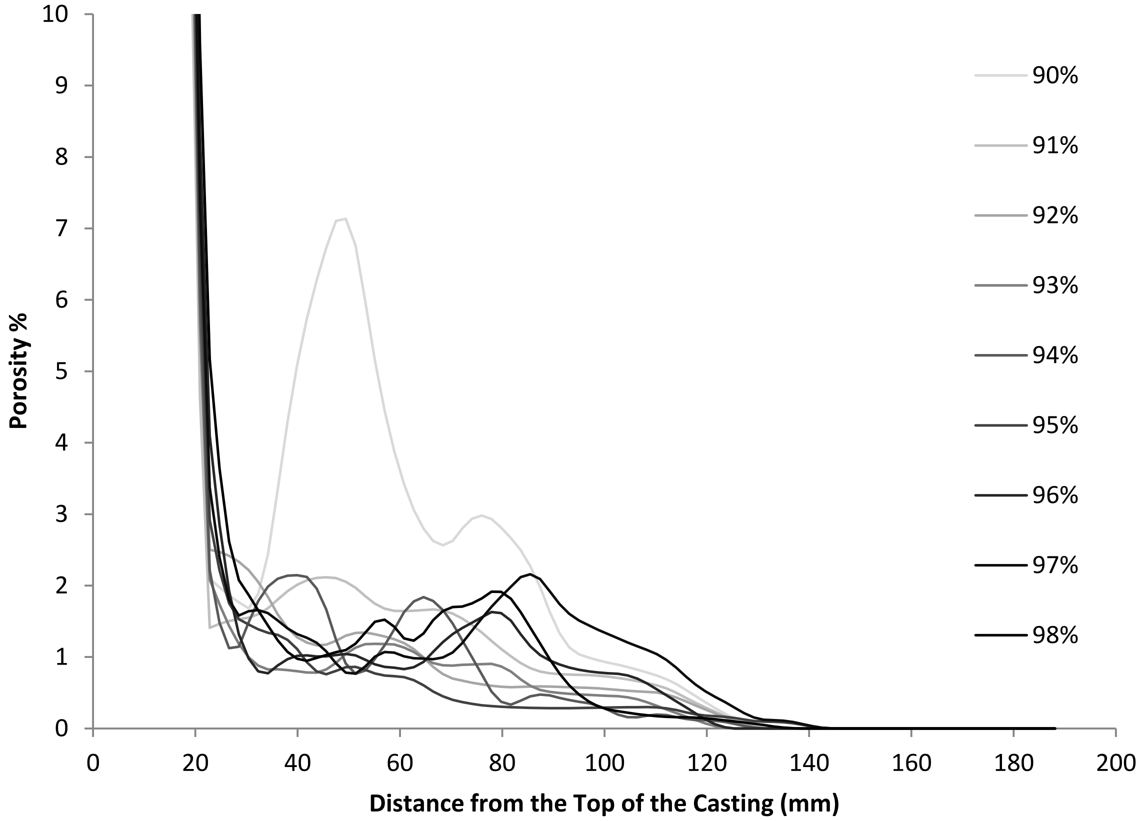

Figure 50: Predicted centreline porosity distribution (100pts) of A20X at different % feeding effectiveness (100,000 element mesh).

Figure 50 shows the predicted distribution of porosity using a 100,000 element mesh for the A20X alloy as a function of feeding effectiveness. The amount of predicted porosity decreased with increasing feeding effectiveness (FE). Interestingly, however, at 98% FE the total average porosity formed is greater than that obtained when at 92, 93, 94, 95 and 96% FE.

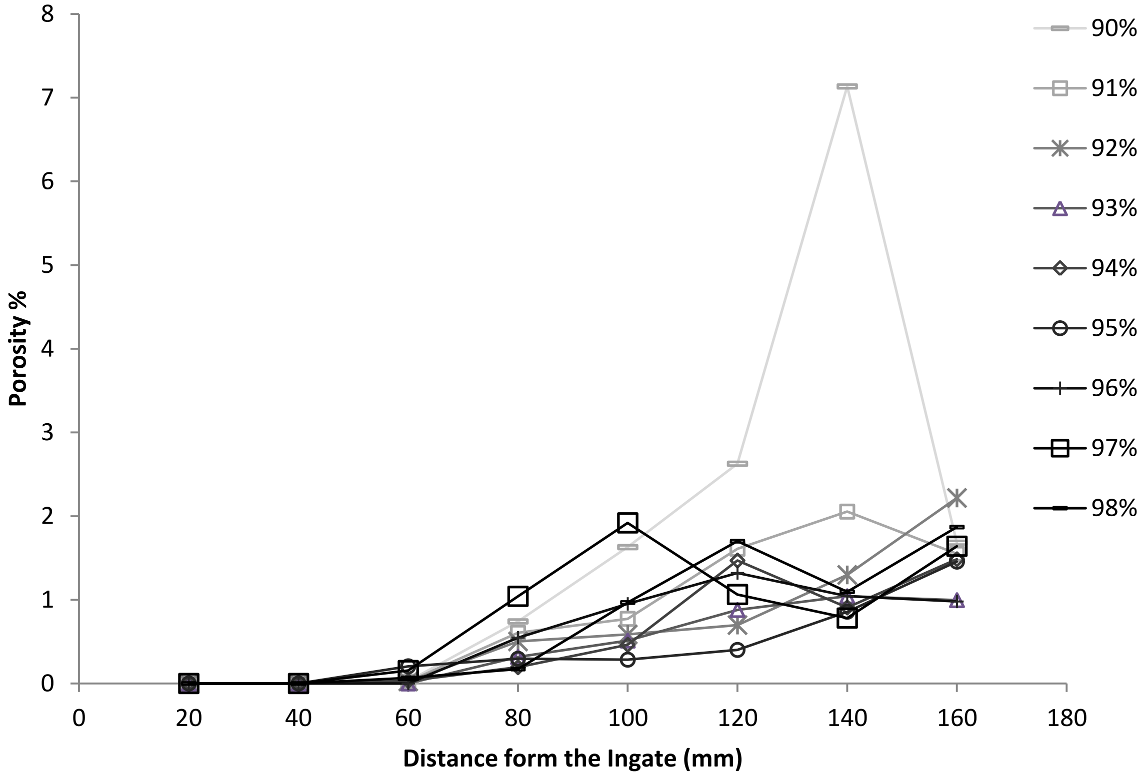

Figure 51: Distribution of porosity at eight points along the centreline of the A20X model casting for a range of feeding effectiveness values. Measurements were taken at 20, 40, 60, 80, 100, 120, 140, 160mm from the bottom of the casting.

Figure 51 is a localised plot of figure 50, plotting only the eight point locations measured in the real casting to compare better the level the porosity distribution. As the distance from the ingate increases, the porosity levels increases. The average porosity level for the real A20X casting was 0.482% and the model condition of feeding effectiveness that is closest to that is at 93% where the average porosity level was 0.467%.

Figure 52 shows the predicted centreline porosity for the MAGMASOFT's Al-4%Cu alloy for feeding effectiveness values between 90-98%. It illustrates an increase in the predicted porosity over the same FE range as the A20X alloy up until the 97 and 98% FE which appears to predict less porosity than the A20X model.

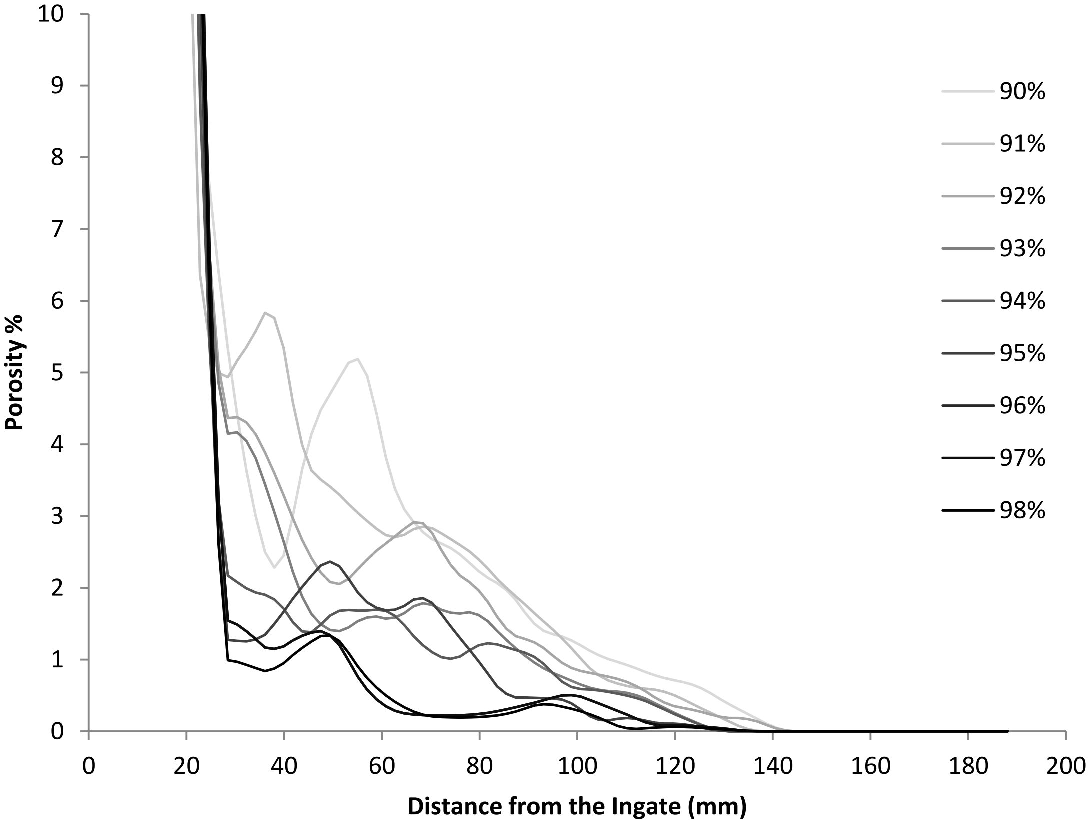

Figure 52: Predicted centreline porosity distribution (100pts) of MAGMASOFT's Al-4%Cu alloy at different % feeding effectiveness values (100,000 mesh model).

Figure 53 shows the predicted porosity of the Al-4%Cu alloy at points at which metallographic measurements were made. It predicts a sharper increase in porosity levels as you move up the casting and ultimately higher levels of porosity at the top of the casting in all FE conditions compared with the A20X model (figure 51).

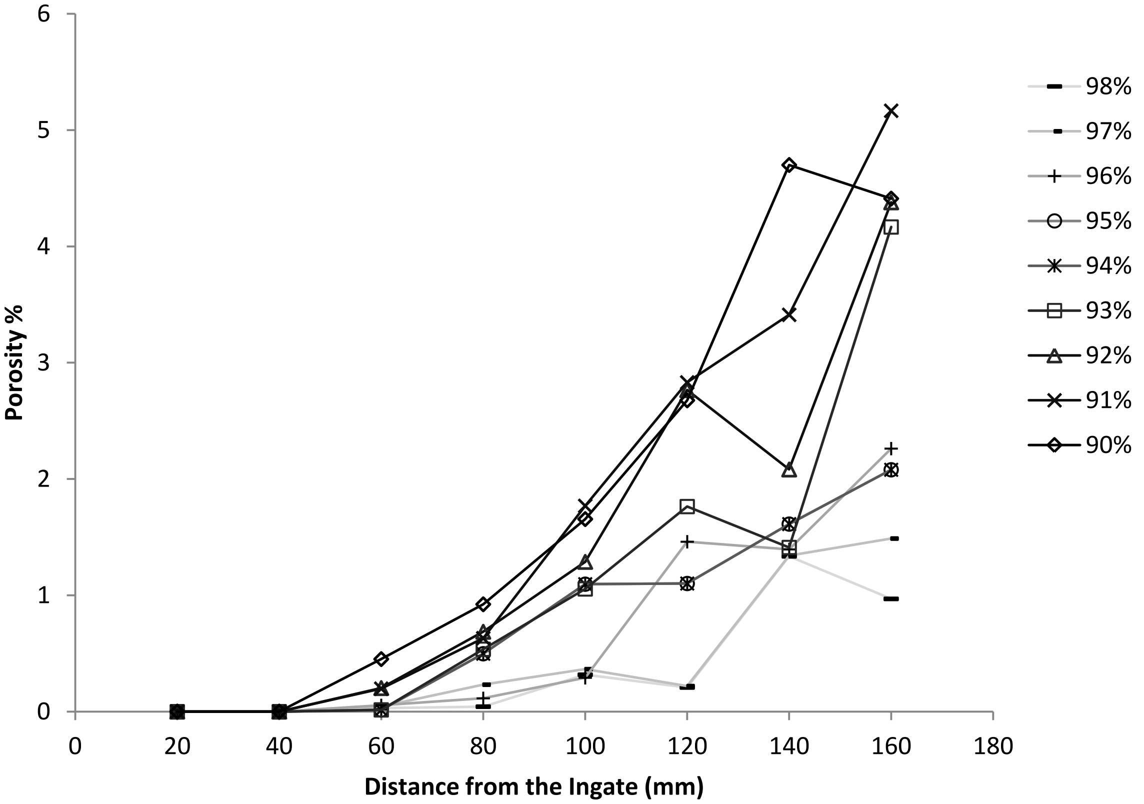

Figure 53: Distribution of porosity at 8 selected points along the centreline of the AlCu4 model casting for a range of feeding effectiveness values. Measurements were taken at 20,40,60,80,100,120,140,160mm from the bottom of the casting.

5.13.3 Calibrated Model Simulations

Figure 54 shows the results of the new A20X thermophysical property database and the predicted porosity distributions it produces in varying feeding conditions within MAGMASOFT. The images show both the centreline porosity profiles along the x and y planes in the model. The effectiveness of feeding was varied from 10% (far left) to 30, 50 and 80% (far right) to show the variation of porosity formation in an extreme range. Like the Al-4%Cu model, there is a bulb like formation in the 10% feeding condition which develops into a narrow tongue-like structure down the centre of the castings. When the feeding becomes high at 80% the porosity starts to dissipate towards the top of the casting becoming less and less with a shrinkage pool developing at the top of the casting. The images cut in the x-plane show that the shrinkage becomes more and more surface orientated as the feeding effectiveness is increased.

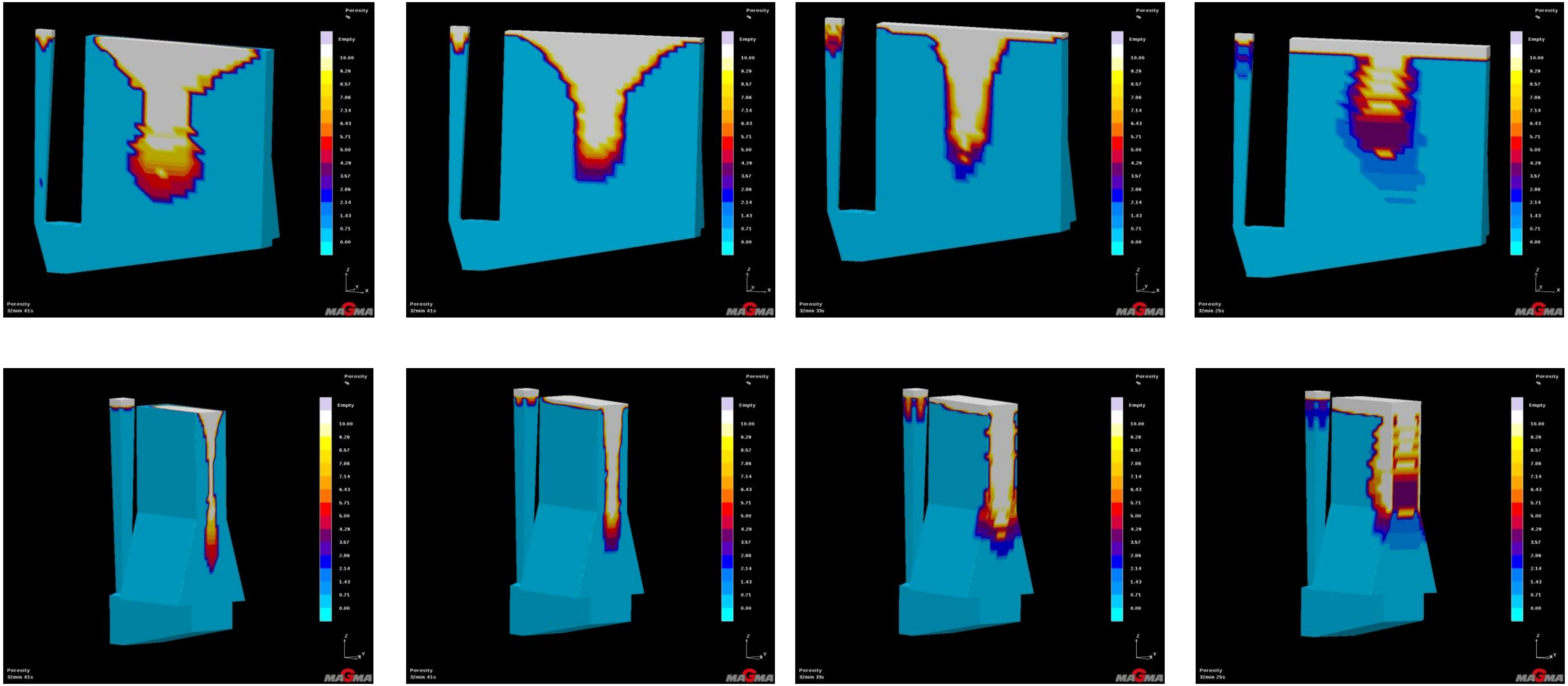

Figure 53: Formation of centreline porosity in both the X and Y planes in four differing feeding effectiveness conditions in MAGMASOFT using the new A20X thermophysical property database. From left to right: 10, 30, 50, 80% FE.

CHAPTER 6 DISCUSSION

6.1 Results Overview

This project has undertaken the design and casting of a simple geometry that produced differing porosity levels when cast in three alloys of nominally the same composition but with varying levels of grain refinement and substantially different microstructures. They were characterised quantitatively to determine the effects of varying levels of grain refinement on porosity and microstructure. As expected, the more grain refiner present (in the form of titanium and boron) the less porosity was seen; this was accompanied by a transition from a dendritic/cellular to fully globular microstructure Using the commercial casting simulation software MAGMASOFT, a thermophysical property database was developed to accurately simulate porosity formation for the A20X alloy. The properties were determined experimentally where possible. The porosity module (feeding effectiveness) within the model was then calibrated to try and accurately predict the effect grain refinement has on porosity. However, prediction of the absolute distribution of porosity within local volumes was not possible and the model predicted more porosity than was measured experimentally. A value for the feeding effectiveness parameter of 93% best fits the experimental data, as well as correlating with the onset of the eutectic phase of alloy solidification.

6.2 Correlation of the A20X model with Experimental Data

The first observation that should be made is the modification of thermophysical properties from the Al-4%Cu database to the A20X model yielded a change in the observed porosity distribution in the model. Comparing the distributions of porosity for each feeding effectiveness parameter between the two models conditions, the A20X model in general predicts a lower level of porosity with a graduated distribution along the centreline from the bottom to the top of the casting. The 97 and 98% conditions in the Al-4%Cu$_4$ model (figure 54) did show lower total porosity formed which seems to suggest an error with the model as higher levels of feeding would result in less porosity formation not more.

Figure 54 and 55 show the amalgamated porosity data from all three cast alloys and the respective predicted porosity data from both Al-4%Cu and A20X models. There appears to be no resolvable correlation of porosity distribution between the three cast alloys and the modelled data. A series of feeding effectiveness parameters were modelled, 90-98%, as this range captured the levels of porosity measured in the castings. Models in which the feeding effectiveness was set to less than 90% were not assessed as the predicted porosity fraction exceeded the experimental data substantially.

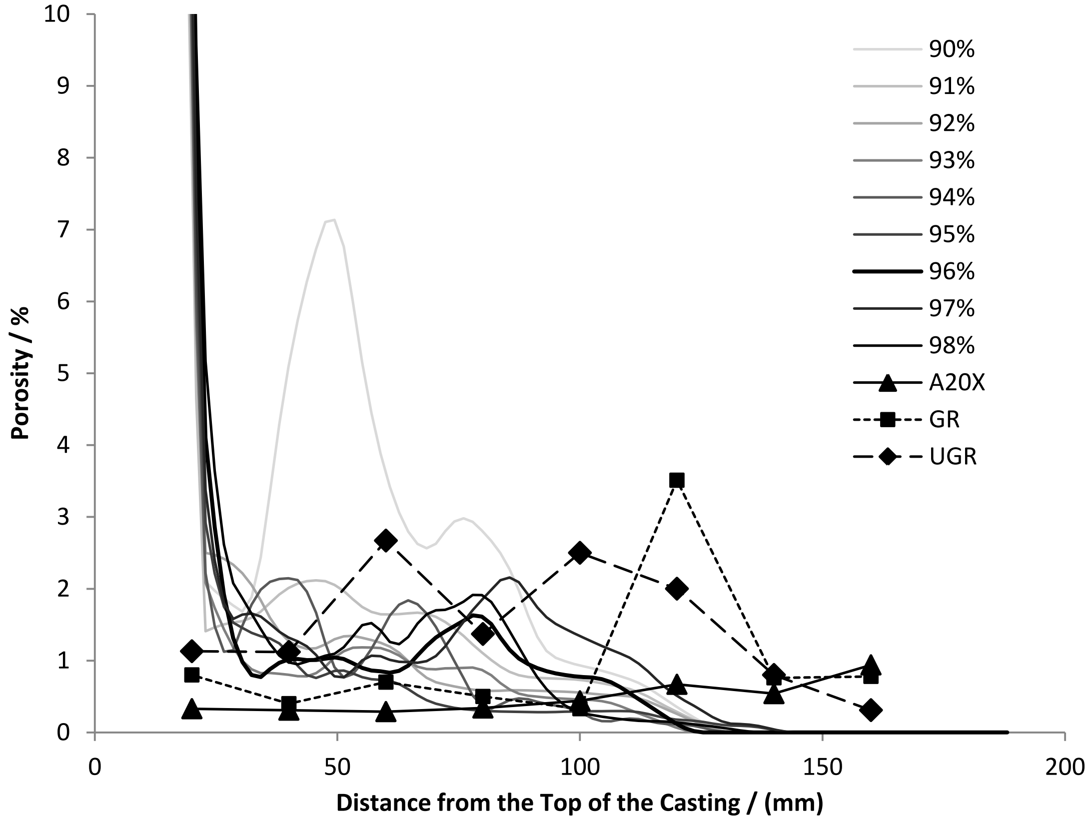

Figure 54: Collated centreline porosity data from the three cast alloys and the predicted from the A20X model for a range of feeding effectiveness conditions

The inability of the A20X model to simulate accurately the distribution of porosity in the real casting at a local level is likely to be because the MAGMASOFT software cannot account for the heterogeneous nucleation of pores that occurs in real castings (Campbell 2003) and thus the stochastic element of porosity formation throughout the casting is missing. This is a limitation that is not unique to MAMGMASOFT, all commercial casting simulation software contain such limitations. The only approach reported to date that accounts for the heterogeneous effect of oxides nucleating solidification porosity is that reported by Ohnaka (2004).

At face value it may simply be surmised that the thermal model is in error, and thus the calculated porosity distribution that is derived from the calculated thermal fields is also in error. However, it has been seen in Figures 28 and 31 that there is an excellent correlation between the measured thermocouple profiles and their simulated counterparts.

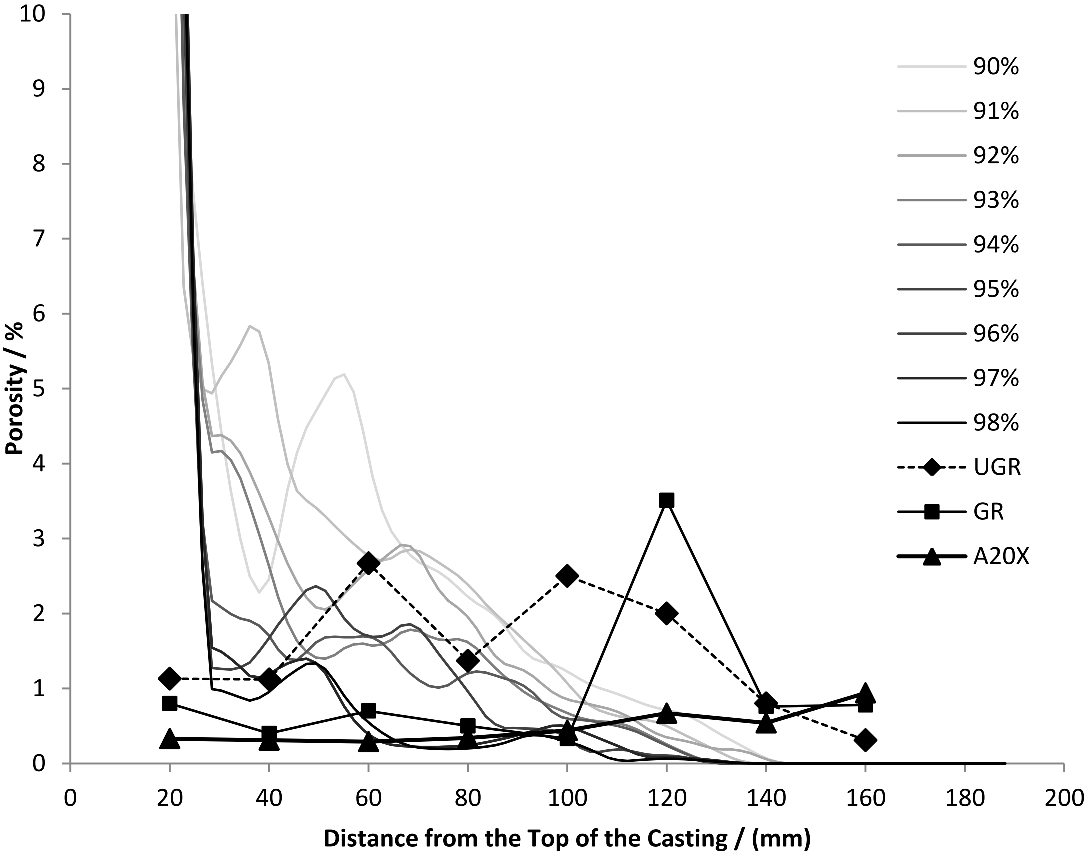

Figure 55 Collated centreline porosity data from the three cast alloys and the predicted from the AlCu4 model for a range of feeding effectiveness conditions

The A20X model does yield a more accurate prediction of the global severity of porosity in the A20X alloy. Table 9 shows the average (total) porosity obtained using the A20X and Al-4%Cu models in each feeding effectiveness condition and for the experimentally cast alloys. There is a very close match between the experimental average porosity of the A20X casting (0.482%), and average predicted porosity value of 0.467% over the same eight points at a feeding effectiveness value of 93%. This is better represented in figures 56 and 57 which illustrate the like for like porosity values at the eight isolated points measured in the castings and the model for both A20X and the Al-4%Cu databases. They illustrate both the disparity in accuracy between the models prediction of porosity at a local level in various regions but also that the amounts of total porosity are of a similar scale. Comparing the two figures also shows that the new A20X model does predict more accurately the global porosity formation compared with

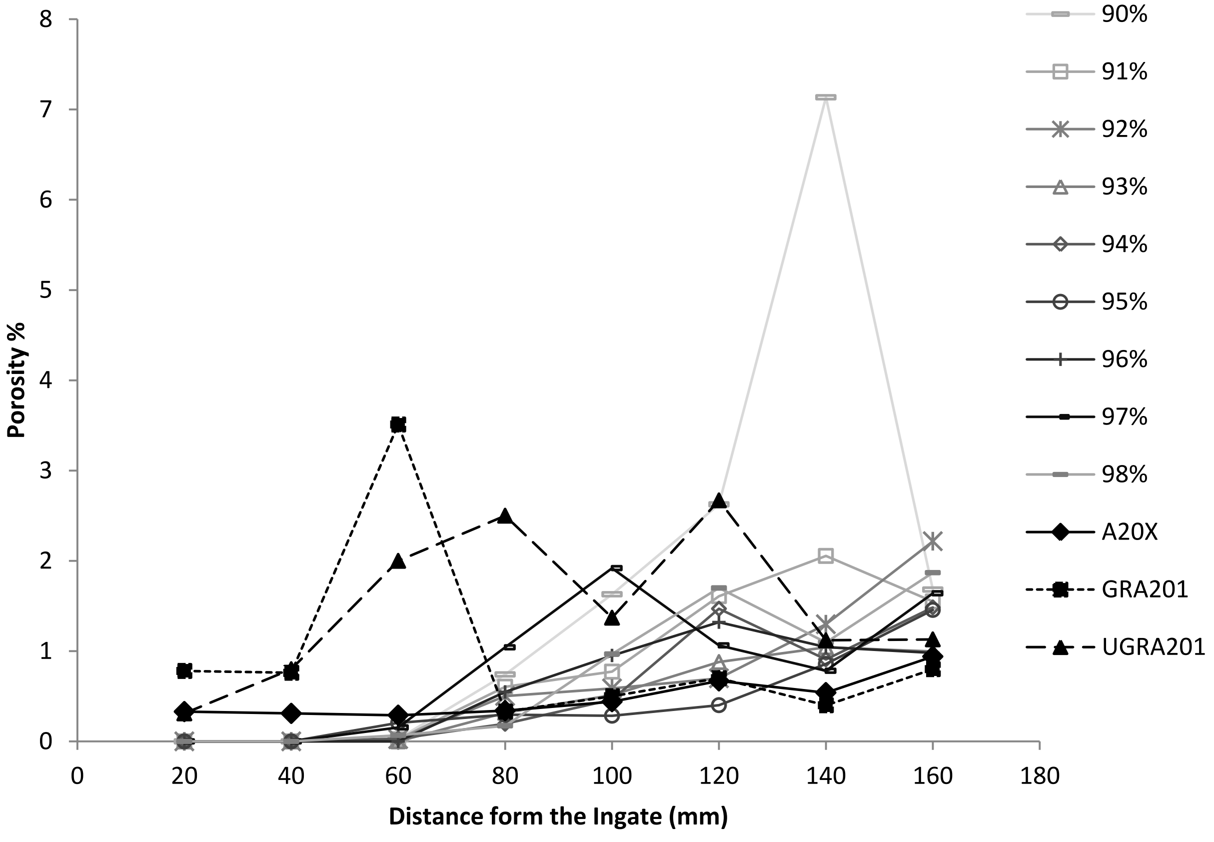

Figure 56: Collated centreline porosity data from the three casting alloys and the predicted from the A20X model (8pts) for a range of feeding effectiveness conditions.

the Al-4%Cu model making it a better tool to model the alloy.

Table 9 Average Total Porosity (8pts) of the two MAGMASOFT models: A20X and AlCu4 for a range of feeding effectiveness conditions (90-98%) and the three cast alloys: A20X, GRA201 and IA201.

MAGMASOFT FE %	A20X Model Average predicted porosity (%)	AlCu4 Model Average predicted porosity (%)	Alloy	Experimentally determined average porosity (%)
90	1.609568327	1.852305556	A20X	0.4825
91	0.756613027	1.750888889	GR A201	0.9725
92	0.578413793	1.4255	I A201	1.4875
93	0.46701788	1.118541667		
94	0.558163474	0.800277778		
95	0.383772669	0.760277778		
96	0.585802043	0.697138889		
97	0.796902937	0.461333333		
98	0.674111111	0.362875		

It should be noted that the feeding effectiveness (93%) that correlates most accurately with experimental measurement is also the fraction solid at which the eutectic transformation begins (0.93). This correlation with the onset of the eutectic reaction alloy may suggest that the copious nucleation seen in the A20X alloy allows feeding by liquid, mass and Darcy flow (section 2.9) right up to the start of solidification of the eutectic phases and consequently the reduction in classic shrinkage porosity.

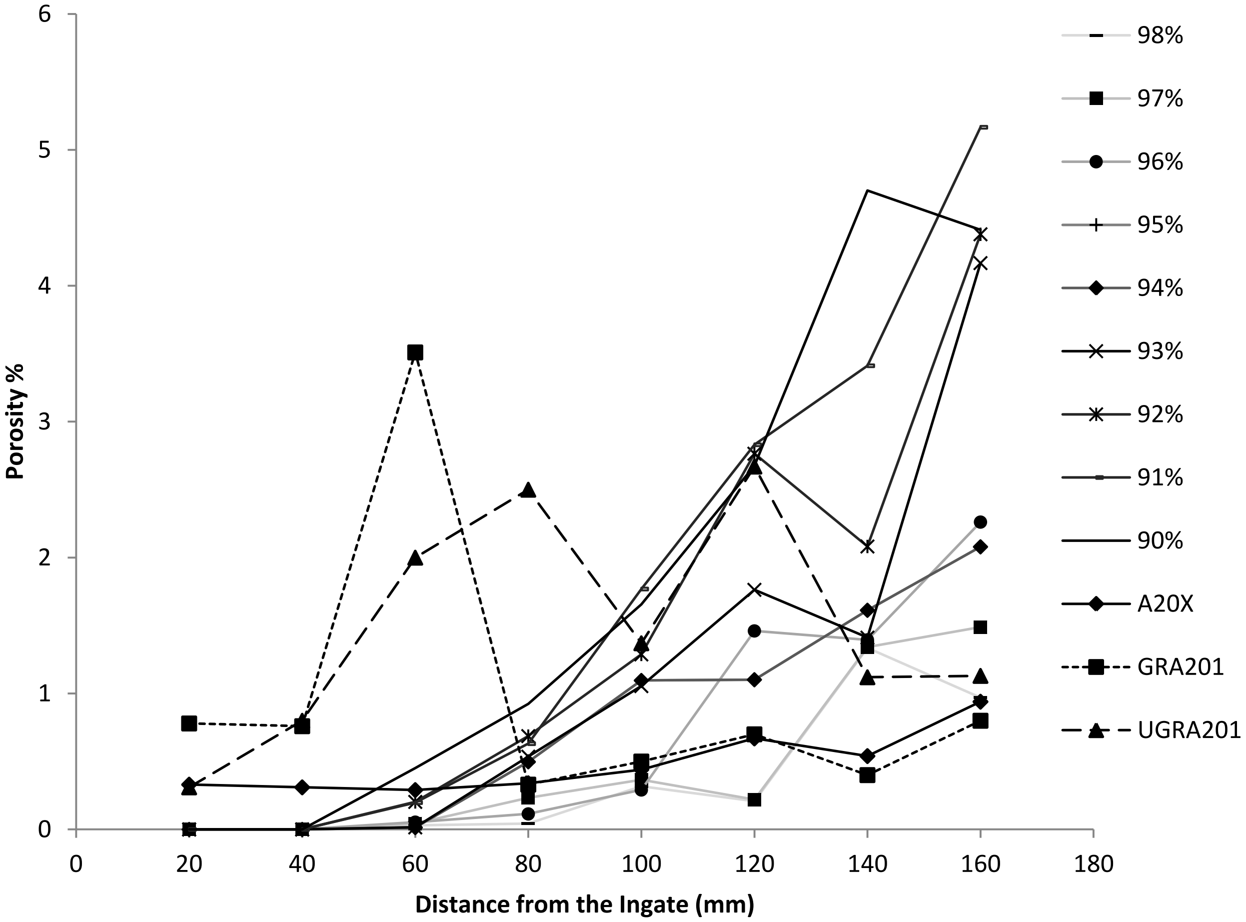

Figure 57: Collated centreline porosity data from the three cast alloys and the predicted from the $AlCu_4$ model (8pts) for a range of feeding effectiveness values.

Throughout the range of feeding effectiveness conditions in the Al-4%Cu model there is steeper increment in porosity development as you move up the centreline of the casting as compared with the A20X model data. It ultimately predicts higher levels of porosity at each measured point along the casting centre as well as total average porosity (table 8) compared with the A20X model at the same feeding effectiveness conditions except for the 97 and 98% conditions. The first point correlates well with the proposition that the A20X alloy has better feeding properties. The two conditions where it is the opposite however are of interest. Having already stated that the A20X alloy may allow liquid, mass and Darcy flow feeding mechanisms to be active right up to the solidification of the eutectic phases (93% f_s), it can be said with confidence that the A20X alloy is not working at either of these high values (97 or

98%) as they surpass this eutectic formation point which are the last solid to form in the alloy (see table 1 for solidification reactions of A201 alloy) and are thus unrealistic values.

6.3 Improvement of Feeding Effectiveness and reduction of Porosity in A20X Alloy

Porosity in aluminium castings is a problem relating to the release of dissolved hydrogen and solidification shrinkage. From the quantitative optical measurements of porosity taken for each alloy on the centreline of each casting, A20X shows the least. The pore morphologies and sizes (Figures 36-38) indicate that they are not due to dissolved hydrogen, the observed pores being substantially smaller in size than those reported by Lee et al (2001). This decrease in porosity formation is possibly linked instead with the enhanced ability of an alloy to feed during solidification (Campbell 1969). The metallographic analysis of the alloys shows a difference in the morphologies in the microstructures of the alloys (figures 36, 37, 39). Depending on the effectiveness of any grain refiners there is a scale of structures that can be formed in aluminium alloys; from a fully dendritic structure to a more refined cellular rosette-like structure and finally to a fully refined globular structure (section 2.6) and (Arnberg et al 1996). The A20X alloy is comprised of a fully refined globular structure with a more uniform grain shape and size due to the high levels of grain refinement (see table 3) compared with that of the lesser refined alloys GRA201 and IA201 which have a cellular structure of larger grain size (Figures: 36, 37 and 38). The absence of the fully dendritic coarse grain structure in the IA201 can be explained by reviewing the analysis of composition (Table 3), there being some grain refiner present, as shown by the presence of boron. It appears logical to propose that a change in the morphology of a solidifying alloy would change the alloy’s rheological properties and with it the feeding properties.

Rheology has been reported to affect directly the feeding effectiveness of an alloy and the relative significance of each mechanism throughout solidification. It is clear from the conclusions of (Campbell 1969) that the key mechanisms involved in the feeding of these long freezing range Al-Cu alloy systems that affects the formation of porosity are interdendritic and solid feeding with mass feeding not reported as having a significant role, as the critical stages of feeding occur long after mass feeding has normally finished. The mass and interdendritic feeding mechanisms described in sections 2.10.2 and 2.10.3 are first the movement of the partially solidified metal and liquid (mass) and following impingement of grains formation of a pasty zone where interdendritic feeding starts to dominate and the flow of remaining liquid feeds the solidification shrinkage. Dendrite coherency often marks the transition point between the two feeding mechanisms – mass and interdendritic (Arnberg et al 1995) – as the growing dendrites impinge upon one another. The onset of development of strength in the mushy zone and the dominance then of interdendritic feeding via Darcy flow then dominates. It should be noted that initially the contacting solid network is skeletal and weak. The rigidity point or maximum packing fraction then is the point in which solid particles coarsen or ripen, interlocking and providing the mushy zone with measureable strength (Dahle and StJohn 1998), Figure 65. After this point, interdendritic feeding becomes harder still as feed paths narrow due to continuing side arm coarsening (Kurz and Fisher 1986) and increased pressure gradient is required to sustain the creeping capillary flow. (Arnberg et al 1996) measured the coherency and rigidity points of a series of aluminium casting alloys (A356, A357, A380, A390, A413, A201, A206) and A201 was measured as 21% and 64% fraction solid respectively (figure 58).

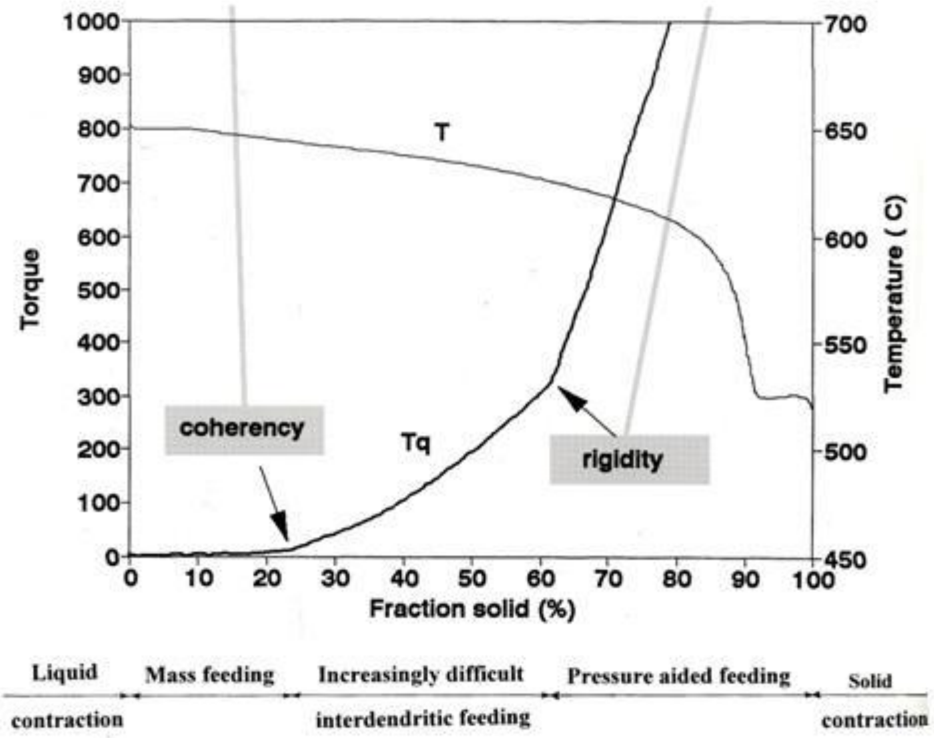

Figure 58: A schematic representation of the feeding stages related to interdendritic development from the solidification process of the A201 alloy highlighting the coherency and rigidity points (Arnberg et al 1996)

The effect grain refinement has on the dendrite coherency point has been found to be significant, with coherency being prolonged in several cases: (Malekan and Shabestari 2009) using an A319 alloy, (Arnberg et al 1996) presented torque vs. Fraction solid data on A356, A380, A413, A528 and A713 and (Veldman et al 2001) with AlSi7Mg, AlSi11Mg and AlCu4 alloys. All alloys exhibited an offset of the coherency point to higher f_s with the modification of grain morphology to a small globular morphology from their original more dendritic/rosette-like structures.

The torque data from Arnberg and co-workers (1996) illustrates perfectly that by initiating many smaller crystals coherency and rigidity points are delayed to higher solid fractions, therefore postponing the harder feeding stages. The residual deficit in feed metal left is less and as a consequence of prolonging the mass feeding mechanism and the overall magnitude and severity of the driving force for microporosity formation and growth is thereby reduced.

In 3D models of globular grain growth using Voroni tessellation methods, Phillion et al (2006) reported the influence of cooling rate during solidification on the fraction of solid at which percolation of solid within the liquid occurs (formation of an interconnected network of solid instead of liquid throughout the volume). Results are summarised in Figure 59.

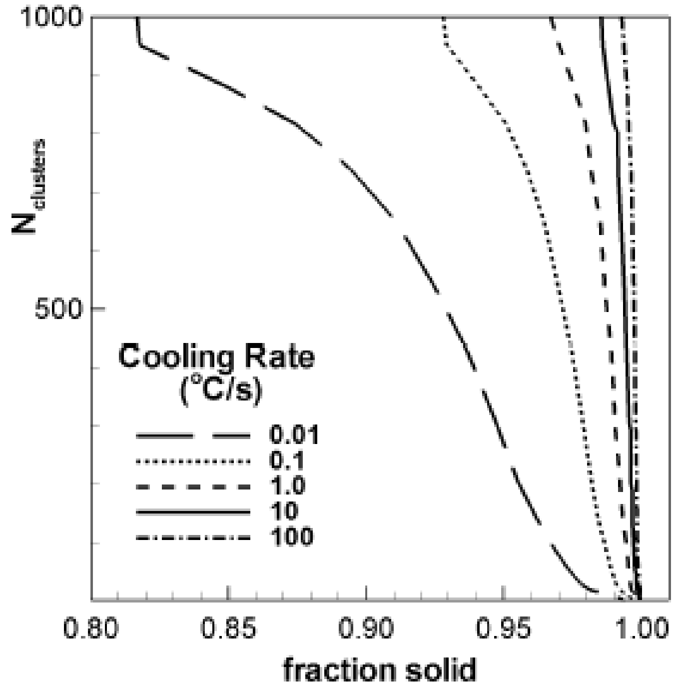

Figure 59: Effect of cooling rate of the evolution of number of solid grain clusters
(Phillion et al 2006)

This continuity of solid and liquid has a large effect on defect formation in castings, marking the maximum fraction solid at which grain movement can contribute to feeding. At a cooling rate of 0.1°C/s (which is comparable with the alloys cast in this investigation) percolation of solid occurs at a solid fraction of 0.93, which again coincides with that of the A20X model feeding parameter (93%). It could be hypothesised that at this 0.93 solid fraction a solid network of developing grains forms which then halts the mass feeding mechanism (total rigidity) leaving the residual, isolated, liquid channels unfed by mechanisms other than solid feeding.

6.3 Modelling Uncertainties

Dendrite coherency highlights that within the feeding mechanisms even subsequent to coherency, Darcy flow occurs. The feeding effectiveness parameter accounts for both Darcy and mass feeding in the model as an aggregated effect. The feeding effectiveness function in the MAGMASOFT software is unable to separate out the two highly significant mechanism of feeding; thus, in seeking to optimise the model for A20X it has only been possible to establish the general trend of combined effect of all the feeding mechanisms.

In the experimental determination of a thermophysical property database for the A20X alloy there remains an unresolved uncertainty with respect to the calculation of C_p (specific heat). The high temperature DSC had an irresolvable software error that meant the data had to be post processed in order to correctly account for the machines baseline properties (section 5.12.4). However, this possible error is repeated systematically throughout all simulations and does not appear to have led to any significant errors in calculated local solidification times (sections 5.5 and 5.6).

An assumption was also made when calculating the fraction solid curve of the A20X alloy. As the majority phase is dilute aluminium, densities for both solid and liquid aluminium were used. The partition coefficient for the Al-Cu phase diagram is 0.17 (Smithells Metals Reference Book 8th edition) supports this assumption. Results showed that the eutectic phase occurred when 7% liquid remains and the evolution of the fraction solid curve was different to that of the similar alloy (Al-4%Cu) in the MAGMASOFT database.

Overall, it is concluded that the remaining uncertainties in material properties had no significant effect on the model accuracy and they are acceptable for use in simulation of commercial casting processes with A20X alloy.

CHAPTER 7 CONCLUSIONS

Based on the results obtained within this project, the following conclusions can be made:

1. A thermophysical property database has been developed along with the identification of a feeding effectiveness parameter that can be used in the simulation of a casting of the aluminium alloy A20X. Results calculated with the model show good general agreement with experimentally observed porosity levels.

2. The A20X alloy exhibits less porosity than that of the two less fully refined alloys as a consequence of the more effective feeding behaviour of the alloy due to the globular morphology of the grains, a result of higher levels titanium and boron.

3. In the A20X alloy, mass feeding is proposed to occur up to the point of eutectic formation, 0.93 f_s because of its improved feeding characteristics.

4. The MAGMASOFT software package is unable to account for the heterogeneous nature of porosity development and so cannot predict local porosity evolution throughout the whole casting accurately.

CHAPTER 8 FURTHER WORK

Having completed this research, there are areas for further development that would advance the understanding and increase the modelling capabilities of the A20X alloy.

1. Produce additional castings to verify the model database for A20X.

2. Repeat the specific heat capacity measurements using an appropriate high temperature DSC method to elicit accurately the C_p of the A20X alloy.

3. Experimentally determine the rheological properties of the A20X alloy (Torque Paddle tests) specifically to establish the coherency and rigidity points for the further analysis of the alloy in the semi-solid state and consequently understand feeding properties more quantitatively.

CHAPTER 9 REFERENCES

Andrew, J.H., Percival, R.T., & Bottomley, G.T.C. 1936. *Iron and Steel Special Report*, 15, 43-64.

Anson, J.P., & Gruzleski, J.E. 1999. Effect of Hydrogen Content on Relative Shrinkage and Gas Microporosity in Al7% Si Casting. *AFS Transactions*, 107, 135-142.

Apelian, D., Sigworth, G.K., & Wahler, K.R. 1984. Assessment of Grain refinement and Modification of Al-Si Foudry Alloys by Thermal Analysis. *AFS Transactions*, 92, 297-307.

Arnberg, L. 2008. Castability-Fluidity and Hot Tearing. Metals Handbook, *ASM*, 375.

Arnberg, L., Backerud, L., & Chai, G. 1996. **Solidification Characteristics of Aluminium Alloys: Dendrite Coherency Vol 3**, AFS Des Plaines, Ilinois.

Arnberg, L., Dahle, A.K., Paradies, C.J., Syvertsen, F. 1995. Feeding Mechanisms in Aluminium Foundry Alloys. AFS Transactions,103, 753-760.

Atwood, R.C., & Lee, P.D. 2003. Simulation of the Three Dimensional Morphology of Solidification Porosity in an Aluminium-Silicon Alloy. *Acta Materialia*, 51 (18), 5447-5466.

Backerud, L., Chai, G., & Tamminen, J. (1990). **Solidification Characteristics of Aluminium Alloys: Foundry Alloys Vol.2**. (9th edn.) AFS, Scanaluminium. Oslo.

Baker, W.A. 1945. *Journal. Institute of Metals*, 71, 165-204

Brody, H.D. & Flemings, M.C. 1966. Solute Redistribution in Dendritic Solidification. *Transactions of the Metallurgical Society of Aime*, 236, (5) 615-&.

Cahoon, J.R., Tandon, K.N., & Chaturvedi, M.C. 1992. Effect of Gravity level on Grain Refinement in Aluminium Alloys. *Metallurgical Transactions A*, 23A, 3399-3404.

Campbell, J. 1969. Feeding Mechanisms in Castings. *Cast Metals Research Journal*, 5 (1), 1-8.

Campbell, J., 2003. **Castings**. (2nd edn.) Butterworth-Heinemann, Oxford.

Chai G., 1994. PhD Thesis, Stockholm University, Chem. Com. No.1.

Chien, K.H., Kattamis, T.Z., & Mollard, F.R. 1973. Cast Microstructure and Fatigue Behavior of A High-Strength Aluminum-Alloy (Ko-1). *Metallurgical Transactions*, 4, (4) 1069-1076.

Chiesa. R., Fuoco, R., & Gruzleski, J.E. 1994. Porosity Distribution in Directionally Solidified Test Bars Sand Cast from a Controlled A356 Melt. *Cast Metals Journal*, 7 (2) 113-122.

Clyne, T.W., & Davies, G.J., A Quantitative Solidification Test for Casting and an Evaluation of Cracking in Aluminium-Magnesium Alloys. *The British Foundrymen*, 68, 238-244.

Darcy, H. P. G., 1856, **Les Fontaines Publiques de la Ville de Dijon.** Dalmont, Paris.647

Dahle, A.K., & St.John, D.H. 1998. Rheological Properties ofthe Mushy Zone and its effect on the formation of Defects during Solidfication. *Acta Materialia*, 47 (1), 31-41.

Dahle, A.K., Tondal, P.A., Paradies, J.J., & Arnberg, L. 1996, Effect of grain refinement on the fluidity of two commercial Al-Si foundry alloys. Metallurgical and Materials Transactions A, 27, 2305–2313.

Davidson, C., Viano, D., Lu, L., & StJohn, D. 2006. Observation of Crack Initiation during Hot Tearing, *International Journal of Cast Metals Research*, 19, 59-65.

Di Sabatino M. & Arnberg L., 2004. A Review on the Fluidity of Aluminium Alloys, *Met Science and Technology Teksid*, 22 (1), 9-15.

Di Sabatino, M. & Arnberg, L. 2009. Castability of aluminium alloys. *Transactions of the Indian Institute of Metals*, 62, (4-5) 321-325.

Di Sabatino, M., Arnberg, L., Brusethaug, S., & Apelian, D. 2005. Fluidity evaluation methods for Al-Mg-Si alloys. *International Journal of Cast Metal Research*, 19 (2), 94-97.

Din, T. & Campbell, J. 1996. High strength aerospace aluminium casting alloys: A comparative study. *Materials Science and Technology*, 12, (8) 644-650.

Easton, M. & StJohn, D. 1999. Grain refinement of aluminum alloys: Part I. The nucleant and salute paradigms - A review of the literature. *Metallurgical and Materials Transactions A-Physical Metallurgy and Materials Science*, 30, (6) 1613-1623.

Eskin, D.G., Suyitno, Katgerman, L. 2004. Mechanical properties of the semi-solid state and hot-tearing of aluminium alloys. *Progress in Material Science*, 49, 429-711.

Fang, Q.T., Bruno, M.J. 1991. **Light Metals:1991**. (ed. E.L.Rooy), TMS, Warrendale, PA.

Fang, Q.T., Granger, D.A. 1989. Porosity Formation in Modified and Un-modified A356 Alloy Castings. *AFS Transactions*, 97, 989-1000.

Flemings, M.C. 1974. **Solidification Processing.** (2nd edn.) McGraw-Hill, New York.

Flemings, M.C. 1974a. Solidification of Castings. *Scientific American*, 231, (6) 88-95.

Flemings, M.C. 1974b. Solidification Processing. *Metallurgical Transactions*, 5, (10) 2121-2134.

Fuoco, R., Correa, E.R., & Andrade Bastos, M.D. 1998. Effects of Grain Refinement on **Feeding** Mechanisms in A356 Aluminium Alloy. *AFS Transactions*, 108, 401-409.

Ghosh, A. 1990. **Principals of econdary processing anjd casting of liquid steel**. (Ch.6,7,9) New Dehli: Oxford and IBH.

Glasson, E.L., Emley, E.F. 1968. **The Solidification of Metals**. (110) Iron and Steel Institute., London

Gulliver, G.H. 1913. *Journal. Institute of Metals*, 9, 120-157.

Guzowaski, MM., Sigworth, G.K., & Sentner, D.A. 1987. *Metallurgical Transactions A*, 18A, 603–619.

Hansen, P.N., & Sahm, P.R. 1988. How to Model and Simulate the Feeding Process in Casting to Predict Shrinkage and Porosity Formation. *Modelling of Casting and Welding Process IV*, TMS-AIME, 33-42.

Harinath, U., Nrayana, K.L., & Roshan, H.M. 1979. Studies on Volume Deficit of LM6 Alloy in Shell Molds. *AFS Transactions*, 87, 231-238.

Hattel, J., Pryds, N., Thorborg, J., Lipinski, M., & Spneider, M. 2005. MAGMASOFT. **Fundamentals of Numerical Modelling of Casting Processes**. Polyteknisk Forlag, Denmark.

in the A356 Casting Alloy System. *AFS Transactions*, 101, 401-413.

Jones, G.P. & Pearson, J. 1976. Factors Affecting Grain Refinement of Aluminum Using Titanium and Boron Additives. *Metallurgical Transactions B-Process Metallurgy*, 7, (2) 223-234.

Kuo,Y.S., Chang, E., & Lin, Y.L. 1989. The feeding effects of risers on the mechanical properties of A201 Al allo plate castings. *AFS Transactions,* 97, 777-782.

Kurz, W., & Fisher, D.J. 1989. **Fundamentals of Solidification**, (3rd edn.) Trans Tech Publications, Brookfield, VT

Lee, Y.E., Chang, E., & Chieu, C.F. 1990. Modeling of Feeding Behavior of Solidifying Al-7Si-0.3Mg Alloy Plate Casting, *Metallurgical Transactions B*, 21, 715-722B.

Lee, Y.E., Chirazi, Atwood, R.C. Wang. 2003. Multiscale Modelling of Solidification Microstructures including Microsegregation and Microporosity, in an Al–Si–Cu Alloy. *Material Science and Engineering.*

Li, S. 2010. Hot Tearing in Cast Aluminium Alloys: Measures and Effects of Process Variables. PhD Thesis, Worcester Polytechnic Institute, Worcester, USA, 43-86.

Loitti, E., & Previtali, B. 2006. Study of the Validity of the Niyama Criterion Applied to the AlSi7Mg Alloy. *La Metallurgia Italiana*.

Loper Jr, C.R. 1992. Fluidity in Aluminium Silicon Casting Alloys. *AFS Transactions*, 100, 533-538.

Luck, R., Berry, J.T., &Taylor, R.P. 1999.Solidification Modelling and Porosity Control in Aluminium Alloys. TAFS, 107, 203-206.

MAGMASOFT. 2011. Olive, Simn, Maxima Engineering Ltd, Provate Communication.

Malekan, M., & Shabestari, S.G. 2009. Effect of Grain Refinement on the Dendrite Coherency point during Solidification of the A319 Aluminium Alloy. Metallurgical and Materials Transactions A, 40A (13), 3196-3202.

Mayers, C.D., McCartney, D.G., & Tatlock, G.J. 1993. *Journal of Material Science and Technology*, 9, 97-103.

Mccartney, D.G. 1988. Discussion of the Role of Boron in the Grain-Refinement of Aluminum with Titanium. *Metallurgical Transactions A-Physical Metallurgy and Materials Science*, 19, (2) 385-387.

Metz, S.A., & Flemings, M.C. 1970. A Fundamental Study of Hot Tearing. *AFS Transactions*, 78, 453-460.

Mollard, F.R. 1969. Metallography as a Quality Control Tool for KO-1 Alloy Castings. *AFS Transactions,* 77, 368-372.

Mollard, F.R. 1970. Influence of Chemical Composition and Heat Treatment on Properties of KO-1 Alloy. *AFS Transactions,* 78, 443-449.

Mollard, F.R., Flemings, M.C., & Niyama, E.F. 1987. Aluminum Fluidity in Casting. *Journal of Metals*, 39, (11) 34-37.

Monroe, R. 2005. Porosity in Castings, *AFS Transactions*, 113, 519-545.

Morthland,T.E., Byrne, P.E. Tortorelli, D.A., & Dantzig, J.A. 1995. Optimal Riser Design for Metal Casting, *Metallurgical and Material Transactions B*, 26B, 1995, 871-885.

Mullins. W.W., & Sekerka, R.F. 1963. Morphological Stability of a Partical Growing by Diffusion or Heat Flow. *Journal of Applied Physics*, 34, (2), 323-329.

Murty, B.S., Kori, S.A., & Chakraborty, M. 2002. Grain refinement of aluminium and its alloys by heterogeneous nucleation and alloying. *International Materials Reviews*, 47, (1) 3-29.

Niyama, E., Uchida, T., Morikawa, M., & Saito, S. 1982. A method of shrinkage prediction and its application to steel casting practice. *AFS International Cast Metals Journal,* **9**, 52–63.

Ohnaka, I., Sugiyama, a., Onda, H., Kimatsuka, A., Yasuda, H. Zhu, J-D., & Zhao, H. 2004. Porosity Formation Mechanism in Al-and Mg-Alloy *Castings and its Direct Simulation. Melting and Solidification Processes VI*, (6th Pacific Rim Conference).

Overfelt, R.A., Bakhtiyarov, S.I., Wang, D., & Taylor, R.E. 2002. Thermophysical Properties of 201 Aluminum, Ductile Iron and Sebiloy II. *AFS Transactions*, 110 (1), 257-266.

Pearson, J. & Birch, M.E.J. 1979. Effect of the Titanium - Boron Ratio on the Efficiency of Aluminum Grain-Refining Alloys. *Journal of Metals*, 31, (11) 27-31.

Pellini, W.S. 1952. Strain Theory of Hot Tearing. *Foundry*, 80, 125-199.

Phillion, A.B., Desboilles, J.L., & Rappaz, M. 2006. A 3D Granular Model of Equiaxed-Granular Solidification. Modelling of Casting Welding and Advanced Solidification Processes*, TMS Publications,* Warrendale, USA.

Porter, D.A., Easterling, K.E. 1981. **Phase Transformations in Metals and Alloys**. (1st edn.) Chapman and Hall, London.

Pumphrey, W.I., & Lyons, J.V. 1948. Cracking during the Casting and Welding of the More Common Binary Aluminium Alloys. *Journal Institute of Metals*. 118, 439-455.

Reynolds, J.A. & Tottle, C.R. 1951. The Nucleation of Cast Metals at the Mould Face. *Journal of the Institute of Metals*, 80, (2) 93-102.

Saveiko, V.N. 1961. Theory of Hot Tearing. **Russian Castings Production**, (vol.11) 453-456.

Savitski, A., & Golay, M.J.E. 1964. Smoothing and Differentiation of Data by Simplified Least Squares Procedures. *Analytical Chemistry*, 36 (8), 1627-1639.

Scheil, E. 1942. *Zeitschrift für Metallkunde*, 9, 70-72.

Schumacher, P., Greer, A.L., Worth, J., Evans, P.V., Kearns, M.A., Fisher, P., & Green, A.H. 1998. New studies of nucleation mechanisms in aluminium alloys: implications for grain refinement practice. *Materials Science and Technology*, 14, (5) 394-404.

Sicha, W.E., Boehm, R.C. 1948. Grain Refinement in Al-4.5%Cu Alloys. *AFS Transactions*, 92, (56) 398-409.

Sigworth, G.K. 1996. Hot Tearing of Metals. *AFS Transaction*, 104, 1053 – 1062.

Smithells, C.J., & Brandes, E.A. 1998. **Smithells Light Metals Handbook** (7thEdn.) Butterworth-Heinemann.

Spittle, J.A. 2006. Grain refinement in shape casting of aluminium alloys. *International Journal of Cast Metals Research*, 19, (4) 210-222.

Stefanescu, D.M. 2005. Computer Simulation of Shrinkage-related Defects in Castings - a Review. *International Journal of Cast Metals*, 18, (3), 1–129.

Suri, V.K., Huang, H., Berry, J.T., & Hill, J.L. 1992. Applicability of Thermal Parameter-based Porosity Criteria to Long Freezing Range Aluminium Alloys. *AFS transactions* 100, 399-407.

Taghiabadi, R., Mahmoudi, M., Ghomy, M.E., & Campbell, J. 2003. Effect of Casting Techniques on Tensile Properties of Cast Aluminium Alloy (Al-Si-Mg) and TiB2 Containing Metal Matrix Composite. *Materials Science and Technology*, 19, (4) 497-502.

Tian, J., Xue, X.A., Zhang, Y.B., Gao, Y.L., Liu, L.Z., Sun, Q., Yuan, S.Y. 2003. Numerical Simulation and Shrinkage Defects Prediction of a Turbine Blade Investment Casting. *Journal of Materials Science & Technology*, 19 (1), 32-34.

Tiryakioglu M., Askeland D.R. & Ramsay C.W. Fluidity of 319 and A356: An Experimental Design Approach. *AFS Transactions*, 102, 17-25.

Turnbull, D. 1950. Kinetics of Heterogeneous Nucleation. *Journal of Chemical Physics*, 18, (2) 198-203.

Tynelius, K., Major, J.F., & Apelian, D. 1993. A Parametric Study of Microporosity in Al-Si Foundry Alloys. *AFS Transactions,* 101, 93-166.

Veldman, L.M., Dahle, A.K., St.John, D.H., & Arnberg, L. 2001. Dendrite Coherency in Al-Si-Cu S Alloys. *Metallurgical and Materials Transactions A*. 32 (1) 147-155.

Viswanathan, S., Sikka, V.K., & Brody, H.T. 1993. The Application of Quality Criteria for the Prediction of Porosity in the Design of Casting Processes. **Modelling of Casting Welding and Advanced Solidification Processes vol. VI**, *TMS*, 285–292.

Xue, X, 1985. A Criterion Function for Shrinkage Prediction in Carbon Steel Castings. MSc.

Zuo, Y., Li, H., Xia, M., Jiang, B., Scamans, G.M., & Fan, Z. 2011. Refining grain structure and porosity of an aluminium alloy with intensive melt shearing. *Scripta Materialia*, 64, (2) 209-212.

APPENDIX 1: Al-4%Cu Thermophysical properties

General Parameters

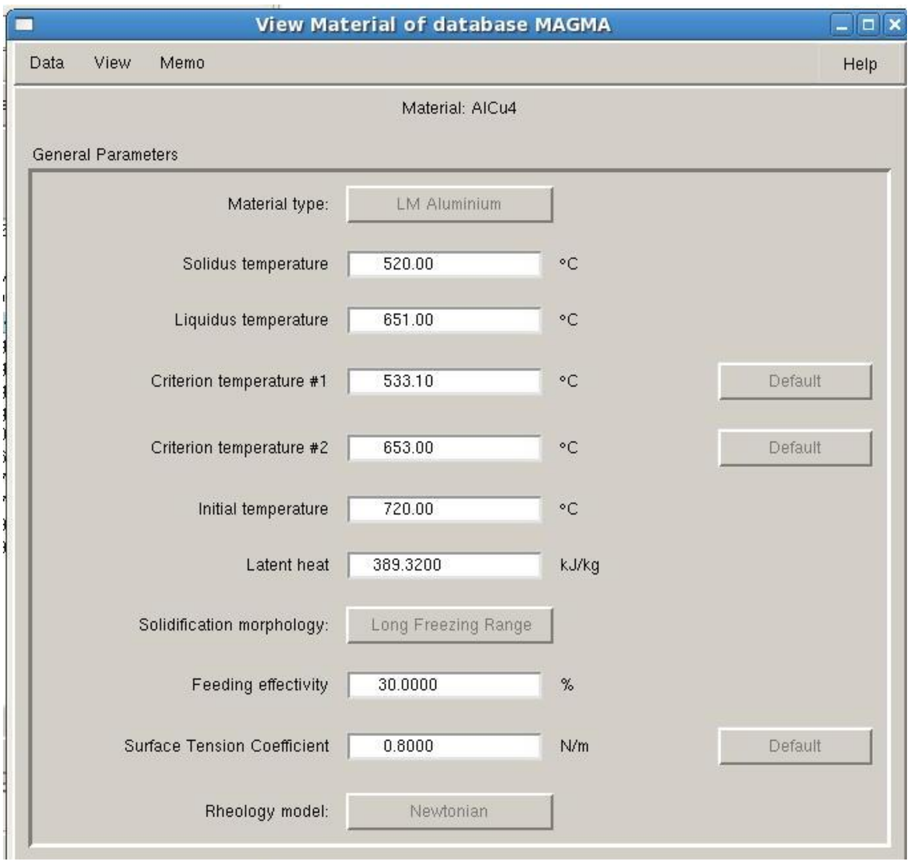

Material: AlCu4

General Parameters

Material type: LM Aluminium
Solidus temperature 520.00 °C
Liquidus temperature 651.00 °C
Criterion temperature #1 533.10 °C
Criterion temperature #2 653.00 °C
Initial temperature 720.00 °C
Latent heat 389.3200 kJ/kg
Solidification morphology: Long Freezing Range
Feeding effectivity 30.0000 %
Surface Tension Coefficient 0.8000 N/m
Rheology model: Newtonian

General Parameters of the $AlCu_4$ alloy taken directly from the MAGMASOFT database.

Thermal Conductivity

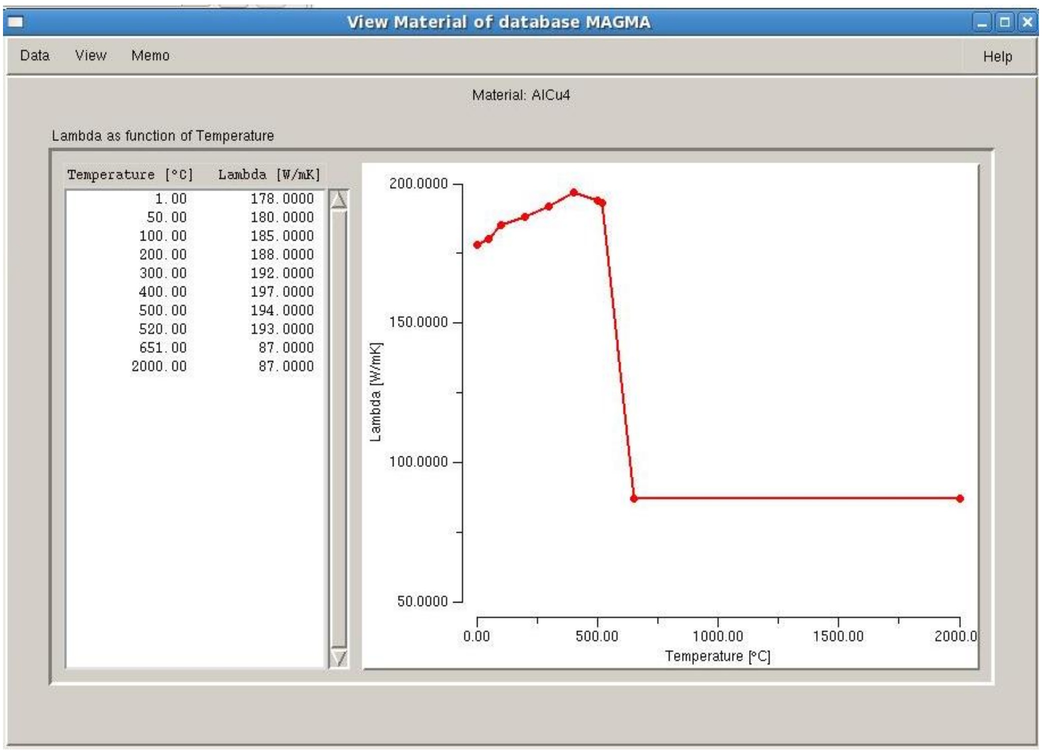

Material: AlCu4

Lambda as function of Temperature

Temperature [°C]	Lambda [W/mK]
1.00	178.0000
50.00	180.0000
100.00	185.0000
200.00	188.0000
300.00	192.0000
400.00	197.0000
500.00	194.0000
520.00	193.0000
651.00	87.0000
2000.00	87.0000

Thermal conductivity plotted as a function of temperature

Fraction of Solid

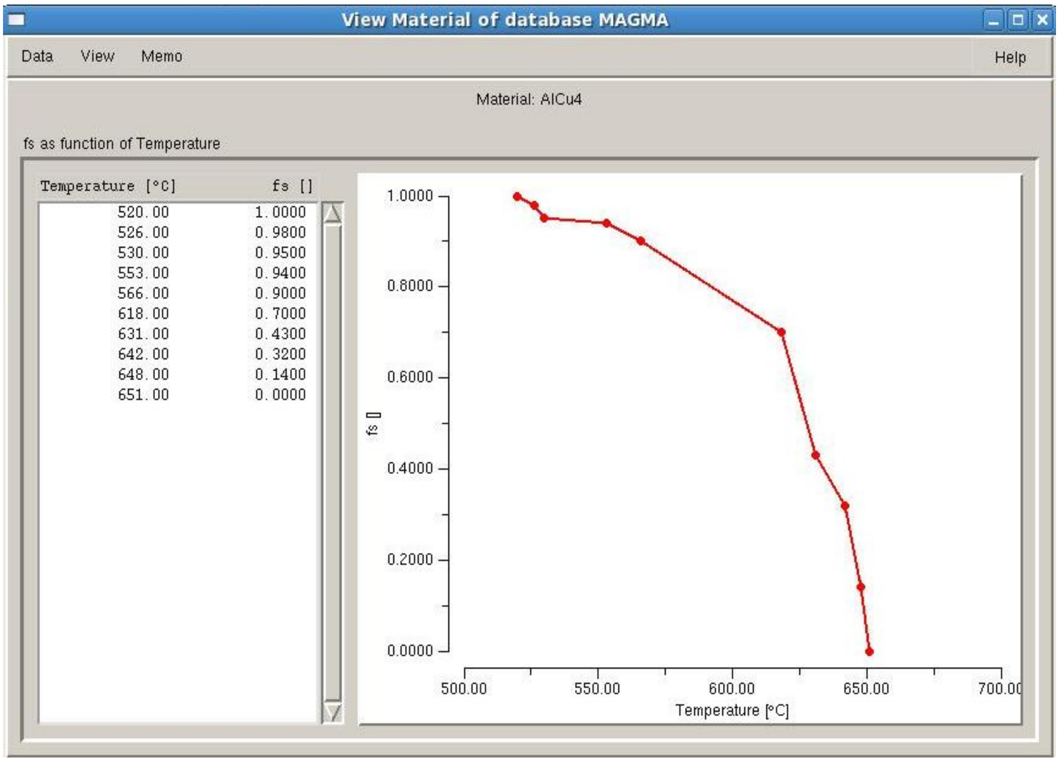

Material: AlCu4

fs as function of Temperature

Temperature [°C]	fs []
520.00	1.0000
526.00	0.9800
530.00	0.9500
553.00	0.9400
566.00	0.9000
618.00	0.7000
631.00	0.4300
642.00	0.3200
648.00	0.1400
651.00	0.0000

Fraction of solid curve for the Magma $AlCu_4$ alloy

Specific Heat Capacity

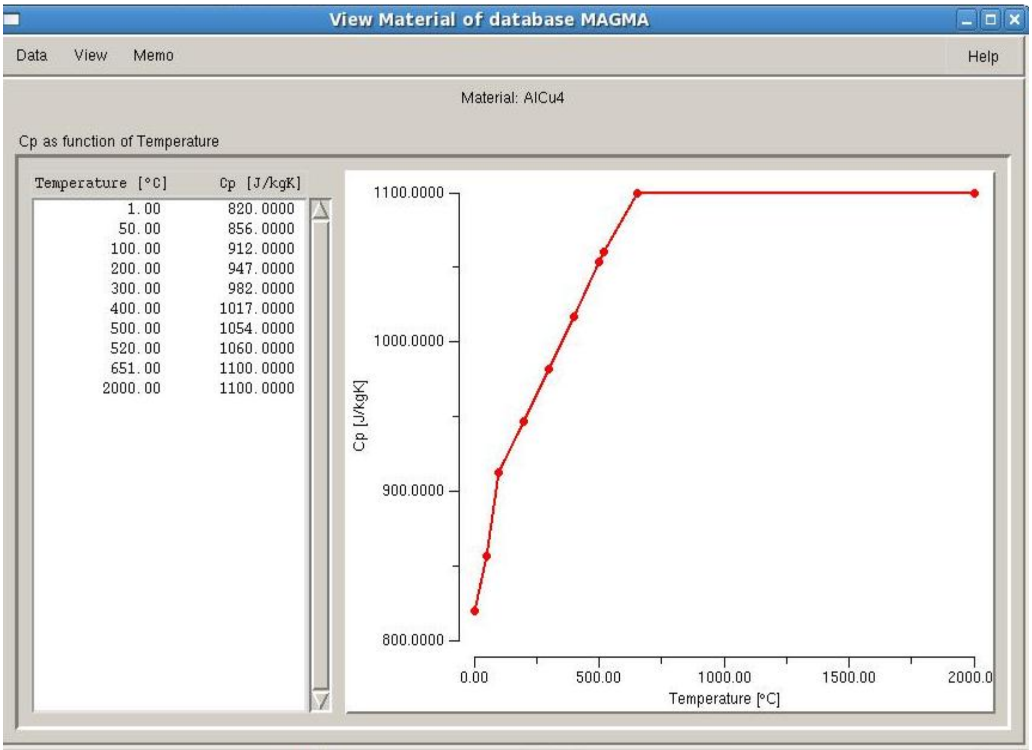

Material: AlCu4

Cp as function of Temperature

Temperature [°C]	Cp [J/kgK]
1.00	820.0000
50.00	856.0000
100.00	912.0000
200.00	947.0000
300.00	982.0000
400.00	1017.0000
500.00	1054.0000
520.00	1060.0000
651.00	1100.0000
2000.00	1100.0000

Specific Heat Capacity plotted as a function of temperature

Density: Rho

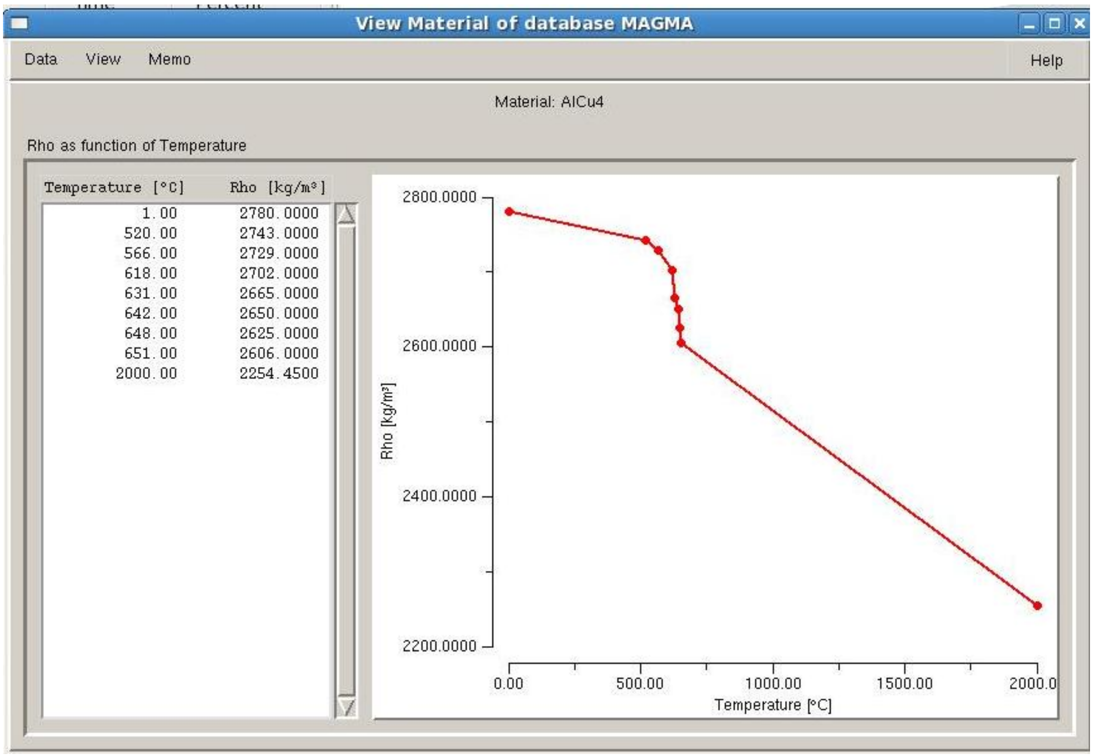

Material: AlCu4

Rho as function of Temperature

Temperature [°C]	Rho [kg/m³]
1.00	2780.0000
520.00	2743.0000
566.00	2729.0000
618.00	2702.0000
631.00	2665.0000
642.00	2650.0000
648.00	2625.0000
651.00	2606.0000
2000.00	2254.4500

Density: Rho plotted as a function of temperature from the MAGMASOFT database for the AlCu$_4$ alloy.

Density*Specific Heat Capacity

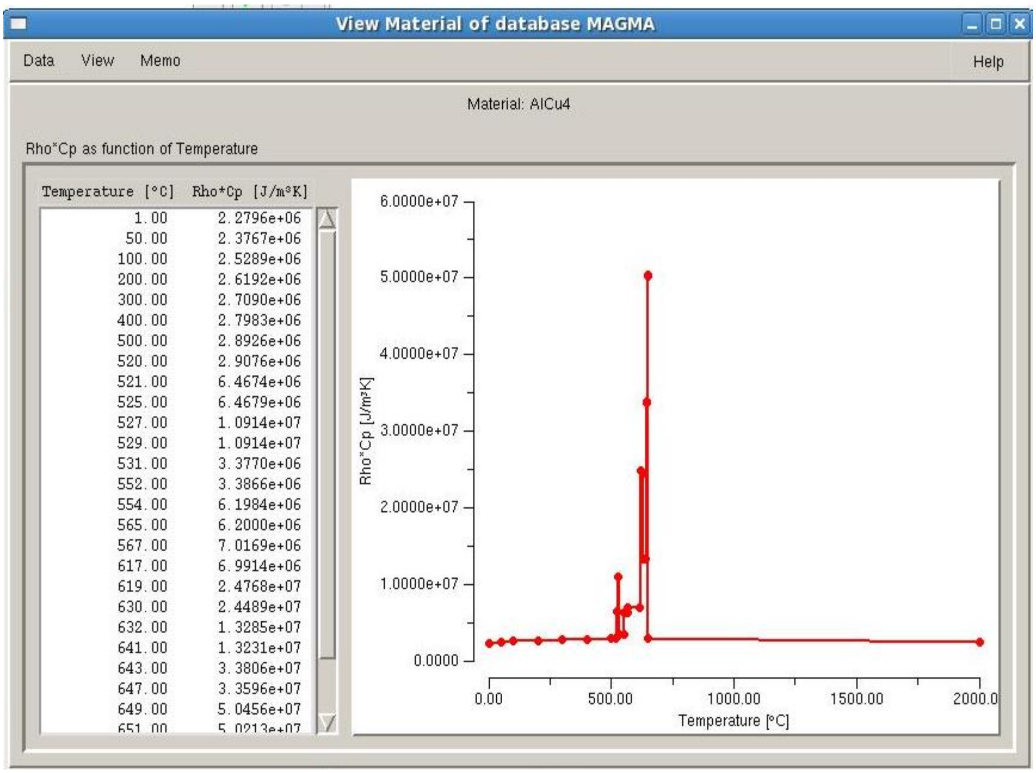

Material: AlCu4

Rho*Cp as function of Temperature

Temperature [°C]	Rho*Cp [J/m³K]
1.00	2.2796e+06
50.00	2.3767e+06
100.00	2.5289e+06
200.00	2.6192e+06
300.00	2.7090e+06
400.00	2.7983e+06
500.00	2.8926e+06
520.00	2.9076e+06
521.00	6.4674e+06
525.00	6.4679e+06
527.00	1.0914e+07
529.00	1.0914e+07
531.00	3.3770e+06
552.00	3.3866e+06
554.00	6.1984e+06
565.00	6.2000e+06
567.00	7.0169e+06
617.00	6.9914e+06
619.00	2.4768e+07
630.00	2.4489e+07
632.00	1.3285e+07
641.00	1.3231e+07
643.00	3.3806e+07
647.00	3.3596e+07
649.00	5.0456e+07
651.00	5.0213e+07

Rho*Cp is plotted as a function of temperature